Important Notice

UNIVERSITY OF CALGARY

Surface Wave Analysis and its Application to the Calculation of Converted Wave Static Corrections

by

Roohollah Askari

A THESIS

SUBMITTED TO THE FACULTY OF GRADUATE STUDIES

IN PARTIAL FULFILMENT OF THE REQUIREMENTS FOR THE

DEGREE OF DOCTOR OF PHILOSOPHY

DEPARTMENT OF GEOSCIENCE

CALGARY, ALBERTA

SEPTEMBER, 2013

Abstract

Using surface waves, we can estimate an S-wave velocity model to address the S-wave receiver statics of converted waves. Shear wave velocity is estimated from the inversion of either phase or group velocity.

I address three major problems within the realm of S-wave receiver statics and these are the problem of inversion accuracy, misinterpretation of multi-modes, and the optimization of spatial analysis windows.

To improve inversion accuracy, I develop a method to simultaneously estimate the phase and group velocities of surface waves based on the generalized S transform. The method is robust and it returns accurate results. To cope with noise and dispersion in the data, I introduce two cost functions. Though my method is robust where the surface wave is highly dispersed, I find that parameterization becomes ambiguous when the surface wave is multi-modal, and so it is possible for misinterpretation of different modes of the surface wave.

To address multi-modality for the estimation of the group velocity, I develop a slant stack method that is based again on the generalized S transform. To control spectral localization, I use a scaling factor in the generalized S transform. I find that a small scaling factor should be chosen for low frequency surface-waves, whereas for higher frequencies a larger scaling factor should be chosen.

Finally, I determine an accurate S-wave velocity model of the near surface for use in S-wave statics estimation by optimizing the analysis spatial-window. To do this, I enlarge upon the idea of CMP Cross-Correlation of Surface Waves (CCSW). I obtain a precise estimation of a dispersion curve by limiting analysis to seismic traces that lie within a limited spatial window. I find that the optimum window length (aperture) should be close (one to one and half) to the maximum wavelength in a CMP gather. I find that, through experiment, when the aperture is optimum, a high resolution image of each mode within the dispersion curve is observable, and this avoids interpretation of modal interferences. A secondary benefit of my CCSW approach is its faster computational process than the conventional implementation.

Acknowledgements

I am indebted to a lot of people whose sincere support invigorated me along my studies. First of all, I thank my advisor Dr. Robert J. Ferguson for his support and guidance in my PhD program. He provided me with peace of mind and freedom to conduct this research project. I acknowledge my PhD committee, especially Dr. Mauricio Sacchi, whose constructive and valuable comments improved this work significantly.

I would like to express my deepest gratitude to CREWES and its industrial sponsors for providing me with financial supports. I sincerely thank the director of CREWES, Dr. Gary Margrave, whose endless endeavors and attitude toward research have been a stroke of inspiration for me. I thank Dr. Helen Isaac for her collaboration and her assistance in processing the field data. I especially thank Laura Baird for her hard work and positive attitude toward international students. She tried her best in order to provide an atmosphere in which we felt comfortable as if we were home. I thank Kevin Hall for his technical support. I am grateful to Dr. Rolf Maier for his technical support and editing any English text that I had during my program.

I am thankful to Dr. Robert Herrmann from the Saint Louis University for generously providing Computer Programs in Seismology. I used his brilliant software package to compute the theoretical phase velocity and the group velocity for a given geological model.

I acknowledge my fellow students at CREWES and of the University of Calgary for fruitful discussions and support in particular Dr. Faranak Mahmoudian, Dr. Saeed Taheri, Dr. Naser Yousefzadeh, Kamran Bigdeli, Jared Fath, Hadi Samimi, Amir Shamsa, and Ritesh Sharma. I express my sincere thanks to my dear friend Dr. Hossein Hejazi for proving me with wisdom and support in some arduous situations that I had in school. I express my especial gratitude to my knowledgeable and supportive friends, Dr. Mostafa Naghizadeh and Dr. Mehdi Zeidouni. Dr. Zeidouni gave me profound insight into the inverse problem; and I learned a lot from his PhD thesis.

There are other nice people out of the University of Calgary whose support and affection will not be forgotten. I thank Phung Tieu Lam who was so supportive to me in the first of school in Calgary and created happy moments for me. Her invitation for the New Year's Eve of 2010 was a unique experience to know more about Canadian culture. I thank Bruce Littlejohn who helps international students with their accommodations. I also thank two Canadian ladies, Helen

Rempel and Steph Elizabeth, whose acquaintances were rewarding to me. They elated my sprit by their generosity and positive manners.

There are other friends that I would like to mention their names. I sincerely thank my friends Gol-Mohammad Ahmadi and Vahid Ghasemi from the Hormozgan University whose friendship was a heavenly gift for me. They were a source of inspiration to me during my B.Sc. and they whetted my motivation and courage to pursue my education. I acknowledge my friends at the University of Tehran who left me with good memories, among them Dr. Assadollah Joata Bayrami, Dr. Loghman Namaki, Dr. Mohammad Reza Hadizadeh, Dr. Navid Amini, Dr. Ali Asghar Mirzaei, and Dr. Farhad Zolfagharpour.

I am indebted to my parents' unconditional love and support without which this work was impossible. I am profoundly thankful to my dearest mother Sarvgol Hosseini who was so glum when I left her, but she endured it to see my success and happiness. I am grateful to my father Mohammad Reza Askari who has been a role model for me as he has been an upright man and taught me how to live righteously. I thank my brother and sisters for being a source of love and affection. Last but not least, I greatly thank my lovely wife Dr. Maryam Bohsagh for her love, affection and support. She was under severe stress when we were away from each other, but she perfectly endured it to protect the house of our love.

Dedication

To my parents, my wife, and

the memory of my uncle Abbas Ali-Bachari.

Table of Contents

List of Tables

List of Figures

List of Symbols

Vp	P-wave velocity
Vs	S-wave velocity
λ	Lamé module
μ	Lamé module
ρ	Density
k	Wavenumber
f	Frequency
h	Thickness
	Phase spectrum
A	S transform amplitude spectrum
Δ	Difference
Δx	Distance
S	The S transform
	Time
t	Time
S	The generalized S transform
w	Scalable window
p	Multi-factor parameter
σ	Scaling factor
α	Frequency
$\lambda\ f)$	Attenuation
d	Distance
$v_p(f)$	Phase velocity
$v_g(f)$	Group velocity
E	Cost function
ε	Wavenumber perturbation
D	Distance
s	Slowness
T	Intercept time
z	Depth

γ	Poisson ratio
Γ	Aperture length
Λ	Maximum wavelength
ζ	Variable
σ	Normal stress
	Tangential stress
u	x component
w	z component
ω	Angular frequency
	Scalar potential
	Vector potential

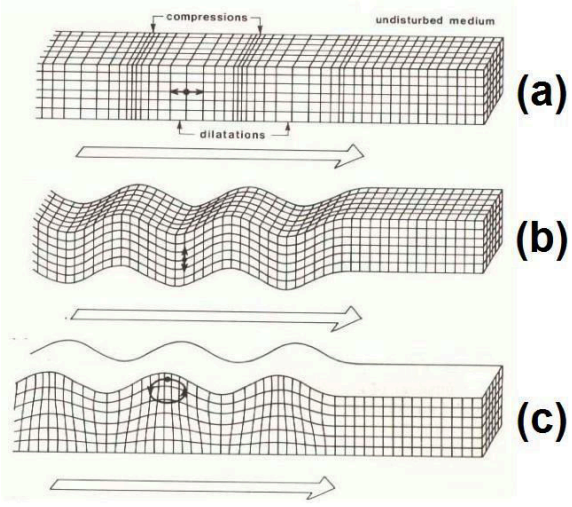

Figure 1.1 Particle motion with respect to wave propagation path for (a) P wave, (b) S wave and (c) Rayleigh wave. The large white arrow exhibits the direction of wave propagation, and the small black arrow indicates particle motion (After Dulaijan, 2008).

1.1.2 Surface waves

Surface waves propagate travel along the earth's surface (Lay and Wallace, 1995). They travel slower than body waves. There are two important categories of surface waves, 'Love waves' and 'Rayleigh waves' (Sheriff and Geldart, 1986). Love waves are horizontally polarized shear waves (SH waves) which are trapped in an elastic layer which is bordered by an elastic half space on one side and a vacuum on the other side. Rayleigh waves (also known as ground roll) are composed of both longitudinal and transverse (Figure 1.1c) motions whose amplitudes decrease exponentially with respect to depth. There is a phase difference between these component motions. Considering a vertical plane which is oriented in the direction of wave propagation, Rayleigh wave motion is elliptical. At the top of the ellipse, particle motion is opposite to the direction of propagation, whereas at the bottom, it is in the direction of propagation (Figure 1.2).

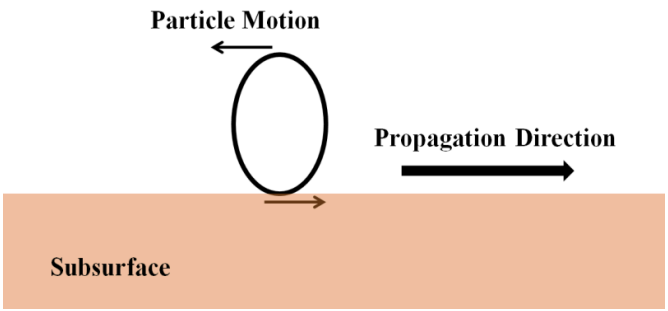

Figure 1.2 Rayleigh wave particle motion

1.2 Seismic reflection survey

Seismic waves are used to study the earth's interior. Earth layers are composed of different materials in which P and S-waves travel and propagate with different velocities. Figure 1.3 shows an example of seismic data acquisition. A seismic source releases energy into the ground. A medium in which seismic data is acquired is either marine or land (Evans, 1998). P and S-Waves velocities vary from one layer to another due to changing composition and compression. In a boundary between two layers where there are density and velocity contrasts, a fraction of the incident wave is transmitted, and a fraction is reflected back to the surface (Sheriff and Geldart, 1986). Reflected waves are used as signals in reflection seismology to image, characterize and study the subsurface. After acquisition, seismic data are processed to remove noise such as ground roll, air waves, multiples, direct waves, and random noises and improve signals (reflectors). There are many processing flows for noise removal and signal enhancement. For instance, band pass and FK filters which are based on the 2D Fourier transform for ground roll attenuation (Yilmaz, 2001), stacking schemes are utilized for random noise attenuation (Yilmaz, 2001), and migration algorithms are implemented to move dipping reflections to their true locations with correct amplitudes and dip (Yousefzadeh, 2012). One of the most important processing steps is the calculation of static corrections to compensate near surface effects. Figure 1.4b shows an image produced by reflected waves of a subsurface. In seismic exploration, sources and receivers are usually located on the surface or few meters below the surface.

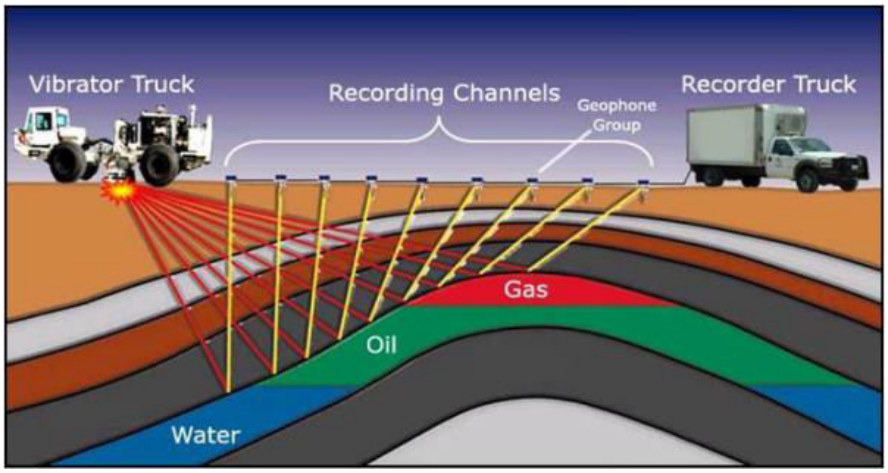

Figure 1.3 A seismic survey (http://cougarlandservices.net/landowners). Vibroseis is used as a source.

1.3 Near surface weathered layer and seismic data quality

Seismic data quality is affected by the near surface. The near surface is characterized by the weathered layer. The weathered layer is defined by an unconsolidated layer, gravel or clay, in which seismic waves travel more slowly than for consolidated rocks (Sheriff, 1991). We can consider the water table as a base for the weathered layer because of the sharp increase of seismic velocity in the presence of water. The base of the weathered layer can be sharp or gradual. Since, in the presence of water, seismic waves' velocities increase, water tables may be considered as a base for the weathered layer boundary.

The velocity of the near surface changes dramatically in the presence of the weathered layer where soil properties change rapidly with respect to geophone location (Yi-Ke et al. 2001). When different ray paths travel to the surface from a reflector, they arrive at different times due to different delays caused by velocity variations of the near surface. After applying migration, we might see time shifts on a reflector that can be misleading in the interpretation of seismic data. Figure 1.4a shows a final image of seismic data obtained from converted waves. The data set was acquired by Consortium for Research in Elastic Wave Exploration Seismology, University of Calgary (CREWES), near Hussar, Alberta, Canada (Margave et al. 2011). Geological structures of the site of study are horizontally flat layers. As seen in Figure 1.4a, the reflectors do not seem to be flat because huge velocity variations of the weathered layers cause ray paths to arrive at the surface at different times. The effect of these huge velocity variations can be observed on the stacked data in Figure 1.4a as some seismic traces are shifted about 100 ms with respect to each other. In order to obtain a more accurate image of the subsurface, near surface effects must be compensated. In the seismic literature, compensations of the near surface weathered layers are called static corrections (Yilmaz, 1987). Figure 1.4b shows the final image of the Hussar data after applying static corrections. We see a flat trend of reflectors after applying static corrections.

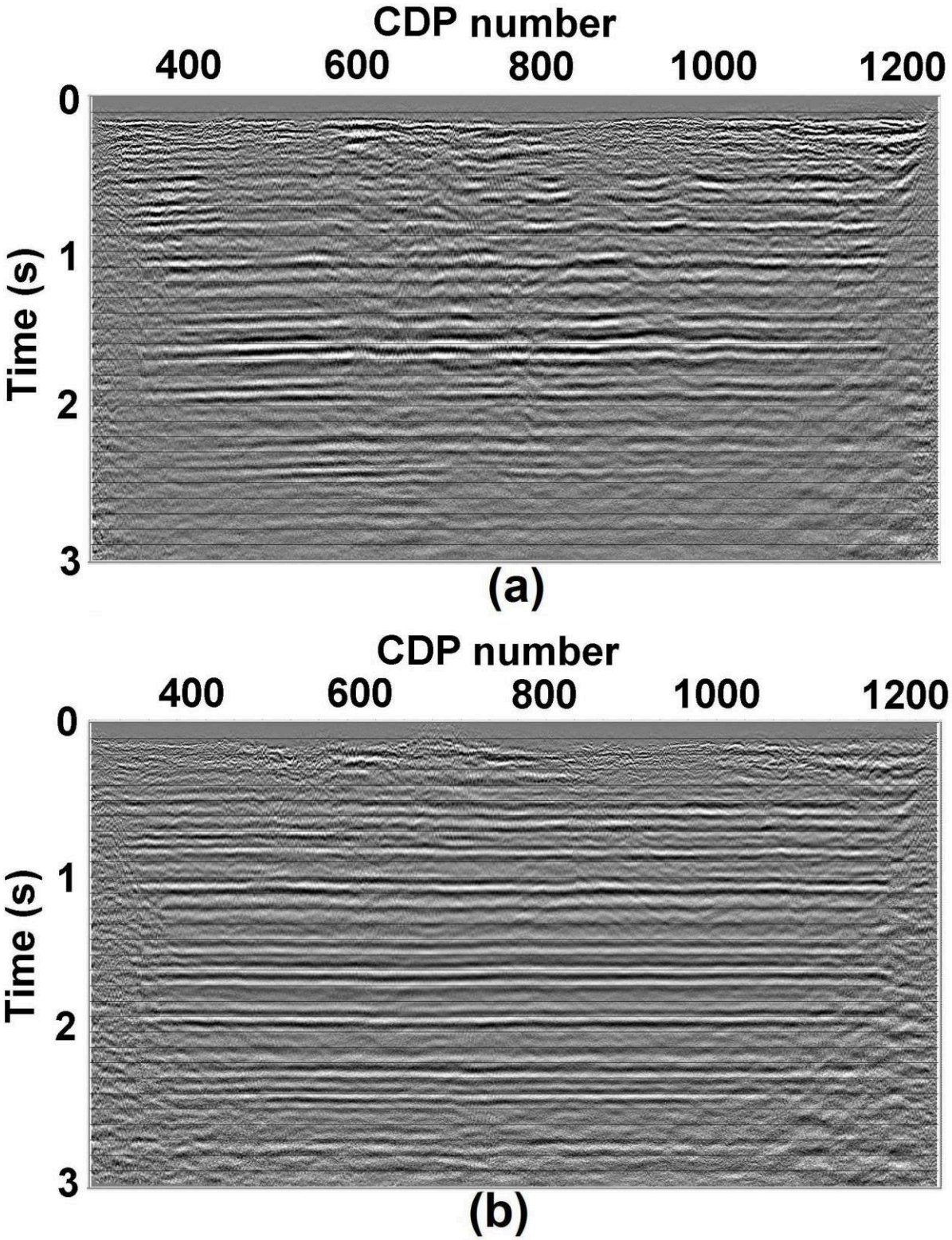

Figure 1.4 A seismic image (a) before static corrections, and (b) after applying static corrections.

1.4 Converted waves and static corrections

As mentioned earlier, at a boundary of two layers where there are density and velocity discontinuities, a fraction of the incident wave is transmitted and a fraction is reflected back to the surface. Some of the energy of the transmitted and reflected waves is converted to other types of waves (Stewart et al., 1999). When an incident P-wave is converted to an S-wave, this mode is called a converted wave in the literature. In converted wave data acquisition, P- and S-waves are recorded by three component receivers (Stewart et al., 1999). Every receiver has one vertical component (V) and two horizontal components (H_{radial} $H_{tangential}$). The vertical component records mainly P-waves and a fraction of the S-waves' projections, whereas the horizontal components record the S-waves and a fraction of the P-waves' projections. S-wave velocity information obtained from converted waves is crucial to determine some physical properties of a reservoir. Although converted wave data acquisition has been considered as one of the promising methods for oil exploration, there are still many challenges that must be addressed. One of these is the S-wave receiver statics, which can be two to ten times greater than the P wave receiver statics (the amount of static corrections which is calculated for the P-waves) (Tatham and McCormack, 1991) due to the large V_p/V_s ratio in the near surface.

There are two categories of methods to address S-wave receiver static corrections, *modeling methods* and *data-based methods*. In modeling methods, we estimate an S-wave velocity model for the near surface from which S-wave receiver static corrections are calculated. Data used for modeling can be obtained from either refracted wave analysis (Frasier and Winterstein, 1990) or surface waves analysis (Park et al., 1999a). Refracted wave methods are based on the analysis of first arrival seismic waves. We model the subsurface based on the concept of refracted waves and divide the subsurface into layers based on the number of apparent slopes that we see at the first arrivals of seismic waves (Palmer, 1980). Although refracted wave analysis is widely used for the estimation of P-wave statics, the methods become ambiguous when we deal with S-waves because it is very hard to pick first arrivals of S-waves. First arrivals of S-waves are sometimes contaminated by noise or are masked by (the first) arrivals of P-waves.

An alternative to estimate S-wave receiver statics from refracted wave analysis is to calculate P-wave receiver statics and then scale the calculated P-wave receiver statics by the

V_p/V_s ratio. This approach suffers from the fact that there is not a constant V_p/V_s ratio for the near surface which results in an inaccurate estimate of S-wave receiver statics. Surface wave analysis is based on the dispersion analysis of Rayleigh waves (ground roll). Ground roll is a predominant event in seismic data and is historically considered as noise in the reflection seismic literature. Dispersion means different frequency components of a signal travel with different velocities, and the velocity of each frequency component is called the phase velocity. Generally in surface wave analysis, a phase velocity for the fundamental mode is estimated and inverted to an S-wave velocity model where the depth of investigation is confined by frequency bandwidth (Xia et al., 1999).

Data-based methods are not based on modeling of the subsurface. The CRP stack-power optimization method (Cary and Eaton, 1993) is based on improving the resolution of stacked data by estimating S-wave receiver statics from the stacked data without static corrections. The method is not straight forward when geological structures are complex or converted waves are weak (Li et al., 2012). Monte-Carlo simulated annealing (Eaton et al. 1991) is again based on the resolution of stacked data, but S-wave receiver statics are calculated from Monte-Carlo simulated annealing. The method is computationally expensive (Li et al., 2012).

1.5 Near surface S-wave velocity and ground roll dispersion analysis

Where a medium is an isotropic, homogeneous and half space, Rayleigh waves (ground roll) are not dispersive. In other words, different frequency components of Rayleigh waves travel at the same velocity. But in a real layered earth, different frequency components of Rayleigh waves are affected by the velocity structure of the subsurface layers. If we assume the seismic wave velocity to increase with depth, high frequency components (short wavelengths) are affected by the velocity structure of shallower layers where P-wave and S-wave velocities are low. On the other hand, low frequency components (long wavelengths) are affected by the velocity structure of deeper layers. Therefore in this case, low frequency components have higher velocities in comparison with high frequency components. The variation of Rayleigh wave velocity at different frequencies is dispersion. The effects of dispersion become more obvious with increasing distance, because the low frequency components of Rayleigh waves arrive sooner at any recording station. We can see this phenomenon on a seismic record as Rayleigh waves (ground roll) are more drawn out in time with increasing distance (Figure 1.5). Rayleigh wave velocity is described by two concepts, ‘phase’ and ‘group’ velocities. Phase

velocity is the velocity of each frequency component (single harmonic) of dispersed waves, whereas the group velocity is the velocity of a wave pocket of dispersed waves. Many authors have studied surface wave dispersion (i.e. Rayleigh, 1887; Sezwa, 1927; Thompson, 1950; Dobrin, 1951; and McMechan and Yedlin, 1981).

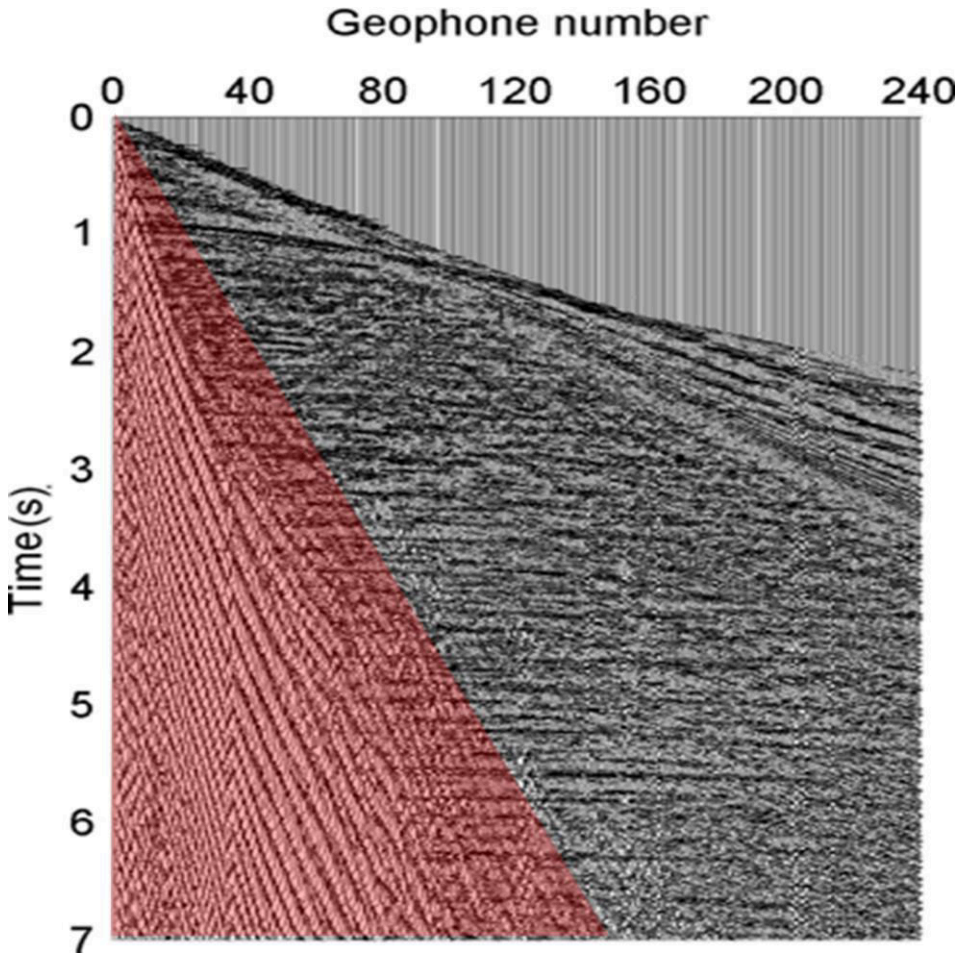

Figure 1.5 A seismic shot record. Rayleigh waves (ground rolls) are more drawn out in time with increasing distance (the red triangle) (from Askari and Siahkoohi, 2008).

It is possible to estimate an S-wave velocity model from the phase velocity of dispersed Rayleigh waves (ground rolls) though an inverse procedure. We can forward model the phase velocity for any geological 1D model using Knopoff's method (Schwab and Knopoff, 1972, Abo-Zena, 1979). The Rayleigh-wave phase velocity, $v_p(f)$, is determined by a nonlinear equation 'F' in an implicit form (Appendix A):

$$F\left(f, v_p(f), V_s, V_p, \rho, h\right) = 0, \tag{1.3}$$

where f is the frequency, V_s and V_p denote the S- and P-wave velocities respectively, h is the thickness of each layer, and ρ is the density of each layer. Based on equation 1.3, it is possible to estimate an S-wave velocity model from the phase velocity through inversion. If we divide the subsurface into thin layers with constant thicknesses but with varying shear wave velocities, we can formulate equation 1.3 as a function of P-wave velocity, S-wave velocity and density. This approach is similar to the familiar approach used in tomography, where the subsurface is divided into small grids. In order to examine the sensitivity of the phase velocity to the shear wave velocity, P-wave velocity and density, we calculate the dispersion function's derivatives for a synthetic geological model (Table 1.1) using the finite difference method. We increase the S-wave velocity, P-wave velocity and the density of the fifth layer by about 20% to calculate the derivatives. Figure 1.6 shows the calculated derivatives for the S-wave velocity, P-wave velocity, and density respectively. The phase velocity is most sensitive to the variation of the S-wave velocity. Therefore, we can assign reasonable constant values of P-wave velocity and density (Xia et al., 1999) for our inverse procedure (Figure 1.7) to obtain a shear wave velocity model from the phase velocity. In the inversion, the phase velocity is the data space and the S-wave velocity is the model space. We optimize the model space (the S-wave velocity) by minimizing an objective function which is the difference between the observed phase velocity and the calculated phase velocity (Appendix B). An initial S-wave velocity model is estimated by the method proposed by Xia et al. (1999). We calculate the theoretical phase velocity model and compare it to the observed phase velocity obtained from field data. If the norm of the difference of the observed and calculated phase velocities is small enough, we terminate the process; otherwise, we update the S-velocity model using an inverse method (Conjugate Gradient for example (Appendix B)). After some iterations, we will obtainthe final S-wave velocity model.

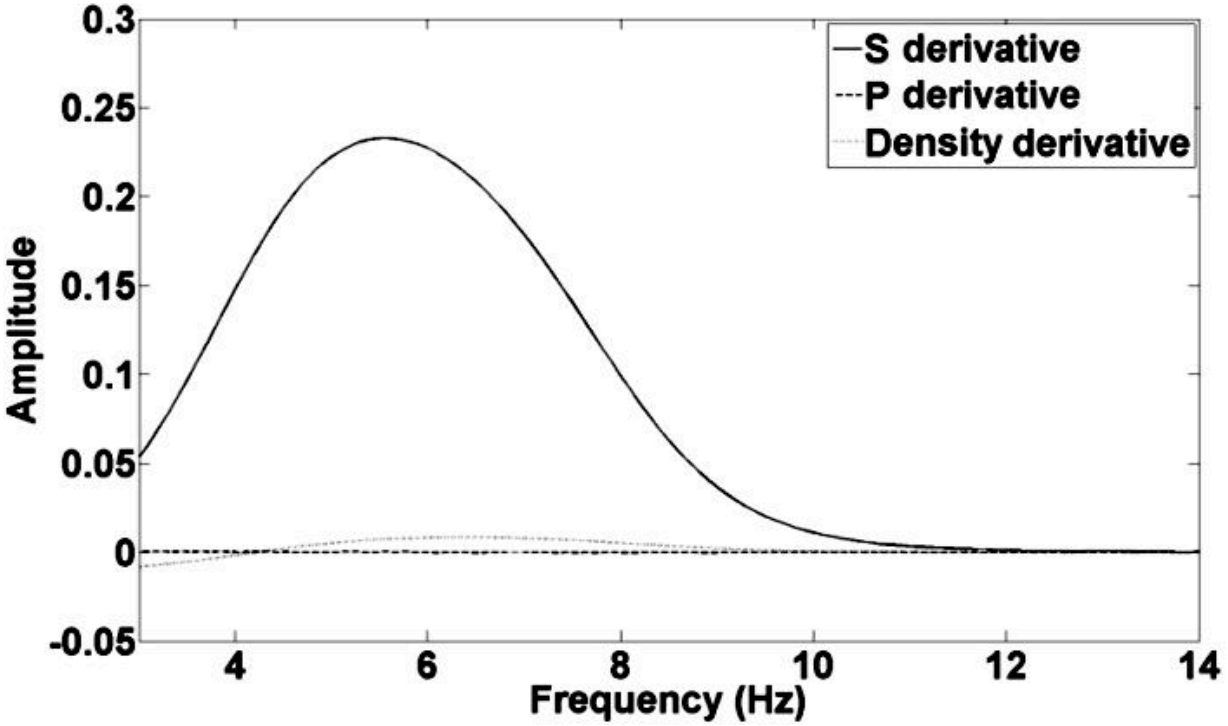

Figure 1.6 Phase velocity derivative with respect to S-wave, P-wave velocities and density respectively for the fifth layer.

S-wave Velocity (m/s)	P-wave velocity (m/s)	Density (kg/m3)
241	1654	2000
197	1681	2000
333	1721	2000
343	1742	2000
321	1760	2000
329	1772	2000
370	1790	2000
415	1793	2000
444	1777	2000
459	1766	2000

Table 1.1 The geological model used for the calculation of the derivatives in Figure 1.6. The thickness of each layer is 5 m.

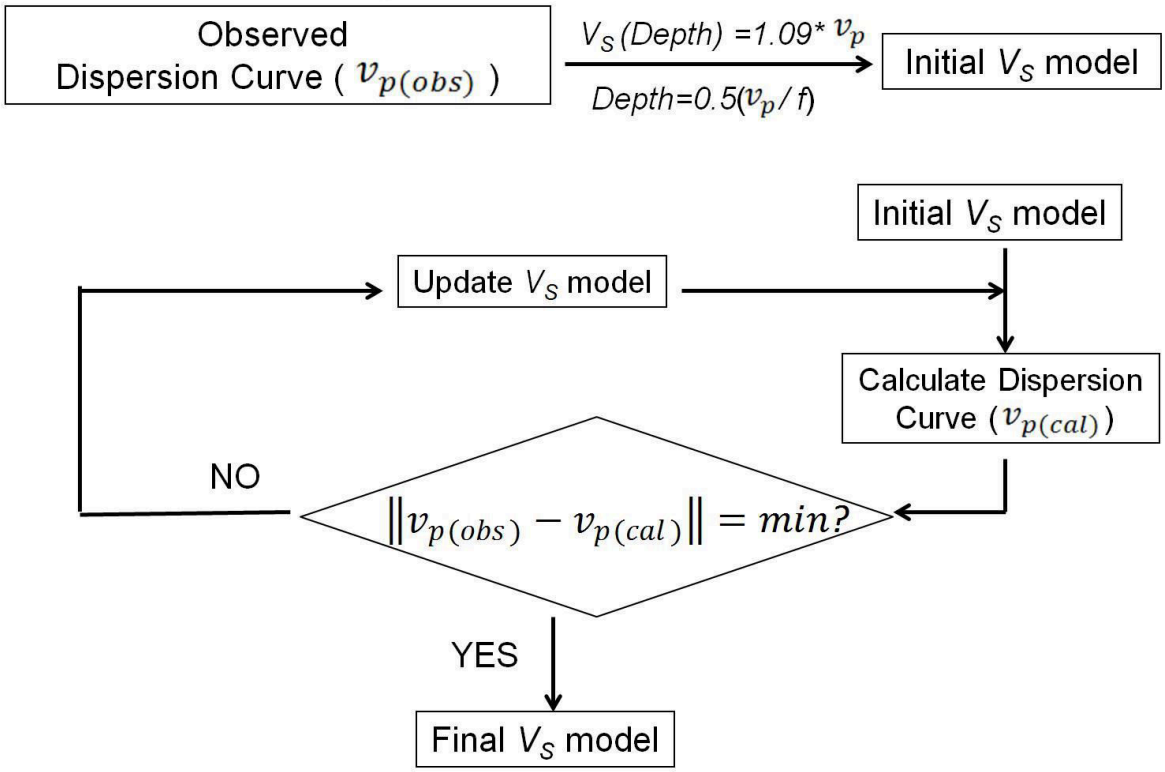

Figure 1.7 The inverse procedure used for the estimation of shear wave velocity from the phase velocity.

1.6 Surface wave analysis methods

Spectral Analysis of Surface Waves (SASW) (Nazarian et al., 1983) is a conventional method for the determination of 1D shear wave velocity for the near surface. The ground roll fundamental mode is analyzed by configuring and reconfiguring a pair of receivers and shots respectively (Figure 1.8). For each shot, there are two records. If we calculate the Fourier spectrum of the two records, we can estimate the phase velocity from the Fourier phase difference between the two records with respect to the distance between the two geophones and frequency (Chapter 2 presents how we can estimate the phase velocity from the phase spectrum). Since there are two shots, two values for the phase velocity are estimated. An average of the estimated phase velocity values is calculated and is assigned to the midpoint.

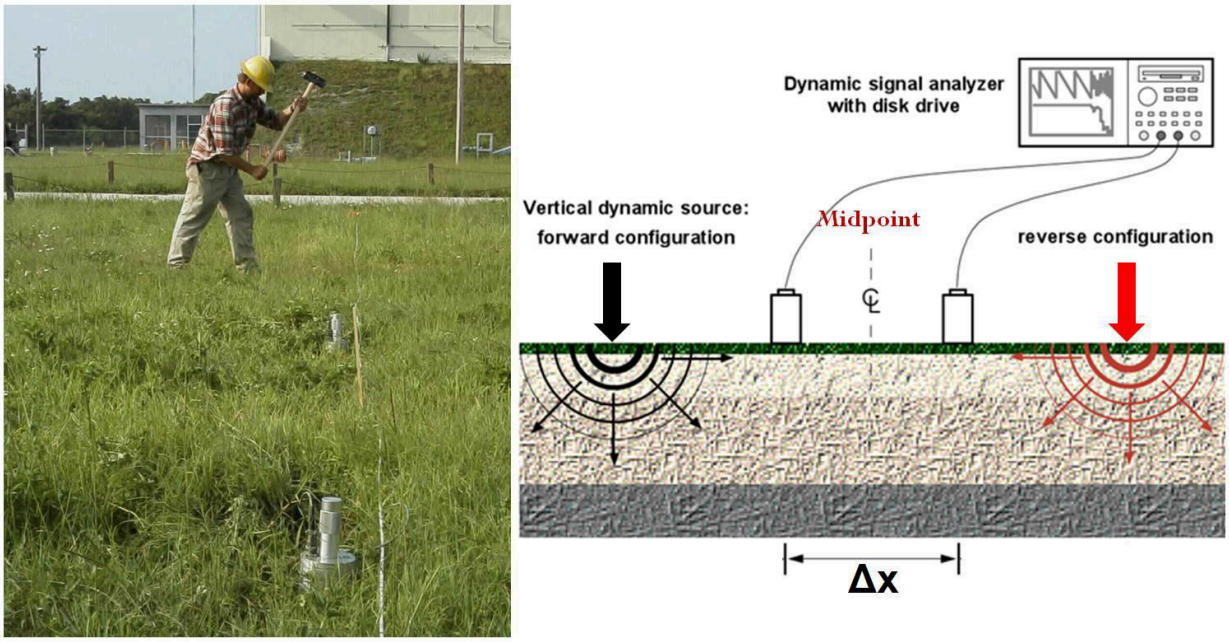

Figure 1.8 A SASW survey (http://www.geovision.com/PDF/M_SASW.PDF). There are two shots (the black and red arrows). The phase velocity is measured with respect to the midpoint.

Park et al. (1999a) introduce the Multi-channel Analysis of Surface Waves (MASW) method, where a dispersion curve for a multi-channel data set is estimated by transforming (e.g. the phase shift method (Appendix C, Park et al., 1998) the data from the time-offset domain to the frequency-slowness (or velocity) domain (Figure 1.9). Generally speaking, in a MASW survey the calculation of dispersion curves is faster and more accurate than that for SASW because we can isolate and distinguish other unwanted coherent events such as first arrivals, higher modes and air waves. Furthermore, MASW is less affected by ambient noise and provides a better signal to noise ratio (Hayashi and Suzuki, 2004). Therefore, MASW results in better dispersion curve estimation, but at the cost of lateral resolution because of the long receiver array that must be used (Park et al., 1999b). Paradoxically, smaller arrays should be used when we need a better lateral resolution, but this reduces the resolution of the dispersion curve. Therefore, there is a tradeoff between the estimation of the dispersion curve and lateral resolution. In practice, it is critical to compensate for this tradeoff. Especially in converted wave surveys, rapid spatial velocity variations in the weathering layer need to be resolved in order to compute an appropriate velocity model for the static corrections. This requires both excellent quality phase velocity information and high spatial resolution.

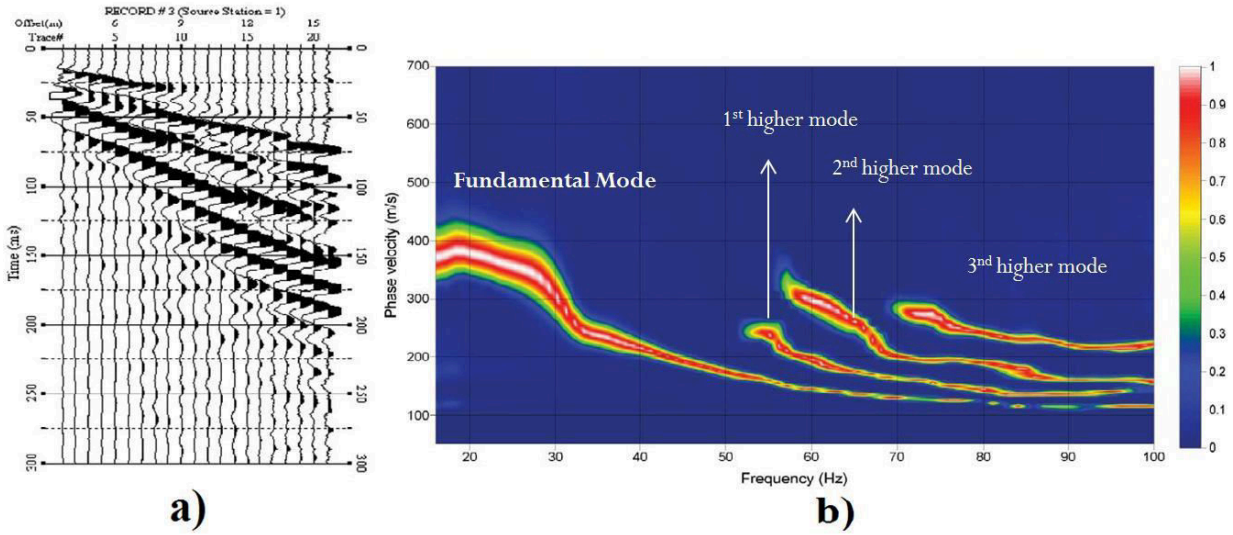

Figure 1.9 (a) A shot record containing dispersed (Rayleigh wave) ground roll, and (b) the estimated phase velocity (form Luo et al., 2008).

Hayashi and Suzuki (2004) introduce CMP Cross-Correlation of Surface Waves (CCSW) to increase lateral resolution. In Hayashi and Suzuki's methodology, all traces within a common mid-point (CMP) are correlated with each other, traces with the same offset which belong to the same CMP are stacked, and a dispersion curve is computed. This method provides good lateral resolution because the phase velocity is estimated with respect to midpoints, similar to SASW where the phase velocity is estimated with respect to midpoints. This approach provides improved lateral resolution of the S-wave velocity. On the other hand, the dispersion curves are estimated from multi-channels, similar to MASW where the phase velocity is estimated from multi-channel data which facilitate the estimation of the phase velocity in the presence of noise. Therefore CCSW takes the advantages of the two conventional methods to improve lateral resolution and dispersion curve estimation simultaneously.

1.7 Thesis objective and organization

The main objectives of this thesis are to introduce new approaches to improve surface wave analysis, including developing mathematical models to estimate the phase and group velocities for surface wave studies, to introducing a new approach for the estimation of the group velocity of multi-modal surface waves, and to enlarge upon a new approach to CMP Cross-Correlation of Surface Waves (CCSW) to increase the lateral resolution of the S-wave velocity to

compute receiver static corrections for converted wave. This thesis is organized into three parts based on three articles that have been published or are being submitted to peer-reviewed journals.

Shear wave velocity is estimated from the inversion of phase and group velocity. Therefore, the analysis of dispersion data to link phase and group velocity to frequency is a crucial step. Some algorithms have been developed to address these issues in different transform domains such as the FK transform (Yilmaz, 1987), ω-p transform (McMechan and Yedlin, 1981), the phase shift (Appendix C, Park et al., 1998), and the wavelet transform (Kulesh et al., 2005; Holschneider et al., 2005; Kulesh et al, 2008) for phase velocity, and narrow band-pass filtering (Herrmann, 1973) and the wavelet transform (Kulesh et al., 2005; Holschneider et al., 2005) for group velocity. One of the objectives of this thesis is to develop mathematical models to estimate the phase and group velocities for surface wave studies. **Chapter 2** presents a mathematical model (Askari and Ferguson, 2012) based on the generalized S transform (Pinnegar and Mansinha, 2003a) to estimate wave propagation parameters (phase velocity, group velocity and the attenuation function) for a highly dispersive medium and noisy data. A scaling factor is used in the generalized S transform to enable the application of the method in highly dispersive meda. In order to improve the method, two cost functions in the generalized S transform domain are introduced. The first cost function estimates an optimum value for the scaling factor. The second cost function generalizes the application of the method to noisy data, especially data with a low signal to noise ratio at low frequencies where the wave number is perturbed. As a remedy, wave number perturbation is estimated by minimizing the cost function using Simulated Annealing. Synthetic and real data examples are presented to show the efficiency of the method for the estimation of propagation parameters of highly dispersive media and noisy data.

Chapter 3 presents a new approach for the estimation of the group velocity of multi-modal surface waves. Though the method introduced in Chapter 2 is robust especially where the surface wave is highly dispersed, parameterization within the method becomes ambiguous when the surface wave is multi-modal. Multi-modal means for any frequency, surface wave does not travel with a unique velocity; surface wave travel with different, distinct and discrete velocities that satisfies equation 1.3. This can make the analysis of surface waves difficult (Herrmann 1973). Based on the generalized S transform domain, slant stacking is implemented to identify

the linear events that correspond to multi-modal surface waves. To ensure optimal resolution, a scaling factor into the generalized S transform is introduced to control spectral localization. We find that a smaller scaling factor should be chosen for low frequency surface waves, whereas, for higher frequencies, a larger scaling factor should be chosen. We show the application of the method to the estimation of the group velocity for synthetic and real data, and we also estimate a near surface shear wave velocity model for the real data based on our estimated group velocity. We find that the model is well matched to another model separately obtained from an estimated phase velocity.

Chapter 4 presents a new approach enlarged upon the idea of CMP Cross-Correlation of Surface Waves (CCSW) to compute receiver static corrections for converted waves. We need an accurate shear wave velocity model of the near surface to address receiver static corrections for converted waves. Each trace of a shot record is cross-correlated with a reference trace that is selected from within the shot gather based on a high signal to noise ratio. This step removes the source effect (the initial phase of a source). New midpoints that relate to the correlated traces are then calculated. We calculate the phase velocity for each CMP gather, and we convert the resulting dispersion curve to a vertical shear wave velocity through an inverse procedure (Conjugate Gradient (Appendix B) for example). Our approach is faster than the conventional CCSW because in the conventional CCSW all traces within a CMP gather are cross-correlated with each other which is computationally expensive. In this chapter, we show that in order to have a precise estimation of dispersion curve, we only consider those traces which lie in a special window. An optimum window length should be close (one to one and half times) to the maximum wavelength in a CMP gather. The window is the so-called aperture. If the aperture is too short, we see a low resolution image of dispersion curves which cause modal interference. When the aperture is optimum, we see a high resolution image of dispersion curves that avoid modal interferences. Therefore, not only does an appropriate aperture length improve dispersion curve estimation, but it also avoids the modal interference that is so disastrous in surface waves studies. 2D near surface shear wave velocity models are estimated for two real data sets. By decimating traces from the first dataset, we show that we can obtain a good trend of S-wave statics similar to those obtained from the original dense array data. This demonstrates that CCSW has a capacity to address static correction of converted waves when geophone spacing is wide. Using the second data set, the importance of wavelength dependent aperture is presented.

We obtain static corrections based on an S-wave velocity model obtained from CCWS and successfully apply them to the data.

Chapter 5 summarizes and concludes the thesis.

1.8 Software used in this thesis

All the codes I used in Chapters 2 and 3 to calculate the phase and group velocity were written in MATLAB. I also wrote a code for the calculation of the phase velocity using the phase shift method and Conjugate Gradient method in Matlab. I used Computer Programs in Seismology developed by Dr. Robert Herrmann from the Saint Louis University to compute the theoretical phase velocity for a given geological model. The software is free and open-source, and can be found at http://www.eas.slu.edu/eqc/eqccps.html. The initial steps in the processing of the Priddis and Hussar data such as applying different filters to the data in order to preserve ground roll, which is considered as signal in this thesis, were accomplished in PROMAX in collaboration with Dr. Helen Isaac. I collaborated with Dr. Isaac in her use of PROMAX to apply the calculated S-wave static corrections to the stacked data, and to perform velocity analysis.

Chapter Two: Dispersion and the Dissipative Characteristics of Surface Waves in the Generalized S Transform Domain

2.1 Overview

Wavenumber, group velocity, phase velocity, and frequency-dependent attenuation characterize the propagation of surface waves in dispersive, attenuating media. We use a mathematical model based on the generalized S transform to simultaneously estimate these characteristic parameters for later use in joint inversion for near-surface shear wave velocity. We use a scaling factor in the generalized S transform to enable the application of the method in a highly dispersive medium. We introduce a cost function in the S-domain to estimate an optimum value for the scaling factor. We also use the cost function to generalize the application of the method for noisy data, especially data with a low signal-to-noise ratio at low frequencies. In that case, the estimated wavenumber is perturbed. As a solution, we estimate wavenumber perturbation by minimizing the cost function, using Simulated Annealing. We use synthetic and real data to show the efficiency of the method for the estimation of the propagation parameters of highly dispersive and noisy media.

2.2 Introduction

The accurate estimation of shear wave (S-wave) velocity for near surface material such as soil, rocks, and pavement is important for many engineering and environmental purposes, as shear wave velocity is one of the essential properties used in stiffness coefficient determination (Xia et al., 2002a). Though seismic refraction methods are widely used for shear wave velocity studies (Palmer, 1980), they fail to estimate S-velocity where geological structure is complex (Xia et al., 2002c) or where a hidden layer (a layer whose velocity is less than its upper layer) is present (Sheriff and Geldart, 1986).

An alternative to refraction analysis is surface wave analysis. Surface wave analysis is a well-known procedure in which the phase or group velocity of dispersive surface waves is inverted to estimate the shear wave velocity structure (e.g. Evison et al., 1959; Stokoe et al., 1988; Keilis-Borok, 1989; Lay and Wallace, 1995; Xia et al., 1999). The usefulness of surface waves lies in their interaction with elastic discontinuities in the subsurface. Velocity varies with wavelength, where discontinuities are in the order of wave lengths (Park et al., 1999a). This

variation, known as dispersion, is observable on seismic records as a change in the period of successive wave cycles with time (Kennett, 1983).

Shear wave velocity is estimated from the inversion of the frequency-dependent phase and group velocity. Therefore, analyzing dispersion data to link phase and group velocity to frequency is a crucial step. Some algorithms have been developed to address these issues in different transform domains, such as the Fourier phase spectrum analysis (Sato, 1955), the FK transform (Yilmaz, 1987), the ω−p transform (McMechan and Yedlin, 1981) the phase shift (Appendix C, Park et al., 1998), the wavelet transform (Holschneider et al., 2005; Kulesh et al., 2005; Kulesh et all, 2008), the slant stack (Xia et al., 2007) and the linear Radon transform (Luo et al., 2009) for phase velocity and narrow band-pass filtering (Herrmann, 1973), and the wavelet transform (Holschneider et al., 2005; Kulesh et al., 2005) for group velocity.

In this study, the generalized S transform (Pinnegar and Mansinha, 2003a) is used to estimate wave propagation parameters (the wavenumber, phase velocity, group velocity, and the attenuation function) for a highly dispersive medium and noisy data. The advantage of the S transform (Stockwell et al., 1996) and its generalized versions (e.g. Mcfadden et al., 2002; Pinnegar and Mansinha, 2003a; Pinnegar and Mansinha, 2003b; Pinnegar and Mansinha, 2004) lies in the fact that it provides frequency-dependent resolution while maintaining a direct relationship with the Fourier spectrum. Using this property, wavenumber and phase velocity are obtained directly from the absolute phase value of the ridges of the S-domain, and group velocity is computed from the time difference of the ridges of the transform. Frequency-dependent attenuation is estimated by the relative amplitudes of the ridges of the transform. Kulesh et al. (2005) and Holschneider et al. (2005) propose a method for the estimation of the characteristic parameters of moderately dispersive surface waves based on the wavelet transform. Using a scaling factor introduced in the generalized version, we significantly improve estimation of the characteristic parameters of surface waves for highly dispersive data. Experimentally, we find that the estimated wavenumber is perturbed for noisy data when signal-to noise-ratio is small at low frequencies. As a remedy, we estimate wavenumber perturbation by minimizing a cost function using simulated annealing.

Based on these cost functions we can obtain the wave propagation parameters from real data, according to the generalized S transform spectrum. An optimum value for the scaling factor can be estimated from a clean or relatively clean record for a data set. For other records, if

signal-to-noise ratio (S/N) is small at low frequencies, a wavenumber perturbation must be applied on the estimated wavenumber. The wavenumber perturbation is obtained using the second cost function. We show the application of the method for a real data example.

2.3 Theory

The S transform is a time-frequency spectral localization method that is similar to the short-time Fourier transform (Gabor, 1946). The Gaussian window in the S transform is a function whose width scales inversely with frequency and whose height scales directly with frequency. The S transform is given by Stockwell et al. (1996) as

$$S[h(\tau)](t,f) = \int_{-\infty}^{+\infty} h(\tau) \left[\frac{|f|}{\sqrt{2\pi}} e^{-\frac{f^2(\tau-t)^2}{2}} \right] e^{-j2\pi f\tau} d\tau. \quad (2.1)$$

where, as an operator, S transforms h, which is a function of τ into a function of frequency f and time t. Time t controls the position of the Gaussian window on the output time axis. In equation 2.1 τ denotes time, and the expression in between brackets is the frequency-dependent scalable Gaussian window. The scaling property of the Gaussian window is reminiscent of the scaling property of continuous wavelets (Mallat, 1999) because one period of the frequency f is always equal to one standard deviation of the window (Stockwell et al., 1996). The S transform, however, is not a wavelet transform because the oscillatory parts of the S transform "wavelet" (provided by the complex Fourier sinusoid) do not translate with the Gaussian window when t changes. As a result, the shapes of the real and imaginary parts of the S transform wavelet change as the Gaussian window translates in time. True wavelets do not have this property because their entire waveform translates in time with no change in shape (Pinnegar and Mansinha, 2003b). Phase measured by the S transform is the localized value of absolute phase with respect to the Fourier spectrum (Pinnegar and Mansinha, 2003a). Thus, the S transform is conceptually a combination of short-time Fourier analysis and wavelet analysis.

A more general version of the S transform allows arbitrary variation in the window. The generalized S transform is (Pinnegar and Mansinha, 2003a)

$$S_g[h(\tau)](t,f,\boldsymbol{p}) = \int_{-\infty}^{+\infty} h(\tau) w(\tau - t, f, \boldsymbol{p}) e^{-j2\pi f\tau} d\tau, \quad (2.2)$$

where the Gaussian window of the S transform is generalized into the modeling window w whose width and shape are now a function of parameter $\boldsymbol{p}$. A version of the generalized S transform that has particular usefulness in our analysis is defined using

$$w(\tau - t, f, \sigma) = \frac{|f|}{\sqrt{2\pi}\sigma} e^{-\frac{f^2(\tau-t)^2}{2\sigma^2}}, \tag{2.3}$$

where, compared with the Gaussian window in equation 2.1, a scaling factor σ is introduced (Pinnegar and Mansinha, 2003a). Using σ, the generalized S transform is written as

$$S_g[h(\tau)](t, f, \sigma) = \int_{-\infty}^{+\infty} h(\tau) \frac{|f|}{\sqrt{2\pi}\sigma} e^{-\frac{f^2(\tau-t)^2}{2\sigma^2}} e^{-j2\pi f\tau} d\tau, \tag{2.4}$$

where the scaling factor σ controls time-frequency resolution by changing the number of oscillations within the window. Figure 2.1 shows the Gaussian window for the scaling factors σ=1, 0.25, and 4 at a frequency of 10 Hz. When σ is smaller than one, the Gaussian window is tightened in the time domain and the time resolution increases. On the other hand, for σ larger than one, the Gaussian window is expanded in the time domain and, therefore, the frequency resolution increases. Figure 2.2a shows a signal that consists of three Ricker wavelets with central frequencies of 50 Hz at 0.25 s, 150 Hz at 0.50 s, and 250 Hz at 0.75 s, respectively. Figures 2.2b, 2.2c, and 2.2d show the generalized S transforms of the signal for σ=1, 0.25, and 4, respectively. Figure 2.2c presents a better time resolution at the cost of the frequency resolution, whereas Figure 2.2d presents a better frequency resolution. This phenomenon, as explained earlier, is pertinent to the time-frequency expansion of the Gaussian window, which is controlled by the scaling factor σ. The generalized S transform (equation 2.4) is uniquely linked to the Fourier transform of h (Pinnegar and Mansinha, 2003a):

$$S_g[h(\tau)](t, f, \sigma) = \int_{-\infty}^{+\infty} H(\alpha + f) e^{-\frac{2\pi^2\sigma^2}{f^2}\alpha^2} e^{j2\pi\alpha\tau} d\alpha. \qquad f \neq 0, \tag{2.5}$$

where α is a frequency variable and

$$H(f) = \int_{-\infty}^{+\infty} h(\tau) e^{-j2\pi f\tau}\, d\tau \tag{2.6}$$

is the Fourier transform of $\mathrm{h}(\tau)$.

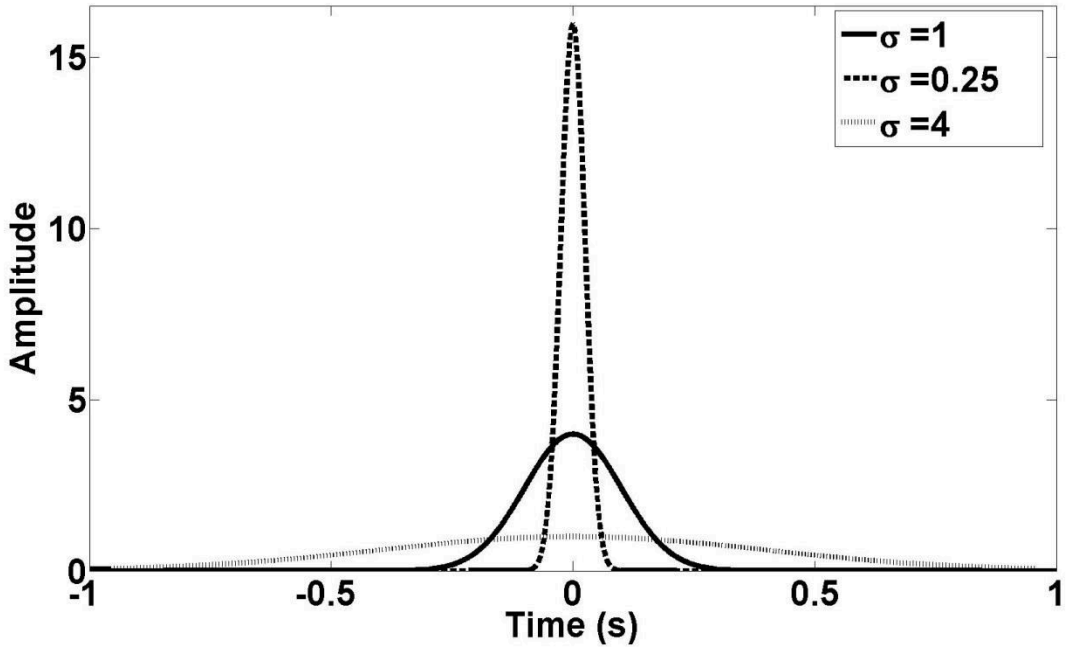

Figure 2.1 The Gaussian window at the frequency of 10 HZ for σ=1 (the solid line), σ=0.25 (the dashed line) and σ=4 (the hashed line).

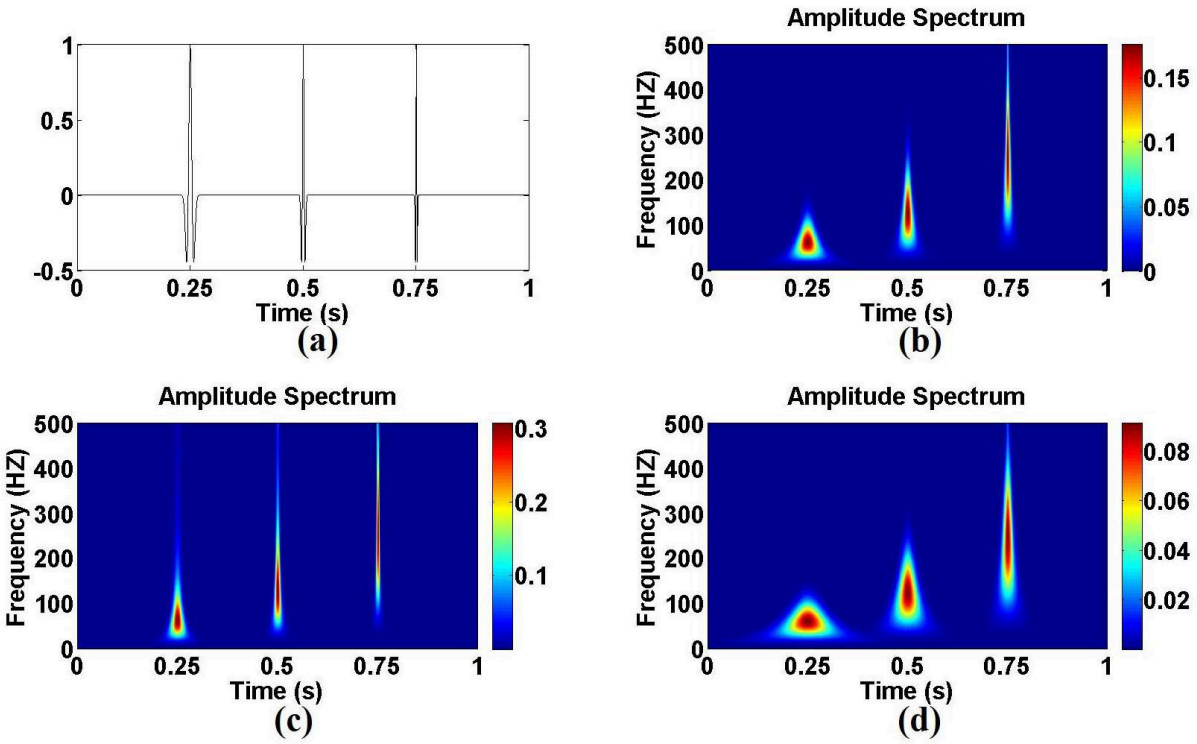

Figure 2.2 (a) A signal. (b), (c) and (d) the generalized S transforms of (a) for σ=1, 0.25 and 4 respectively.

2.4 The Wave Propagation Operator

If we assume a geometrical spreading correction to have been applied to the surface wave data, then the Fourier spectrum (H_2) of the wavelet $h_2(\tau)$ recorded at station 2 can be expressed in terms of the Fourier spectrum (H_1) of the wavelet $h_1(\tau)$ recorded at station 1 by

$$H_2(f) = e^{-\lambda(f)d} e^{-j2\pi k(f)d} H_1(f), \tag{2.7}$$

where $\lambda(f)$ is an attenuation function, and $k(f)$ are spatial wavenumbers that control wave propagation from station 1 to station 2. These wavenumbers characterize the horizontal propagation of surface wave and are a function of elastic properties of the medium, and d is the distance between the two stations. This relation is written in the S domain as

$$S_g[h_2(\tau)] = \int_{-\infty}^{+\infty} e^{-\lambda(f+\alpha)d} e^{-j2\pi k(f+\alpha)d} H_1(\alpha+f) e^{-\frac{2\pi^2\sigma^2}{f^2}\alpha^2} e^{j2\pi\alpha\tau} d\alpha. \tag{2.8}$$

Klush et al. (2005) assume that attenuation function $\lambda(f)$ and phase function $k(f)$ vary slowly with respect to the effective size of the spectrum of the wavelet transform. We make the same assumption for the generalized S transform in order to link the generalized S transforms of signals, which were recorded at different stations, to the wave propagation operators. For instance, for any fixed point (t, f) on the time-frequency plane, we may develop λ and k around the central frequency *f*. Assuming, the wavenumber term $k(f)$ on the right-hand side of equation 2.8 behaves linearly in the vicinity of *f* and attenuation function $\lambda(f)$ is constant in that vicinity where the vicinity is defined by the width of the Gaussian window. Therefore, $\lambda(f+\alpha)$ and $k(f+\alpha)$ can be expressed

$$\lambda(f+\alpha) = \lambda(f) + O(\alpha), \tag{2.9}$$

and

$$k(f+\alpha) = k(f) + \alpha k'(f) + O(\alpha^2), \tag{2.10}$$

where $k'(f)$ indicates a frequency derivative of $k(f)$. Upon inserting the above approximations into the integral (2.8), we obtain

$$\begin{aligned} S_g[h_2(\tau)](t,f,\sigma) &= \int_{-\infty}^{+\infty} e^{-\lambda(f)d} e^{-j2\pi(k(f)+\alpha k'(f))d} H_1(\alpha+f) e^{-\frac{2\pi^2\sigma^2}{f^2}\alpha^2} e^{j2\pi\alpha\tau} d\alpha \\ &= e^{-j2\pi k(f)d} e^{-\lambda(f)d} \int_{-\infty}^{+\infty} H_1(\alpha+f) e^{-\frac{2\pi^2\sigma^2}{f^2}\alpha^2} e^{j2\pi\alpha(\tau-k'(f)d)} d\alpha \\ &= e^{-j2\pi k(f)d} e^{-\lambda(f)d} S_g[h_1](t-k'(f)d, f, \sigma), \end{aligned} \tag{2.11}$$

where $S_g[h_1](t - k'(f)d, f, \sigma)$ is the generalized S transform of h_1 shifted by $-k'(f)d$. Considering

$$v_p(f) = f/k(f), \tag{2.12}$$

where v_p is phase velocity that is the velocity of each frequency component of surface wave, and also

$$v_g(f) = 1/k'(f), \tag{2.13}$$

where group velocity v_g is the velocity of a wave pocket (envelope) of surface wave around frequency *f*, equation 2.11 is expressed as

$$S_g[h_2(\tau)] = e^{-j2\pi f d/v_p(f)} e^{-\lambda(f)d} S_g[h_1(\tau)]\big(t - d/v_g(f), f\big). \tag{2.14}$$

Based on equation 2.14, any point at time-frequency plane (t, f) of station 2, is equivalent to the time shifted-frequency plane (t-$d/v_g(f)$, f) of station 1 with a phase difference of $-j2\pi f d/v_p(f)$, and with an amplitude that is proportional to $e^{-\lambda(f)d}$ that of station 1. Based on equation 2.14, it is possible to estimate the wavenumber, phase velocity, group velocity, and a frequency dependent attenuation from the generalized S transform. First of all, we find the time-frequency distribution of surface wave on the generalized S transform plane. Then, for every frequency, we find the maximum amplitude (ridge) of the generalized S transform, its corresponding time and corresponding unwrapped phase. Thus, the group velocity can be obtained from the time difference of the ridges of the transforms, the wavenumber and phase velocity can be estimated with respect to the phase difference of the ridges, and a frequency dependent attenuation can be calculated from the amplitude ratio of the ridges. Figure 2.3 is given to show how to use equation 2.14 in order to obtain the propagation parameters. Figures 2.3a and 2.3b are two synthetic traces recorded at two stations. Figures 2.3c and 2.3d show the amplitude spectra of the generalized S transform of station 1 and 2 respectively. Figure 2.3e and Figure 2.3f show their phase spectra respectively. At the first step, the ridges of the amplitude spectra of the transform are found (Figures 2.3c and 2.3d) at any specific frequency (here *f* =150Hz) with respect to the time axis. Attenuation is obtained as

$$\lambda(f) = [log(A_1(f)/A_2(f))]/d, \tag{2.15}$$

where A_1 and A_2 are the absolute, maximum amplitudes of the ridges of the stations receptively. Group velocity is obtained as

$$v_g(f) = d/\Delta t(f), \tag{2.16}$$

where $\Delta t = t_2 - t_1$ (from Figures 2.3c and 2.3d) is the time difference between two ridges. Wavenumber $k(f)$ is computed

$$k(f) = -\Delta\varphi(f)/2\pi d, \tag{2.17}$$

where $\Delta\varphi$ is the difference between the unwrapped phases at two ridges (Figures 2.3e and 2.3f). Finally phase velocity is calculated using equation 2.12.

Comparing equation 2.14 with that proposed by Kulesh et al. (2005) for the wavelet transform

$$W[h_2(\tau)] = e^{-j2\pi f d(\frac{1}{v_p(f)} - \frac{1}{v_g(f)})} e^{-\lambda(f)d} W[h_1(\tau)]\left(t - \frac{d}{v_g(f)}, f\right), \tag{2.18}$$

one observes that the phase velocity obtained from the generalized S transform is directly related to the phase spectrum because the phase in the generalized S transform is a localized value of the absolute phase with respect to the Fourier spectrum, whereas the phase in the wavelet transform. The phase in the wavelet transform is instant because the shapes of the real and imaginary parts of the wavelet do not change as the wavelet traverses the time axis, therefore the phase of the wavelet transform is different from the phase of the generalized S transform. Equation 2.14 takes advantage of calculating the phase velocity independently from the group velocity, so any error in calculating the group velocity does not impact on the estimation of phase velocity.

At first glance, the assumption applied in equations 2.9 and 2.10 might lead us to the conclusion that any propagation parameter estimation based on the generalized S transform would make sense only for wave propagation in weakly dispersive media at low frequencies where there is a linear phase process. In cases where the medium is highly dispersive, and a signal has a wide band of frequencies, there is high uncertainty to accurately estimate amplitude and phase spectra of high frequencies due to low frequency resolution which is indicated by Heisenberg boxes (Mallat, 1999). However, the generalized S transform improves frequency resolution of high frequencies by selecting a larger value of σ. So it provides a better estimation of amplitude and phase spectra of high frequencies. Thus it is able to estimate propagation parameters of surface wave for highly dispersive and attenuating media.

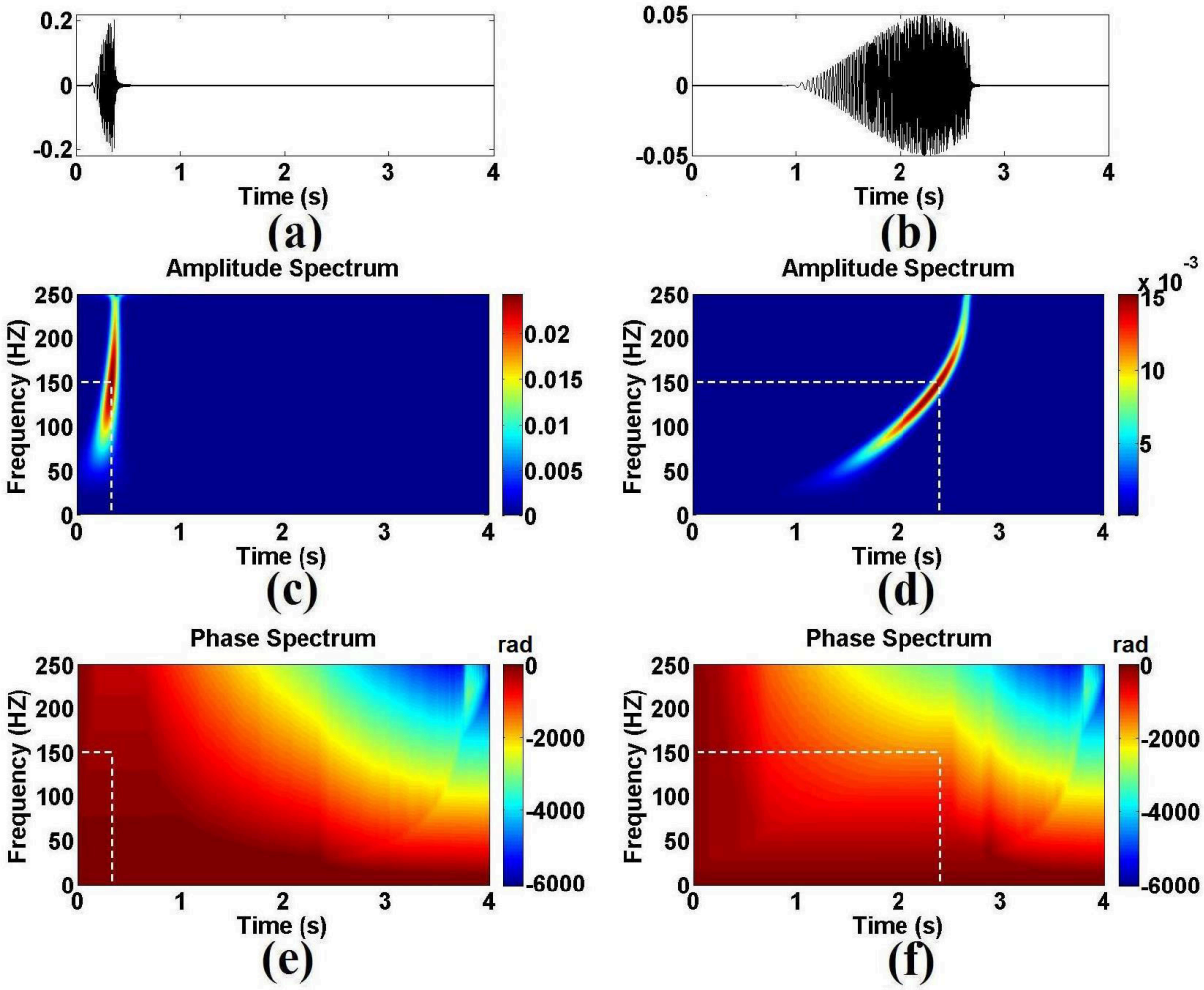

Figure 2.3 (a) and (b) Two synthetic traces. (c) The amplitude spectra of the first trace. (d) The amplitude spectra of the second trace. (e) The phase spectra of the first trace, and (f) the phase spectra of the second trace. The dashed line shows how the time and phase information of the ridges is estimated.

Figure 2.4 shows a wavelet signal dispersed in a relatively high dispersive medium with a dominant frequency of 125 Hz. Geophone spacing is 250 m. As seen in Figures 2.5a-d wavenumber, phase velocity and attenuation obtained using scaling factor σ=20 are poorly estimated for higher frequencies. This error implies the phase and amplitude spectra of high frequencies are poorly estimated. If a larger scaling factor is chosen, the Gaussian window expands in the time domain, and frequency resolution increases. So, we expect to improve results by choosing larger values for σ for this example. The hashed lines in Figure 2.5 show the estimated propagation operators based on σ=100. The wavenumber and phase velocity are now well estimated for all frequency components. The group velocity for lower frequencies (0-4 Hz)

is now poorly estimated due to low time resolution for low frequencies. But for higher frequencies, the result is acceptable. The estimated attenuation function is well computed for frequency ranges from zero to 220 Hz, and for frequency ranges from 220 Hz to 250 Hz, the attenuation function is underestimated. One approach to get a better estimation of the attenuation function is to select higher values of σ. When a higher value of σ is selected, the time resolution is weakened, so the possibility of the time-frequency overlap of higher modes increases. Thus, we are limited to choosing some specific values of σ in practice. Since the time resolution decreases with σ, there is a trade resolution for wavenumber and attenuation with that for group velocity. Therefore in general, σ may not be chosen too large. To compare amplitude and phase spectra of signals based on different values of the scaling factor, the amplitude and phase spectrum of traces (1) and (7) for scaling factors σ=20 and σ=100 are shown in Figure 2.6. For any dataset, an optimum value for σ is obtained using a cost function

$$E(\sigma) = \left\| S_{g_i}(t,f) - S_{g_r}\left(t - D_i/v_g(f), f\right) e^{-\lambda_{\sigma(f)} D_i} e^{-i2\pi k_\sigma(f) D_i} \right\|^2, \tag{2.19}$$

where $\lambda_\sigma(f)$ is the calculated attenuation and $k_\sigma(f)$ is the calculated wavenumber based on a specific value of σ respectively, S_{g_i} is the generalized S transform of the i^{th} geophone, S_{g_r} is the generalized S transform of a reference geophone which could be the first geophone and D_i is the distance between the reference and i^{th} geophones. Figure 2.7 shows the cost function for the data in Figure 2.4. As seen the cost function approaches zero for σ larger than 70. It implies we should choose σ larger than 70 to have good estimations of the attenuation and the wavenumber.

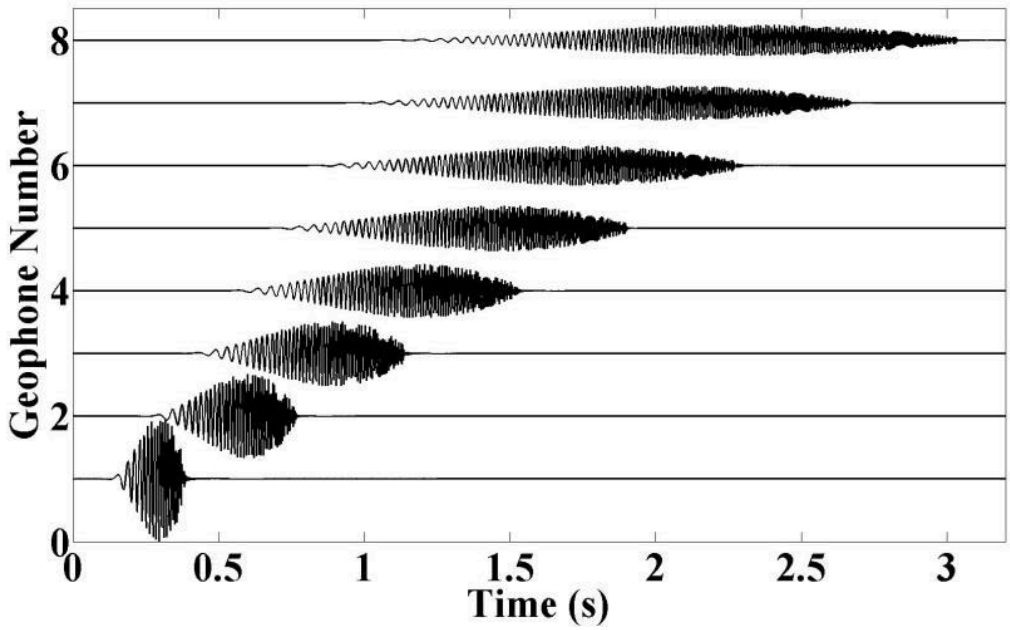

Figure 2.4 A wavelet signal dispersed in a relatively high dispersive medium recorded at different geophones.

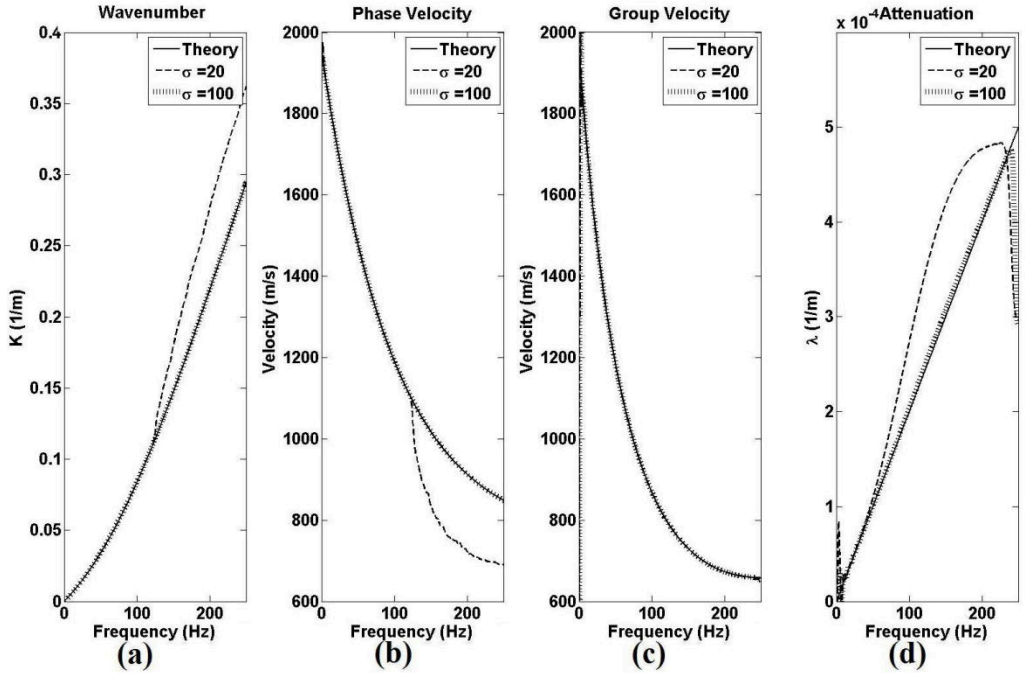

Figure 2.5 The estimated propagation model parameters based on the scaling factors σ=20 and σ =100. (a) The wave number. (b) The phase velocity. (c) The group velocity. (d) The attenuation function.

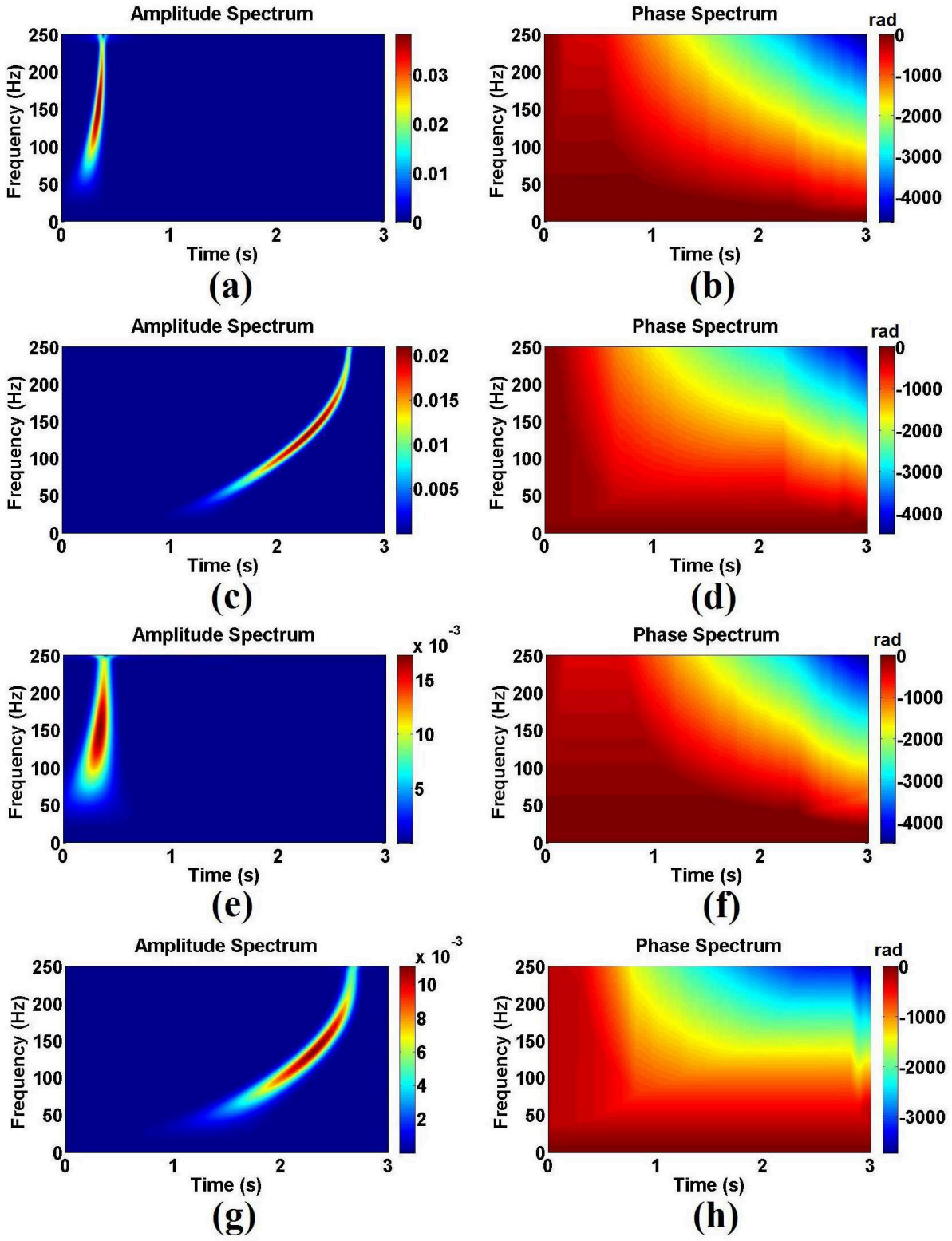

Figure 2.6 (a) and (c) The amplitude spectrum; (b) and (d) the phase spectrum for traces 1 and 7 respectively based on the scaling factor σ =20. (e) and (f) the amplitude spectrum; (g) and (h) the phase spectrum for traces 1 and 7 respectively based on the scaling factor σ =100.

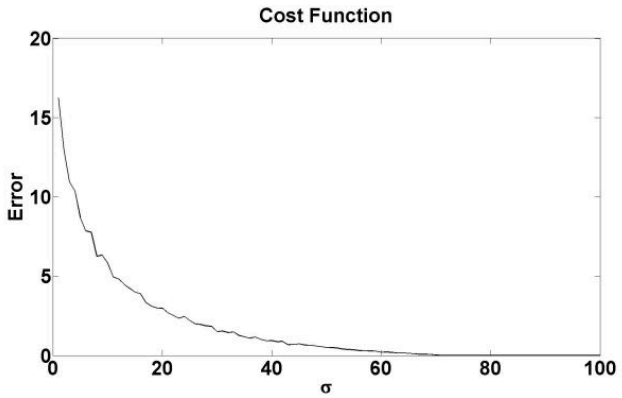

Figure 2.7 The cost function for the data in Figure 2.4.

Figures 2.8a and 2.8b show two dispersed synthetic data sets with different dispersivities. In the both models, a Ricker wavelet with a dominant frequency of 125 Hz is used as the seismic wavelet and geophone spacing is 250 m. Figures 2.8c and 2.8d show phase velocities for Figures 2.8a and 2.8b respectively. Phase velocity for Figure 2.8a ranges from 760 m/s to 850 m/s whereas the phase velocity ranges for Figure 2.8b ranges from 800 m/s to 1400 m/s. Therefore the second data set is more dispersed in comparison with the first data set. However it is less dispersed than the data used in Figure 2.4 where its phase velocity varies from 850 m/s to 1950 m/s. Figures 2.8e and 2.8f show the cost function for the both data sets respectively. The cost function for the first data converts to zero at $\sigma = 5$ and for the second data converts to zero at $\sigma = 22$. It can be concluded that for higher dispersive media, a higher value of σ should be chosen because when a medium is highly dispersive, the phase spectrum changes dramatically, therefore we have to increase the frequency resolution of the generalized S transform to correctly estimate the phase. In other words, σ is a function of data dispersivity.

Another approach that could be used is to include the updated group velocity in equation 2.18. Using this approach, it is expected to have a cost function with a minimum instead of a cost function that approaches zero for infinite σ. Therefore, the optimal σ compromises for estimating the different parameters, instead of only for wavenumber and attenuation. We do not use this approach because we experimentally have found that group velocity is less sensitive to σ than the wavenumber and attenuation (Figure 2.5c). Moreover, this approach increases the computational cost. Equation 2.18 could be only applied for the ridges of the transforms in order to find the optimum value for σ whereas the updated group velocity approach must be applied to any single point on the generalized S transform planes. Thus it is computationally expensive.

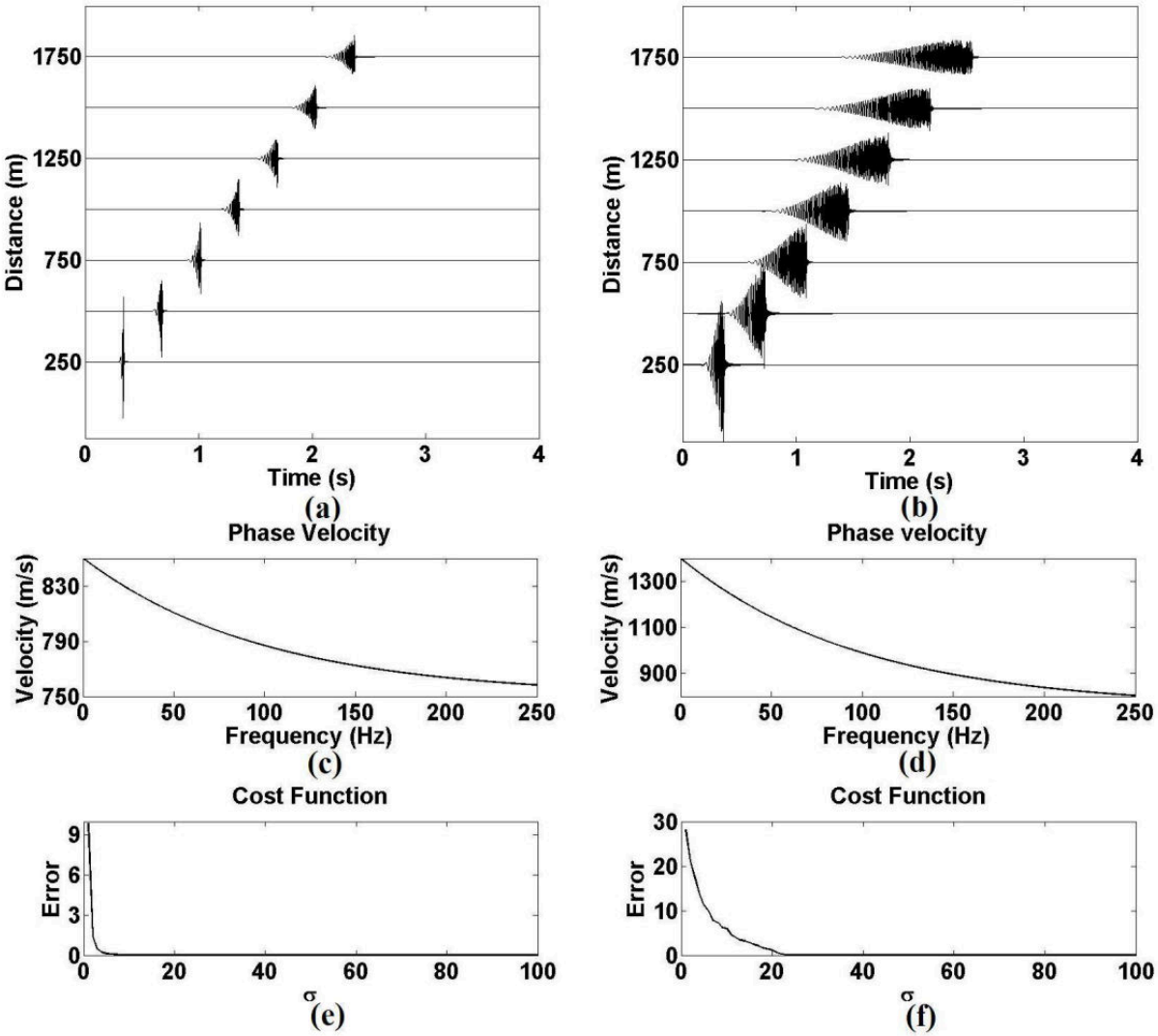

Figure 2.8 (a) and (b) Two different dispersed data sets; (c) and (d) the phase velocities for (a) and (b), respectively; (e) and (f) the cost functions for (a) and (b), respectively.

2.5 Examples

2.5.1 Synthetic Data Example

To investigate the noise effect on the estimation of propagation parameters, two synthetic seismic records are analyzed. In order to generate these models, we use equation (2.7) with an assumed wavenumber and frequency dependent attenuation to calculate the Fourier spectrum of the signals at different stations. Then, by calculating the inverse of the Fourier transform, we obtain the synthetic signals in the time domain. We expect where the signal to noise ratio is small

at low frequencies, there is a wavenumber perturbation. Therefore the wavenumber and consequently phase velocity are not well estimated (the second model). The signal to noise ratios of the both models are equal to five. In the first model (Figure 2.9), a Gaussian wavelet with standard deviation 7×10^{-3} s is used. The additive noise is white Gaussian with a standard deviation of $1\text{x}10^{-2}$ s, and where the geophones are irregularly spaced. The average distance between two adjacent geophones, however, is set to be 200 m. In the second model (Figure 2.10) a Ricker wavelet with dominant frequency 22.5 Hz is used. All other parameters are identical with that used in the first model. The theoretical propagation parameters correspond to the solid lines in Figure 2.11. The dashed lines in Figure 2.11 are the estimated parameters obtained from the first model. As may be seen in Figure 2.11, the wavenumber and the phase velocity are well estimated in comparison with the theoretical values for the first model. The group velocity and the attenuation function are relatively well estimated around low frequencies where the Gaussian wavelet has more energy (Figure 2.12). The estimated group velocity, however, seems distorted around zero frequency. Because the calculated group velocities are highly distorted and poorly estimated around zero frequency, we do not calculate them for those frequency ranges in Figure 2.11(c). As explained earlier, it can be referred to low time resolution at low frequencies. When the signal to noise ratio is small, the attenuation is poorly estimated. In model 1, there is a large difference (over 100%) between the estimated and theoretical attenuation coefficients around 25 Hz. This can be explained with respect to the amplitude spectra of the Gaussian wavelet (Figure 2.12). For the Gaussian wavelet most energy is concentrated around zero frequency therefore the signal to noise ratio becomes small at higher frequencies such as 25 Hz. Consequently the attenuation is poorly estimated at those frequencies. The dotted lines in Figure 2.11 are the estimated propagation parameters for model 2. The estimated wavenumber and phase velocity are not consistent with the theoretical values. The wavenumber of the model (k_m) can be expressed as approximately equal to the estimated wavenumber (k_e) plus perturbation according to

$$k_m \approx k_e + \varepsilon. \tag{2.20}$$

Equation 2.20 can be explained by the effect of noise at low frequency components where the signal to noise ratio is small because the Ricker wavelet has less energy at low frequencies (Figure 2.12). At those frequencies, initial values of phase (φ_0) are highly affected by noise, hence, when we unwrap the phase at low frequency, the phase calculation is affected by the

phase of the noise, consequently a constant φ_n which is related to the phase of noise at low frequencies will be added to the calculated unwrapped phase. Therefore, phase difference between two geophones is not directly proportional to the wavenumber. The group velocity and the attenuation function are better estimated around frequency 22.5 Hz where signal to noise ratio is high. The group velocity is more highly distorted around zero frequency due to the small amount of signal to noise ratio and also low time resolution at low frequencies.

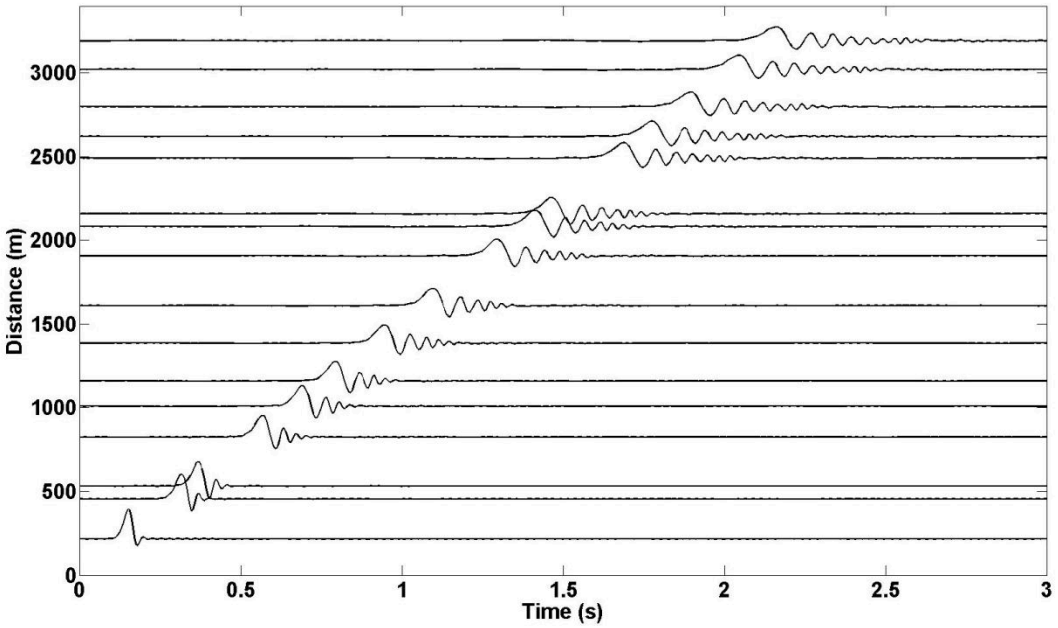

Figure 2.9 A noisy synthetic seismic record with a dispersive Gaussian wavelet.

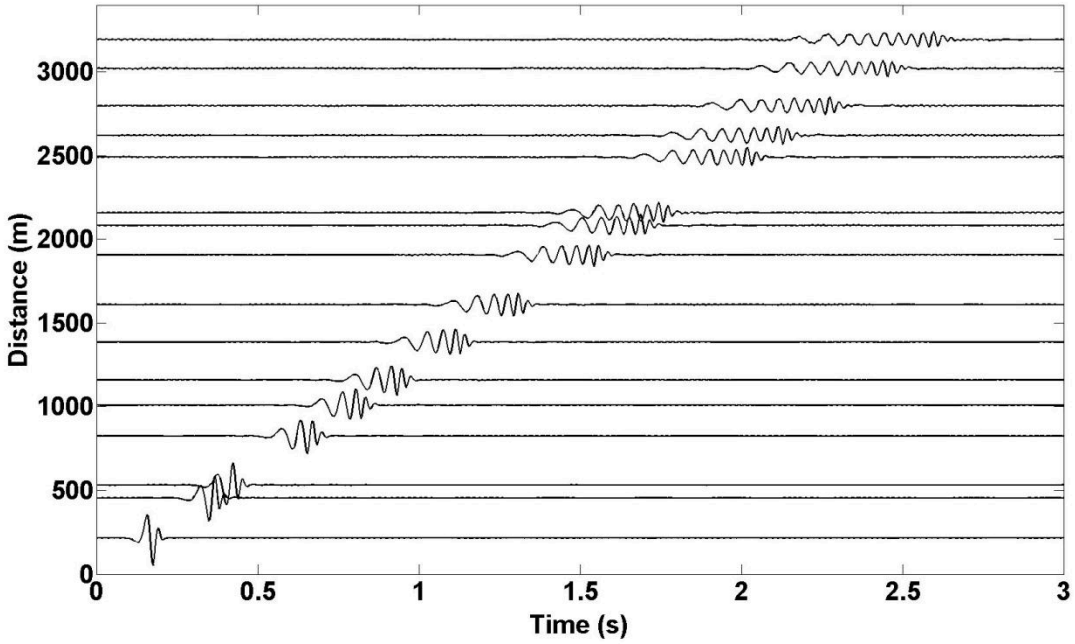

Figure 2.10 A noisy synthetic seismic record with a dispersive Ricker wavelet.

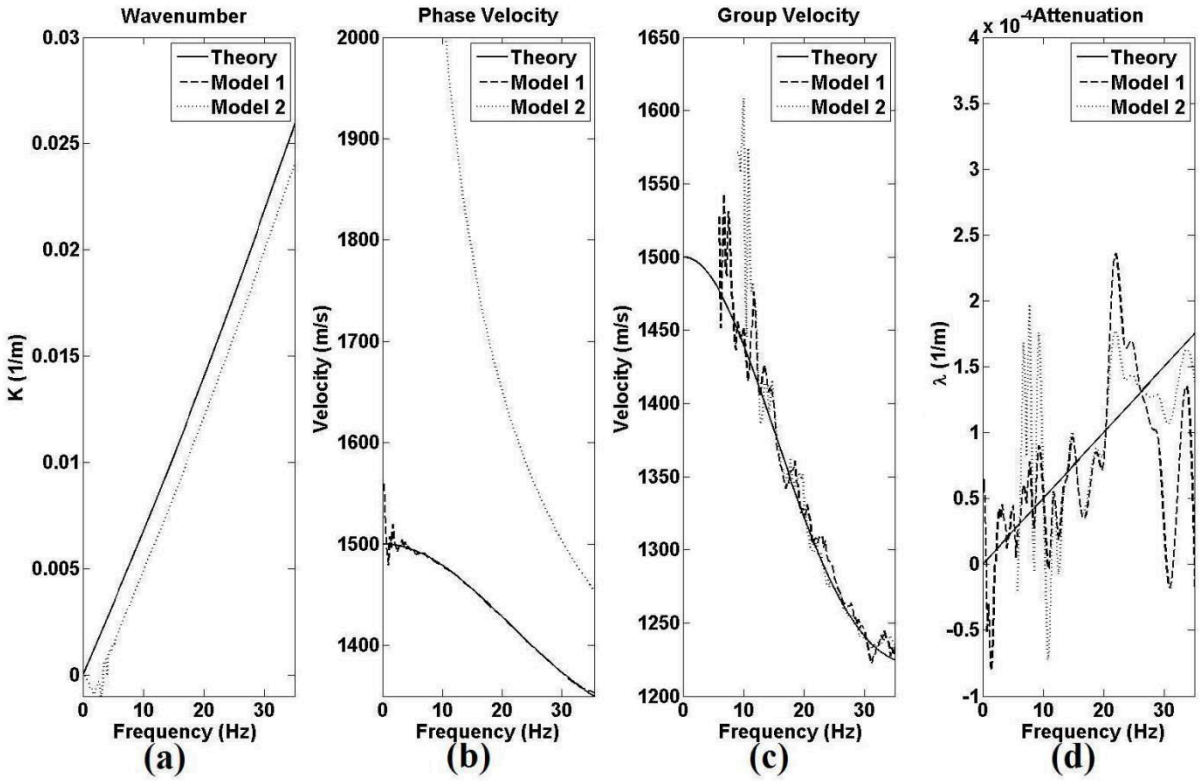

Figure 2.11 The propagation model parameters. (a) The wavenumber. (b) The phase velocity. (c) The group velocity. (d) The attenuation function.

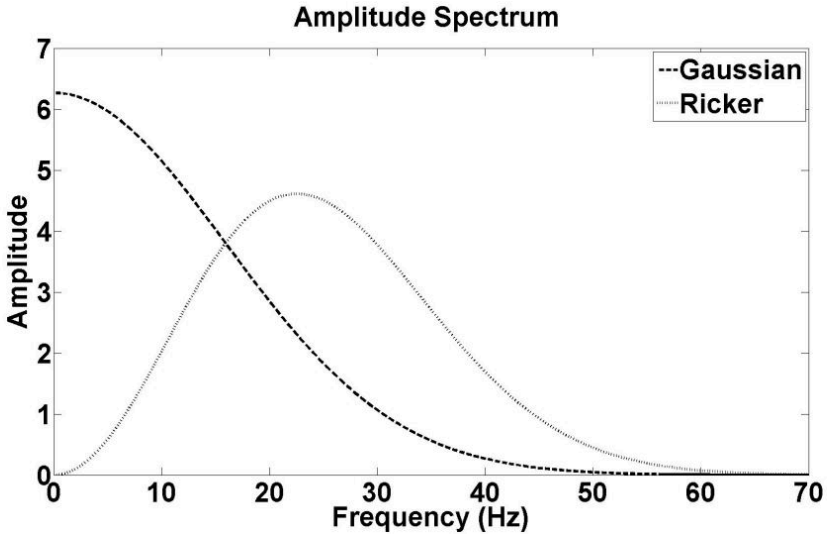

Figure 2.12 The amplitude spectrum of the Gaussian wavelet (the dashed line) and the Ricker wavelet (the dotted line).

The problem can be solved using the least squares solution by finding an appropriate value for wavenumber perturbation ε. The assumption is $|\varepsilon| \ll 1$. The cost function is to be minimized is

$$E(\varepsilon) = \left\| S_{g_i}(t,f) - S_{g_r}\left(t - D_i/v_g(f), f\right) e^{-\lambda(f)D_i} e^{-i2\pi k_e(f)D_i} e^{-i2\pi\varepsilon D_i} \right\|^2, \quad (2.21)$$

where S_{g_i} is the generalized S transform of the i^{th} geophone, S_{g_r} is the generalized S transform of a reference geophone which in this study the first geophone is assumed as the reference and D_i is the distance between the reference and i^{th} geophones. Figure 2.13 show the error function for $0<\varepsilon<.1$. The cost function is highly non-linear and has a lot of local minima, so it is impossible to solve it using some gradient methods such as Steepest Descent or Conjugate Gradient. In this chapter, Simulated Annealing (Beaty et al., 2002) is used to find an optimum value for epsilon. Each step of Simulated Annealing replaces the current solution by a random "nearby" solution, chosen with a probability that depends on the difference between the corresponding cost function values and on a global parameter (called the temperature), that gradually decreases during the process. For the second model, the optimum value of $\varepsilon = 1.89\times10^{-3}$ is obtained. Figure 2.14 shows the wavenumber and the phase velocity corrected based on the computed value for epsilon. The corrected wavenumber and corrected phase velocity match very well with that of the theoretical.

The reason why the geophones are assumed to be irregularly spaced is that for distances larger than 100 m, it is possible to find many values of small epsilons minimizing equation 2.21. For instance, if the distance between two adjacent geophones is 100 m, "$\varepsilon + .01$" will give the same amount of error as epsilon because the multiplication of .01 by the distance will produce an integer multiple of 2π. Therefore in order to have a unique value for epsilon where geophone spacing is more than 100 m, data must be irregularly sampled.

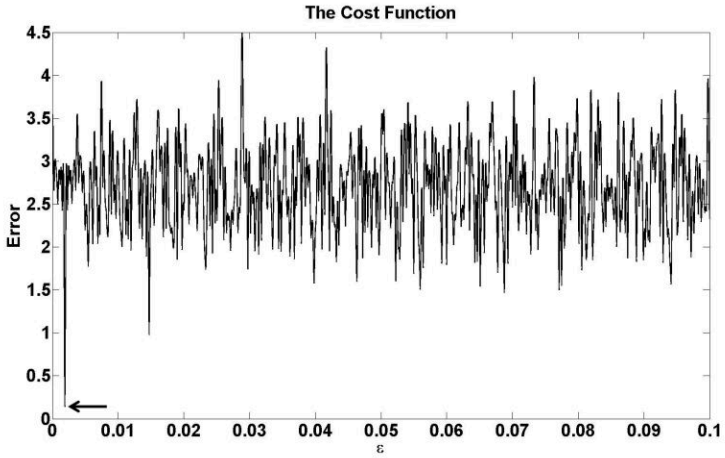

Figure 2.13 The cost function for $0<\varepsilon<.1$

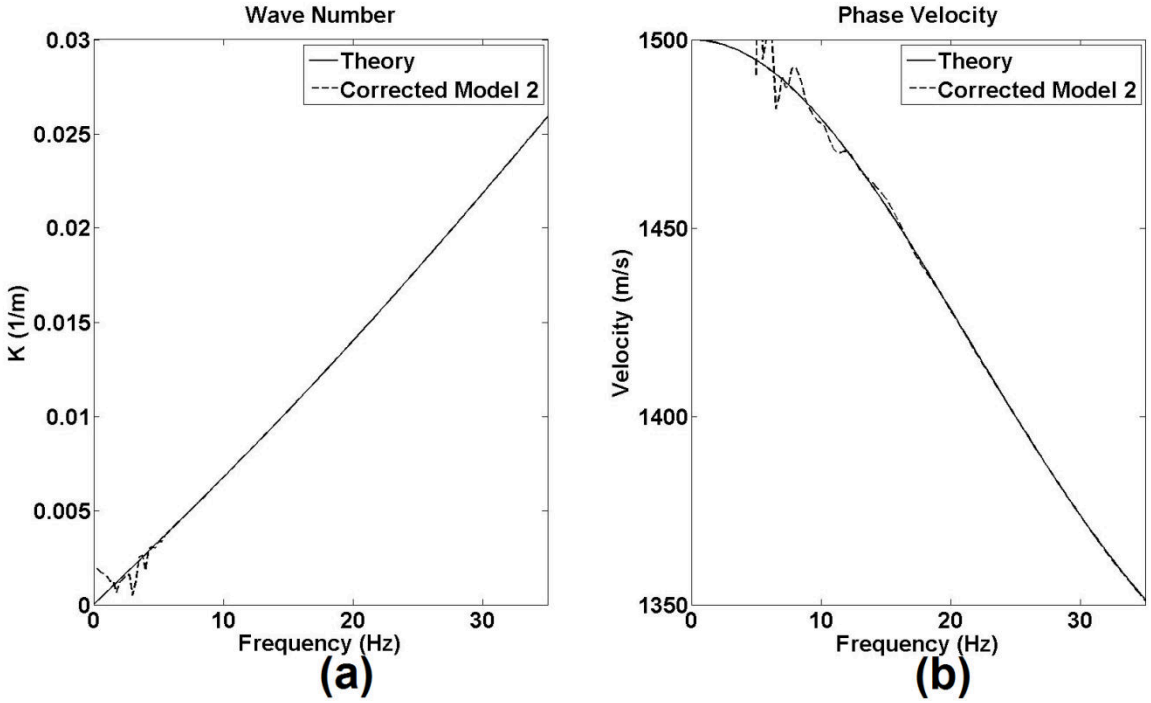

Figure 2.14 (a) The wavenumber. (b) The phase velocity corrected based on computed optimum value for ε.

2.5.2 Real Data

The real data used in this study was acquired from the foothills of the Canadian Rocky Mountains, southern Alberta at the University of Calgary's Rothney Astrophysical/Geophysical Observatory. The source is an IVI Envirovibe (18,000 lb) sweeping from 10 to 250 Hz with an eleven second listen time and a four times vertical stack. The receivers are 10 Hz 3-C geophones. We use the vertical component for ground roll dispersion analysis. Figure 2.15 (solid lines) shows the real data consisting of dispersive ground roll with sampling frequency 1000 Hz and sampling distance one meter. Figure 2.16 shows the estimated propagation parameters obtained from the generalized S transform processing. The estimated phase, group and attenuation are in a reasonable range for near-surface materials (.e.g. Xia et al., 2002c, Kulesh et al., 2005, Holschneider et al., 2005). We note here that the calculated attenuation is comparable with some near surface study results for these ranges of frequency (.e.g. Xia et al., 2002c, Kulesh et al., 2005, Holschneider et al., 2005). There are some small fluctuations on the calculated attenuation which can be referred to the effect of noise. We see this effect (small fluctuations on the calculated attenuation) on the synthetic data example too. The attenuation at 30 Hz is smaller than that at 15 Hz. It can be concluded that there is a near surface layer with smaller attenuation than deeper layers. The estimated group velocity at the frequency ranges from 15 Hz to 35 Hz differs significantly from the phase velocity. The estimated group velocity is less than the phase velocity. The trend of the group velocity is also different from that of the phase velocity. Other authors report similar group velocity ranges and trends for near surface studies (e.g. Kulesh et al., 2005 and Holschneider et al., 2005). For visual comparison, we generate synthetic traces for each geophone location. We use trace 1 (from geophone 1) as the source term, and we estimate traces for geophones 2 through 10 based on the inversion estimates of attenuation and wavenumber. The predicted traces (the hashed lines in Figure 2.15) are well matched to the real data implying good estimations of the wavenumber and attenuation function.

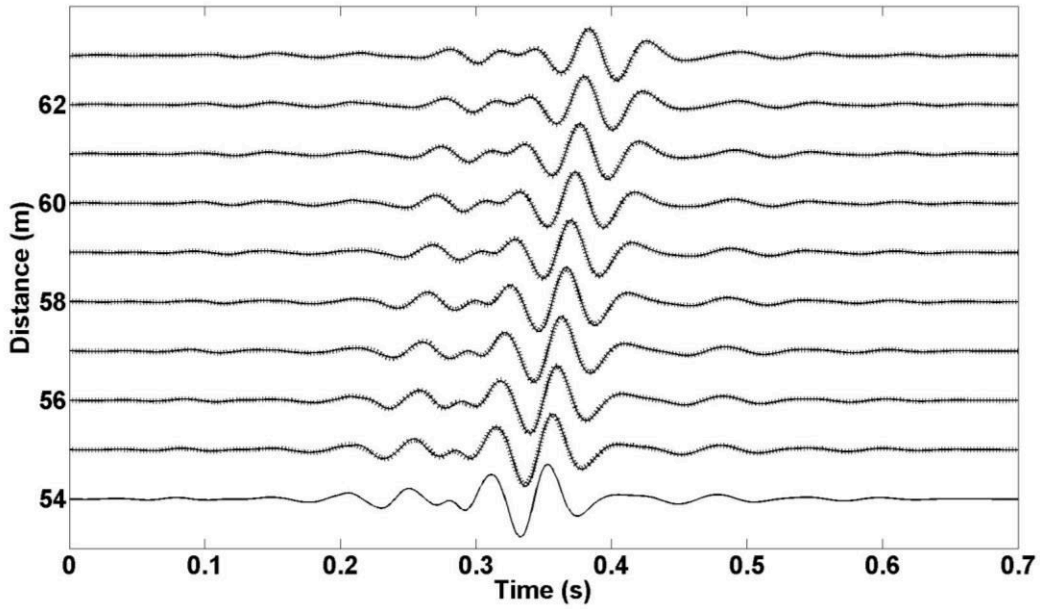

Figure 2.15 The real data (the solid lines) and the predicted (the hashed lines).

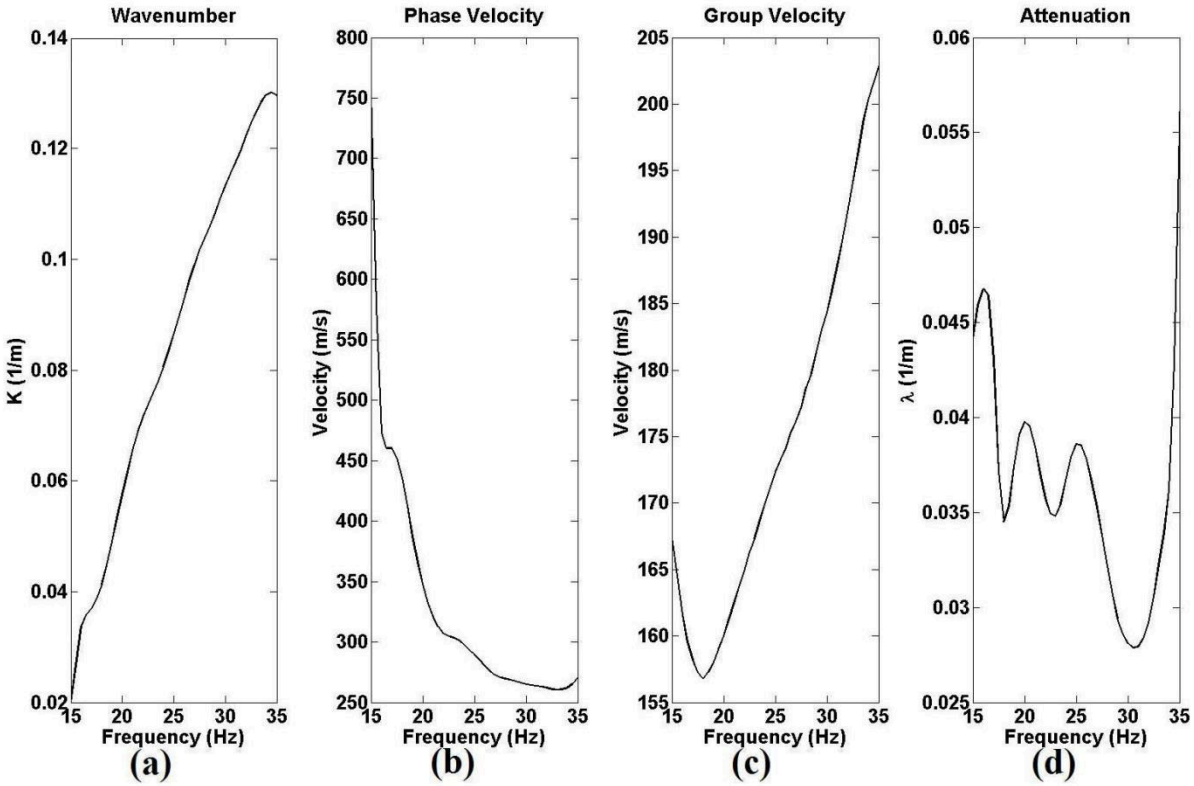

Figure 2.16 Estimated propagation model parameters of the real data. (a) The wavenumber. (b) The phase velocity. (c) The group velocity. (d) The attenuation function.

2.6 Conclusions

In this chapter we use a mathematical model to link the time-frequency spectrum of a signal based on the generalized S transform to its propagation parameters (wavenumber, phase velocity, group velocity and attenuation function) in dispersive and attenuating media. The S transform and its generalized versions provide frequency-dependent resolution while maintaining a direct relationship with the Fourier spectrum. Using this property, wavenumber and phase velocity are obtained directly from the absolute phase value of the ridges of the *S* domain. Group velocity is also computed from the time difference of the ridges of the transform. Finally, frequency-dependent attenuation is estimated by the absolute amplitudes of the ridges of the transform. The advantage of the generalized S transform over the S transform lies in the fact that it manipulates time-frequency resolution in the S domain using a scaling factor. Therefore results can be improved, especially for a highly dispersive and dissipative medium. According to the results of the synthetic data, for a highly dispersive medium, a larger value of the scaling factor must be chosen. In general, estimated parameters are more reliable where signal to noise ratio is high. However, group velocity estimated for frequency ranges (0-5) Hz is not satisfactory due to low time resolution of the transform at low frequencies. This limits the ability of the method to determine the group velocity at mentioned frequency ranges for station separations typical in near-surface exploration.

In reality, a seismic signal usually consists of several modes of surface waves. If time-frequency spectrum of different modes of the signal in the *S* domain is well separated, it is quite possible to simultaneously extract the propagation factors of different modes with respects to their time-frequency distributions. However, we are usually limited to choosing an appropriate scaling factor due to overlapping time-frequency spectrum of different modes for specific values of the scaling factor. We introduce a cost function to estimate a minimum optimum value for the scaling factor. We could make decision what ranges of the scaling factor should be chosen based on the minimum value of the scaling factor and also overlapping time-frequency spectrum of different modes.

Experimentally we find that estimated wavenumber is perturbed for noisy data when signal to noise ratio is small at low frequencies. As a remedy, we estimate wavenumber perturbation by minimizing a cost function using Simulated Annealing. For receiver spacing

larger than 100m, receivers must be irregularly deployed to have a unique answer for the cost function.

Chapter Three: Group Velocity Estimation by Slant Stack in the Generalized S Transform Domain

3.1 Overview

We present a new method by which we estimate surface-wave group velocity using surface wave dispersion curves. Based in the generalized S transform domain, we use slant stacking to identify the linear events that correspond to multi-modal surface waves. To ensure optimal resolution, we introduce a scaling factor into the generalized S transform that we use to control spectral localization. We find that, a smaller scaling factor should be chosen for low frequency surface wave, whereas, for higher frequencies, a larger scaling factor should be chosen. We show the application of the method for the estimation of the group velocity for synthetic and real data, and we also estimate a near surface shear wave velocity model for the real data based on our estimated group velocity. We find that the model is well matched to another model separately obtained from a phase velocity estimated.

3.2 Introduction

Askari and Ferguson (2012) estimate the phase and group velocity of surface waves simultaneously through a mathematical model that is based on the generalized S transform (Pinnegar and Mansinha 2003). Though Askari and Ferguson's (2012) method is robust especially where the surface wave is highly dispersed, parameterization within the method becomes ambiguous when the surface wave is multi-modal. Multi-modal means that there is more than one mode in short period surface wave data, and this can make the analysis of surface waves difficult (Herrmann 1973).

Following Pinnegar and Mansinha (2003a), we note that the generalized S transform returns a three dimensional analysis domain (time, frequency and offset) when given a two dimensional gather (a shot gather for example). At each constant frequency f in the time, frequency and offset domain, we have a 2D common frequency gather in time and offset coordinates, and multi-modal surface waves appears there as linear events. The group velocity of each member of this set of multi-modes (the fundamental mode plus the higher modes) corresponds to the apparent velocity of the linear events. To estimate each linear velocity, we use slant stacking (Yilmaz, 1987) to transform the time and offset coordinates to intercept time and slowness coordinates. The fundamental and higher modes intercept at time T=0, so the group velocity of each mode at each frequency is determined by picking the slowness and then

calculating the inverse of the picked slowness. Using this process, we create a 2D image of the group velocity for all ranges of frequency.

A convenient property of the generalized S transform is its spectral localization and this is optimized through the use of a scalar. This localization allows us to manipulate the time-frequency resolution of the transform and therefore the group velocity resolution. We find that a small scalar enhances the time resolution of the transform, and we use this property to optimize the group velocity estimation for the low frequency components of the surface waves. Conversely, we find that a large scaling factor improves the frequency resolution of the transform and we use this to optimize the group velocity estimation for the high frequency components of surface waves. In this chapter, we demonstrate the application of our slant stack method using synthetic and real data examples, and we also estimate a near surface shear wave velocity model for the real data based on our estimated group velocity. We find that the model is well matched to another model separately obtained from through the inversion of the phase velocity.

3.3 The generalized S transform and the wave propagation operator

As mentioned in Chapter 2, the S transform (Stockwell et al., 1996) is very similar to the familiar Gabor transform (Gabor, 1946). It provides a time dependent frequency distribution of a signal, and a Gaussian window is utilized for spectral localization. The S transform differs from the Gabor transform, in that the Gaussian window is scalable with frequency, and we use this property to enhance the time-frequency resolution. We can generalize the S transform in order to manipulate the time-frequency resolution (Pinnegar and Mansinha, 2003a). In this chapter, we use the same version of the generalized S transform used in Chapter 2 in order to estimate the group velocity of multi-modal surface wave.

Following Askari and Ferguson (2012), the generalized S transform of the signal at station 2 is linked to the signal at station 1 according to equation 2.14. Based on equation 2.14, any point in the time-frequency plane (t, f) of station 1 is equivalent to the time shifted-frequency plane (t-$d/v_g(f), f$) of station 2 and a phase difference of $-j2\pi fd/v_p(f)$, and the amplitude at station 2 is proportional to $e^{-\lambda(f)d}$ times the amplitude of station 1 (Askari and Ferguson, 2012). Thus, the group velocity can be obtained from the time difference of the ridge of the transforms for any frequency (Askari and Ferguson, 2012). As an example in Chapter 2, Figures 2.3a and 2.3b show two synthetic traces for two stations, and Figure 2.3c and Figure 2.3d show their

amplitude spectra respectively. The ridges of the amplitude spectra of the transform are picked (Figures 2.3c and 2.4d) for any specific frequency (here f =150 Hz) with respect to the time axis. The group velocity is then obtained from equation 2.16.

In reality, a seismic record is composed of multi-modal surface waves, and the estimation of the group velocity is not as straightforward as equation 2.16. Therefore, in order to apply the method to multi-modal data, we introduce the slant stack generalized S transform.

3.4 The slant stack generalized S transform

A wavefield such as a common shot gather can be transformed from the offset-time domain to the intercept time-slowness domain by applying linear moveout to the data gather U and summing amplitudes over the offset axis (Yilmaz, 1987). The linear moveout step is

$$U(x,T) = U(x,T = t - sx), \tag{3.1}$$

where T is intercept time, s is slowness and the stacking step is

$$P(s,T) = \sum_x U(x,T = t - sx), \tag{3.2}$$

where P is the slant stack of the data. Using the slant stack, we can estimate the apparent velocities or slownesses of linear events with respect to their intercept times. We use this property in the generalized S transform to estimate the group velocities of multimodal surface wave. If we calculate the amplitude spectrum of the generalized S transform of all traces in a record, we make a cube whose axes are time, offset and frequency (Figure 3.1). If we cut off the frequency axis at any frequency (the red line in Figure 3.1), there is a 2D amplitude function of time and distance which is relatively similar to a seismic record. We call the 2D amplitude function a pseudo-seismic record. We empirically find that at each pseudo-seismic record, multi-modal surface waves can be observed as linear events. According to equation 2.14, the relative time differences of the ridges of the amplitude spectrum of the generalized S transform of the surface wave at different stations provide the group velocity information. Therefore, the apparent velocities of the linear events correspond to group velocities and we can estimate the group velocity of the multi-modal surfaces by slant-stacking the pseudo-seismic record. In this study we call this approach "*Slant Stack Generalized S transform Method*".

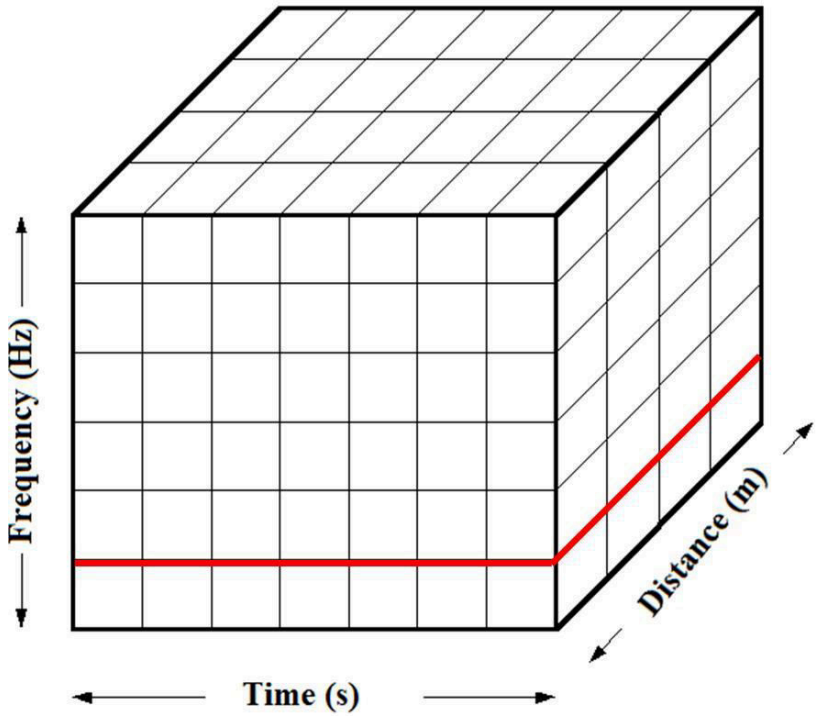

Figure 3.1 A cube whose axes are time, frequency and distance. The generalized S transform returns a three dimensional analysis domain (time, frequency and distance) when given a two dimensional gather (a shot gather for example).

Figure 3.2 shows a synthetic record composed of bimodal surface wave. We use the approach in 2.5.1 to generate the synthetic data. The amplitude spectrum of the generalized S transform is calculated for the first trace (Figure 3.3a). For any specific frequency such as 50Hz (in the amplitude spectrum of the generalized S transform), we observe a one dimensional amplitude function of time which relatively looks similar to a seismic trace (Figure 3.3b). We call this amplitude function a pseudo-seismic trace. By calculating the generalized S transform for all traces and putting together all of the pseudo-traces from them, we make a pseudo-seismic record for that frequency (Figure 3.4). According to Figure 3.4, the apparent velocity of the surface wave can be estimated by applying the slant stack transformation. Figure 3.5a shows the slant stack of the pseudo-seismic record in Figure 3.4. We show the slant stack in the intercept-time-velocity domain instead of the intercept-time-slowness domain for giving a better understanding of the velocity ranges of the group velocity. Because surface waves are generated and initiated from a source point, all harmonics from different modes (the fundamental mode plus higher modes) intercept at $T=0$. Therefore, we can estimate the group velocity for any frequency based on the estimated velocity at $T=0$ in the slant stack domain (Figure 3.5b). The

group velocities of the fundamental and first higher modes are 180 m/s and 550 m/s respectively. There is increased uncertainty in the estimated velocity of the first higher mode because, when a linear event has a higher velocity, the slant stack provides more velocity uncertainty (Yilmaz, 1987). We make a 2D image of the group velocity of the surface wave by putting together all the velocities, estimated at intercept time T=0, for all frequencies. Figure 3.6 shows the group velocity of the record in Figure 3.2 based on the scaling factor σ=2. The group velocity is well estimated for frequencies smaller than 120Hz because the local maxima of the group velocity are well matched to the theoretical values of the group velocity (the solid line). However, the estimated group velocity for frequencies larger than 120Hz is overestimated. This is due to the frequency uncertainty of the generalized S transform at higher frequencies and this can cause error in our estimates of the ridges within the transform. In order to better estimate the group velocity for higher frequencies, a larger scaling factor should be chosen. Figure 3.7 shows the group velocity based on a scaling factor σ=7. In this case, the group velocity for higher frequencies is better estimated comparatively with the case σ=2 because there is a better match between the local maxima of the group velocity and the theoretical values of the group velocity (the dashed line). However, at low frequencies, especially for frequencies below 50 Hz, the group velocity resolution is weakened due to the low time resolution of the generalized S transform for low frequencies for larger scaling factors. Figure 3.8 shows the group velocity based on the scaling factor σ=20. The estimated group velocity is now better estimated compared to that of the scaling factors σ=2 and σ=7, but, for low frequencies, the resolution is weaker. Therefore, there is a tradeoff between the group velocity resolution of low frequencies when a small scaling factor is chosen and that of high frequencies when a large scaling factor is chosen.

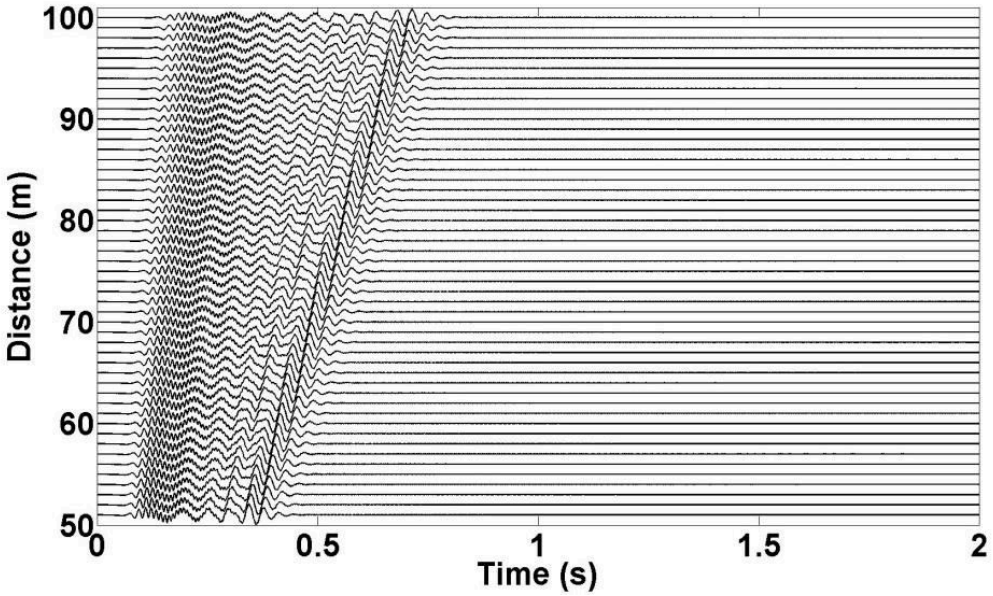

Figure 3.2 A synthetic data containing a two modal surface wave.

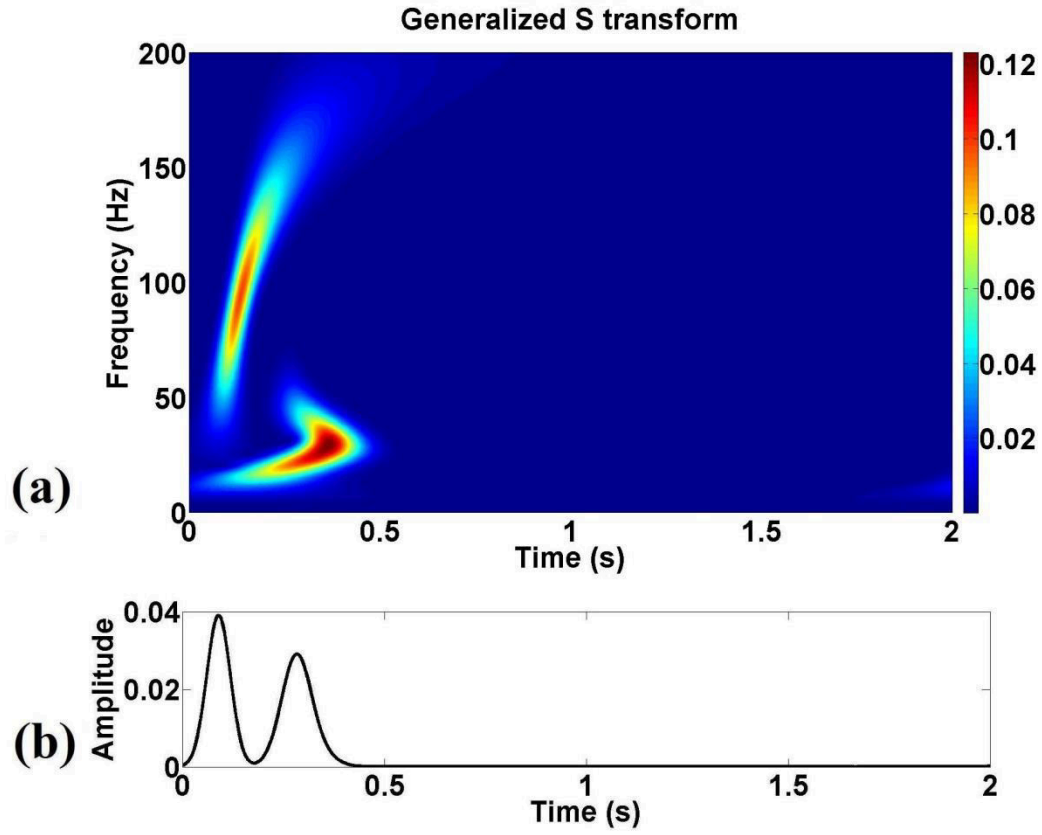

Figure 3.3 (a) The amplitude spectrum of the generalized S transform of the first trace in Figure 3.2. (b) Time representation of the amplitude spectrum of the generalized S transform at the single frequency 50Hz.

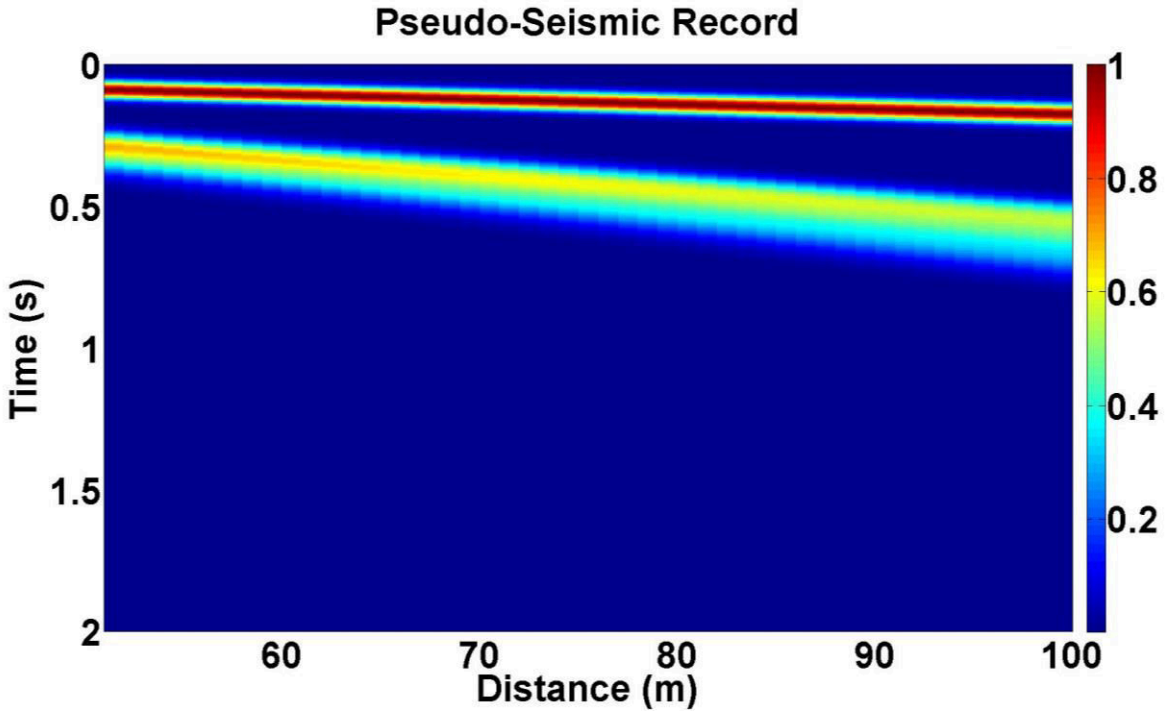

Figure 3.4 A pseudo-seismic record based of the generalized S transform of the traces of the record in Figure 3.2 at Frequency=50Hz.

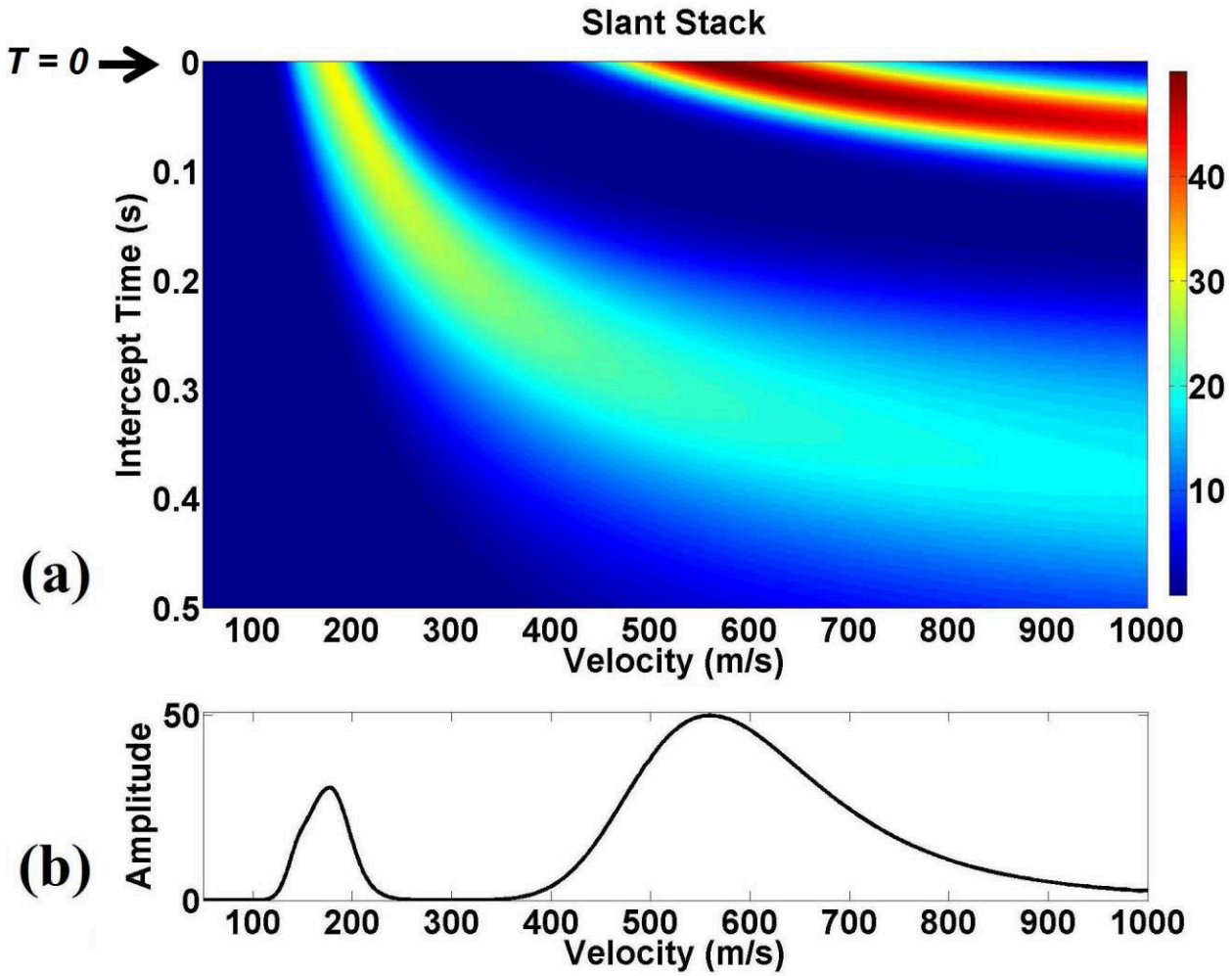

Figure 3.5 (a) The slant stack of the pseudo-record in Figure 3.4. (b) Single representation of the slant stack at intercept time T=0.

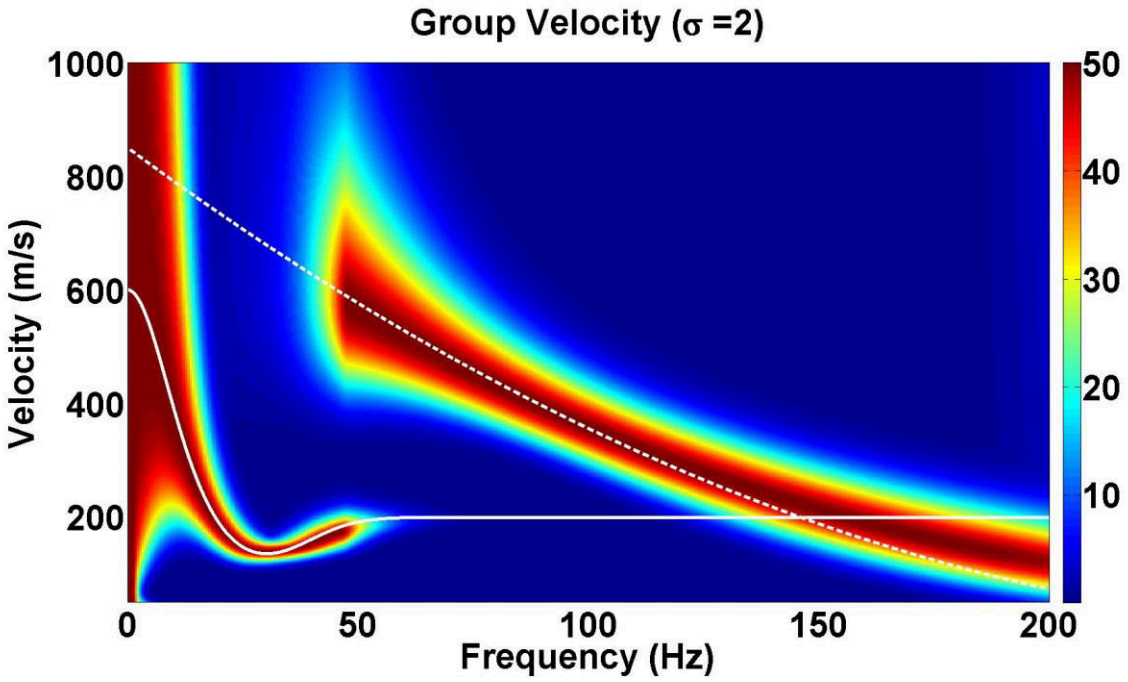

Figure 3.6 The estimated group velocity for the record in Figure 3.2 based on the scaling factor σ=2. The solid and dashed lines correspond to the theoretical values.

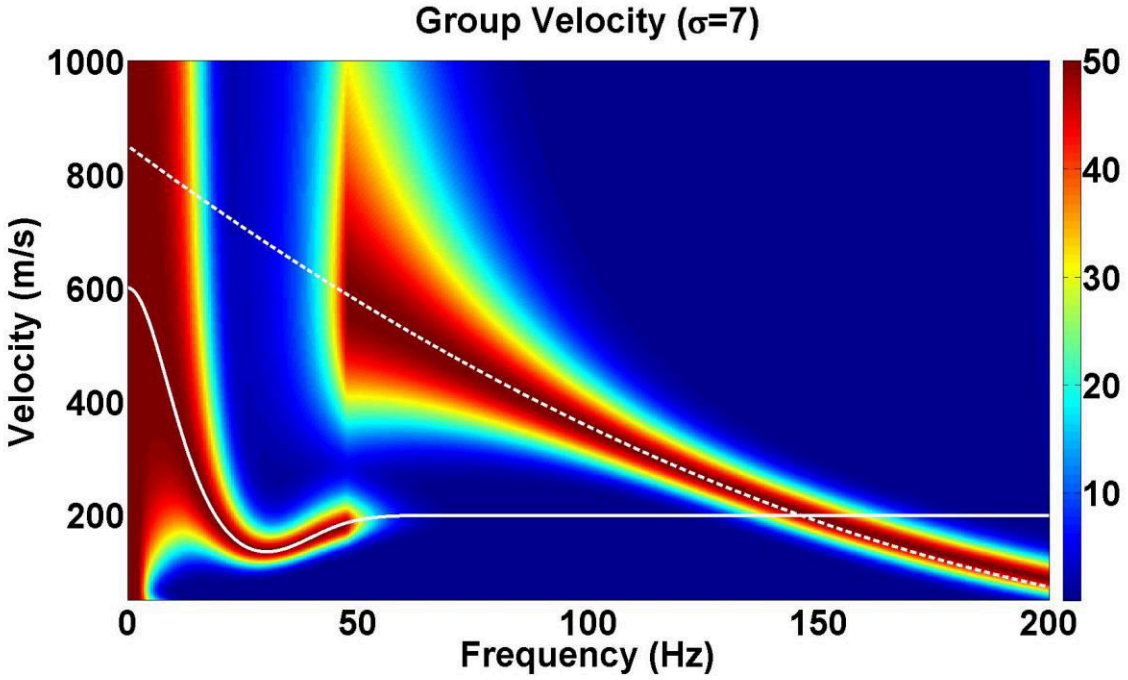

Figure 3.7 The estimated group velocity for the record in Figure 3.2 based on the scaling factor σ=7. The solid and dashed lines correspond to the theoretical values.

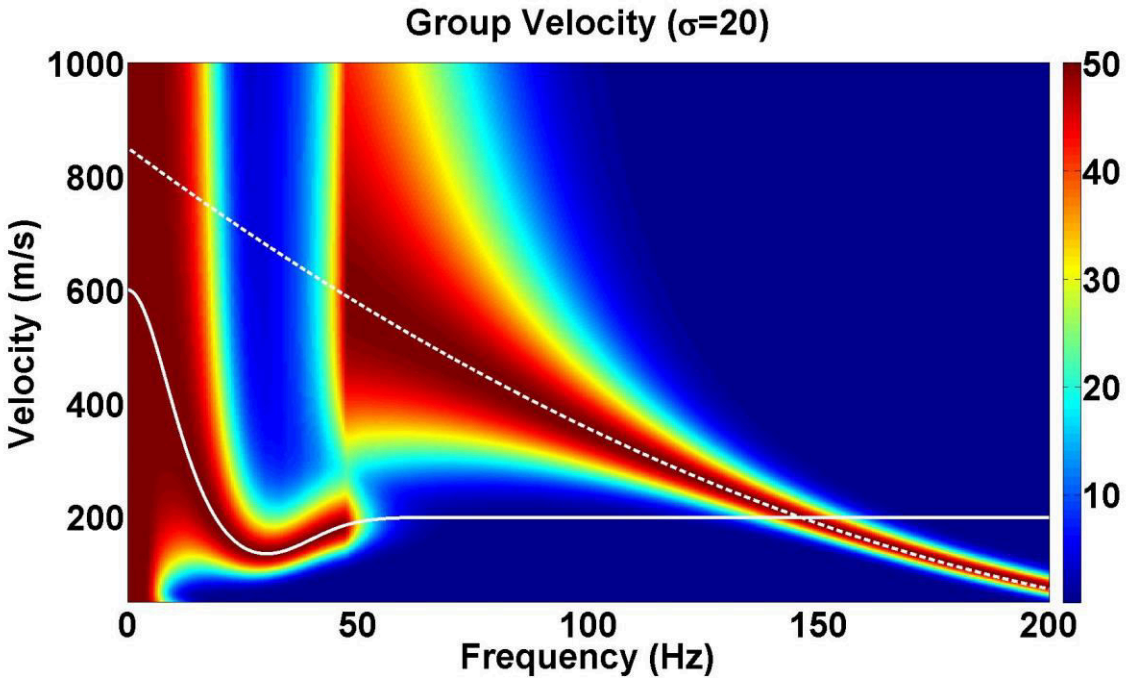

Figure 3.8 The estimated group velocity for the record in Figure 3.2 based on the scaling factor σ=20. The solid and dashed lines correspond to the theoretical values.

3.5 Real data

The real data were acquired in September 2011 by (Consortium for Research in Elastic Wave Exploration Seismology, University of Calgary) CREWES, near Hussar, Alberta, Canada. The survey was originally designed to test the use of different sources and receivers to investigate the extension of the seismic bandwidth in the low frequency range (Margave et al., 2011). 10 Hz geophones were spaced at 10 meter intervals along the line. A vibroseis source with a linear sweep from 1 Hz to 100 Hz, and listening time at 10 s was used.

Figure 3.9 shows a shot record containing multimodal ground roll. Since most ground roll energy is confined to the frequencies from 0 to 35 Hz (Figure 3.10) and with respect to our synthetic data results that a small scaling factor for low-frequency surface wave should be chosen, we choose a scaling factor of 2 to obtain the group velocity of the record. Figure 3.11 shows the group velocity obtained from the record using the slant stack generalized S transform based method. There are two distinct trends of the group velocity. The first trend contains frequencies of 3.5 Hz to 12 Hz and its velocity ranges from 130 m/s to 160 m/s, and the second trend contains frequencies from 9 Hz to 15 Hz with a velocity of around 200 m/s. The first trend can be referred to as the fundamental mode, and the second trend can be referred to as the first

higher mode. In order to verify the reliability of the group velocity of the real data, we calculate the phase velocity for the record and invert the fundamental mode phase velocity to an S-wave velocity model. We repeat the process for the group velocity as well to see whether two S-wave velocity models are in agreement with each other because the group velocity is linked to the phase velocity by

$$v_g(f) = v_p(f)^2/[v_p(f) - f v_p(f)'], \tag{3.3}$$

therefore we expect to obtain similar S-wave velocity models from the inversion of the phase and group velocities if the estimated group velocity in Figure 3.11 is reasonable enough.

Figure 3.12 shows the phase velocity obtained from the phase shift method (Appendix C, Park et al., 1998). Similar to the group velocity, two trends of the phase velocity are observable on the phase velocity image. The first trend ranges from frequencies of 3.5 Hz to 12 Hz while its velocity ranges from 400 m/s to 200 m/s, and the second trend ranges from 9 Hz to 15 Hz while its velocity ranges from 400 m/s to 300 m/s respectively. Again, we can regard the first trend as the fundamental mode and the second trend as the first higher mode. The estimated group velocity is less than the phase velocity which is well accordant with other observations (e.g. Kulesh et al., 2005; Holschneider et al., 2005; Askari and Ferguson, 2012).

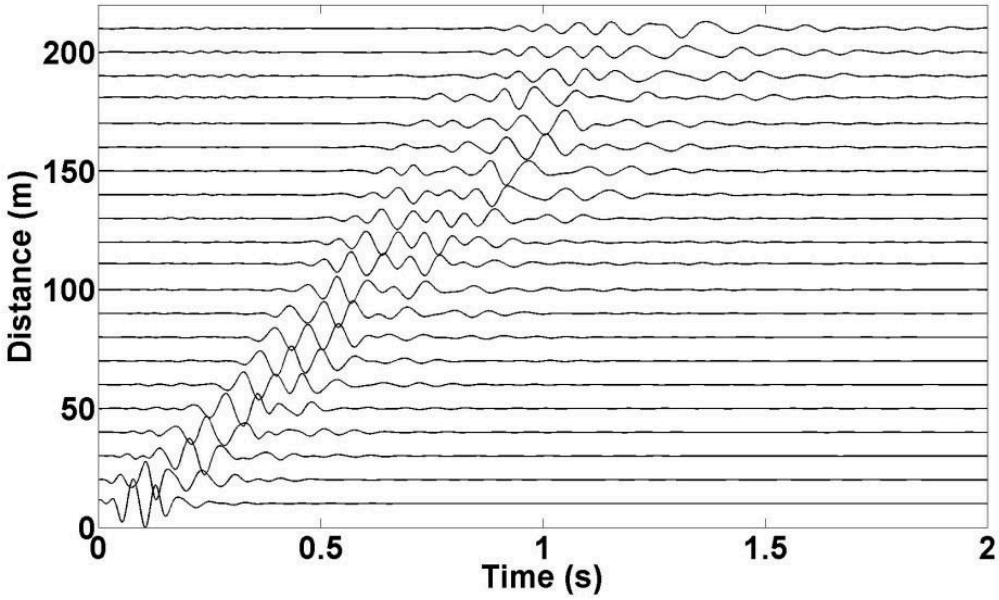

Figure 3.9 Real data used in this chapter.

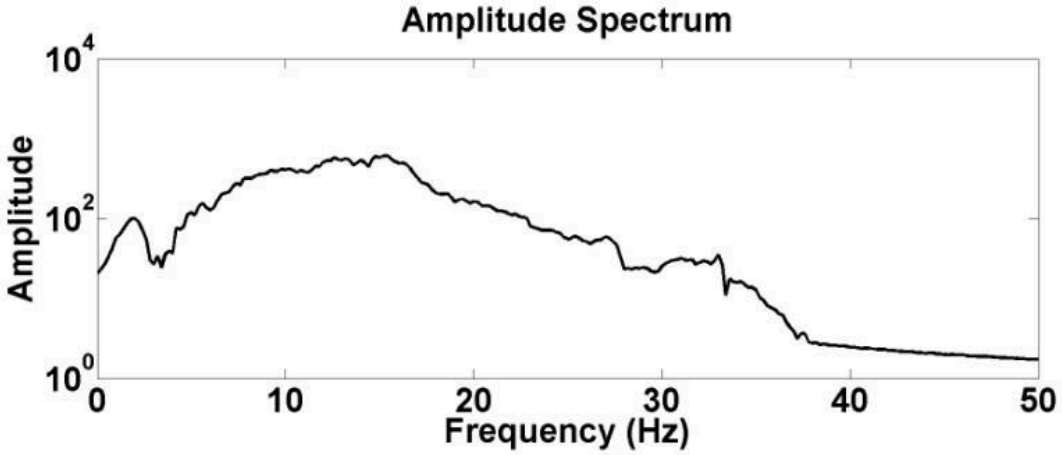

Figure 3.10 The average amplitude spectrum of the record in Figure 3.9.

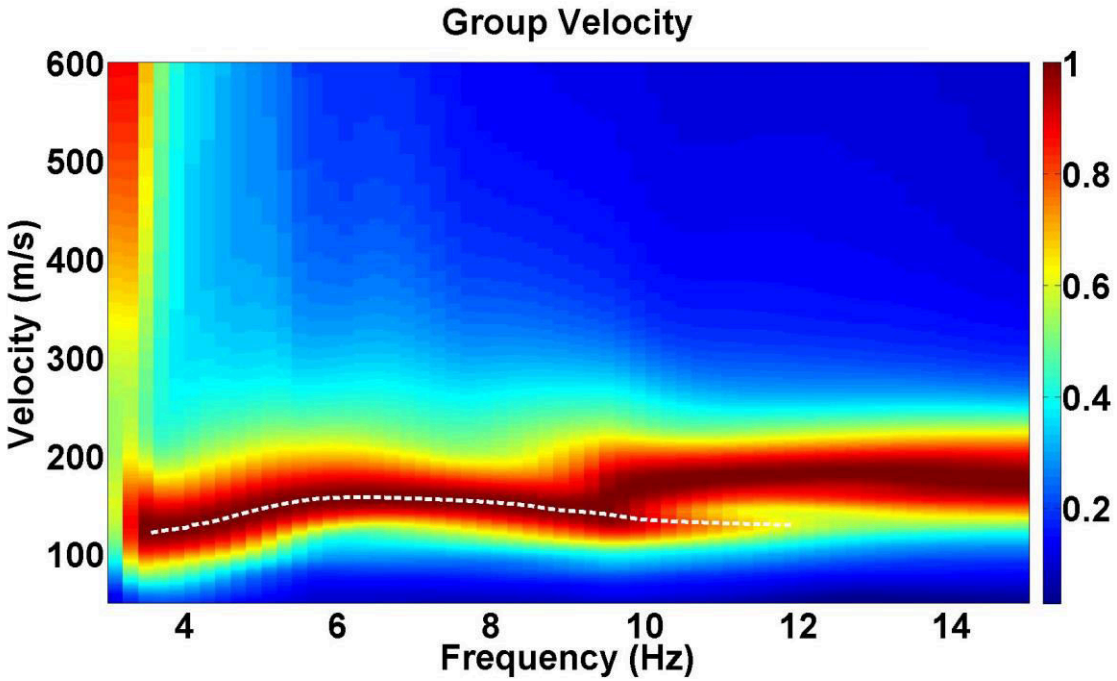

Figure 3.11 The estimated group velocity for the record in 3.9 based on the scaling factor σ=2. The fundamental mode of the group velocity is picked (the dashed line) for the inversion.

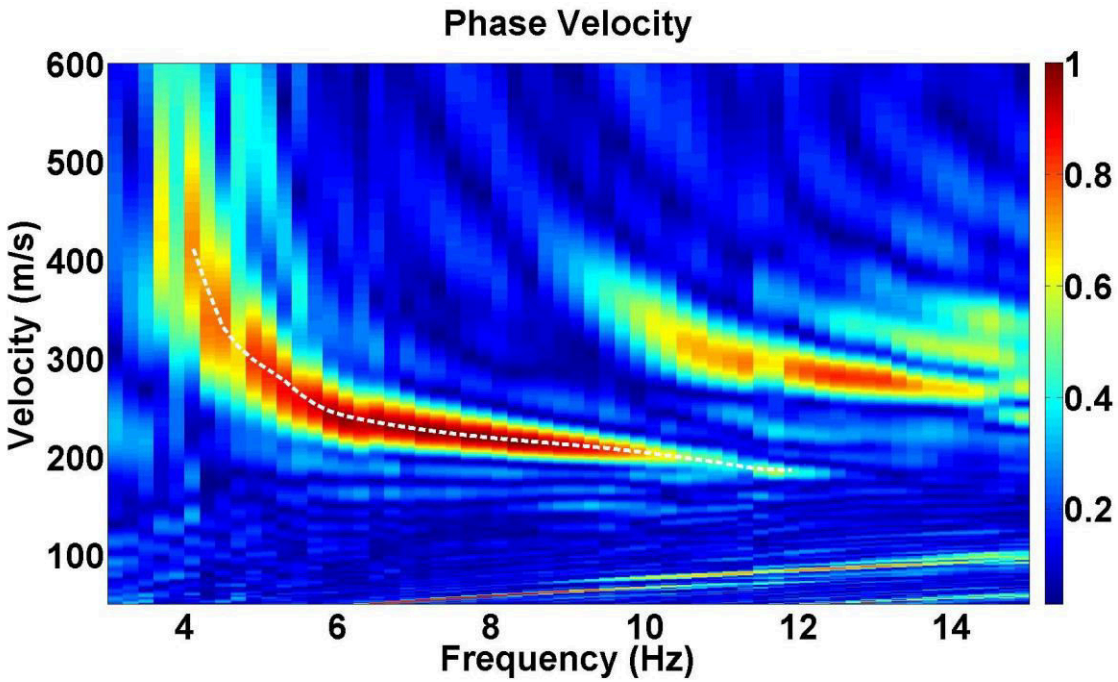

Figure 3.12 The estimated phase velocity for the record in Figure 3.9. The fundamental mode of the phase velocity is picked (the dashed line) for the inversion.

We try to obtain an S-wave velocity model based on the phase and group velocities of the fundamental mode using an inverse procedure. As mentioned in Chapter 1, we can forward model dispersion curves (either phase or group velocities) for any geological 1D model using Knopoff's method (Schwab and Knopoff, 1972). Using equation 1.3, we optimize an initial model using the Conjugate Gradient method (Appendix B, Zeidouni, 2011). The initial model is calculated from the phase velocity using the formula derived in Xia et al. (1999)

$$V_s(z) = 1.09 v_p(f), \tag{3.4}$$

where v_p denotes the phase velocity, V_s denotes the S-wave velocity, f denotes frequency, and z denotes depth which is determined by

$$z = 0.5[\frac{v_p(f)}{f}]. \tag{3.5}$$

We assume the subsurface to be composed of layers with constant thicknesses of 4 m. Since the maximum wavelength is 90 m, the maximum depth of investigation is assumed to be about 45 m (the half of the maximum wavelength (Xia et al., 1999)). Equation 1.3 is not very sensitive to the density and P-wave velocity (Askari et al., 2012). Therefore, we can assign some reasonable values of the density and P-wave velocity in the inversion and accomplish the inverse procedure based on the S-wave velocity only. The density is assumed to be 2200 kg/m^3 for all the layers.

We can obtain an estimate of P-wave velocity in our inversion from the S-wave velocity as a function of the Poisson ratio

$$V_p = V_s\left(\frac{1-\gamma}{0.5-\gamma}\right)^{\frac{1}{2}}. \tag{3.6}$$

Here γ denotes the Poisson ratio. Although the Poisson ratio is not constant for the near surface, we can assign a constant value for the Poisson ratio in equation 3.6 to be implemented in equation 1.3 because equation 1.3 is not very sensitive to the variation of P-wave velocity and an estimate of P-wave velocity is enough. We assume the Poisson ratio to be 0.45 which is commonly observed for the near surface (e.g. Ivanov et al., 2000). Using the above parameters, we optimize the model based on the inversion of the phase velocity and the group velocity. Figure 3.13 shows the observed (solid lines) phase and group velocities, and the predicted phase and group velocities (dashed lines) through the inversion. Figure 3.14 shows two S-wave velocity models obtained from the phase and group velocities. Two models are very similar to each other and exhibit the same trend and approximate values of the S-wave velocity versus depth. Similarity of the two models implies that the group velocity is well estimated. This demonstrates the capability of the slant stack generalized S transform based method for the estimation for the group velocity.

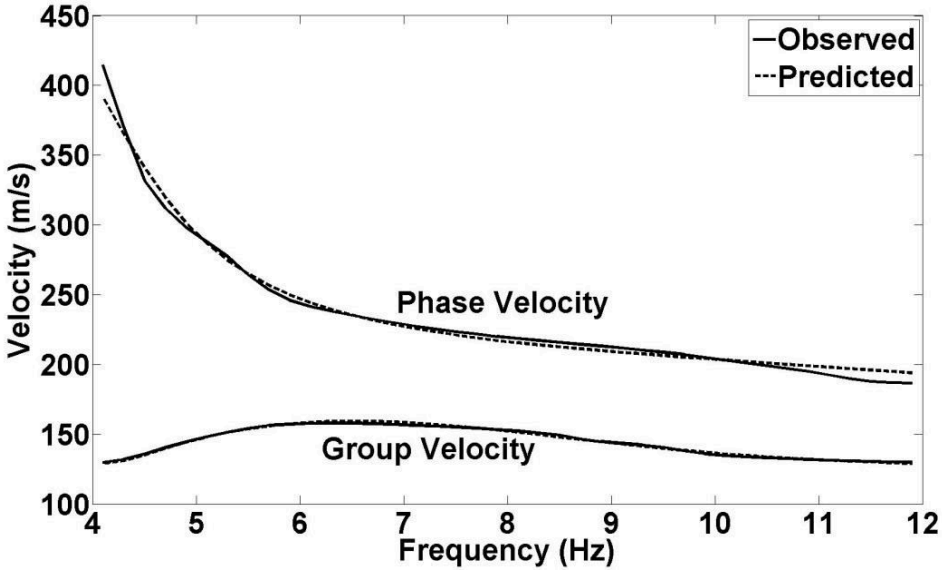

Figure 3.13 The observed and predicted phase and group velocities.

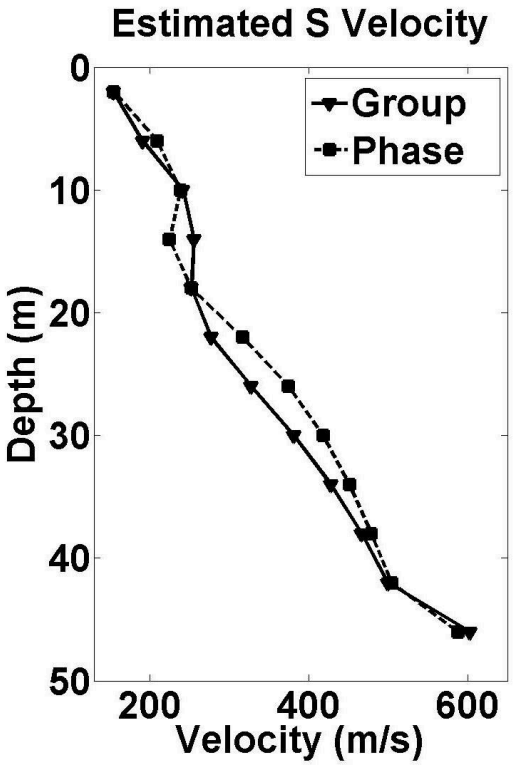

Figure 3.14 The estimated S-wave velocities for the record in Figure 3.9 based on the inversion of the group and phase velocities.

3.6 Discussion

Several studies confirm that the joint inversion of the phase velocities of the fundamental modes with higher modes results in better vertical resolution (e.g. Feng et al., 1995; Luo et al., 2007). However, in practice, the joint inversion of the phase velocities of the fundamental modes with higher modes can be challenging because it is very hard to pick different modes in the presence of large velocity contrasts and/or hidden layers (O'Neill and Matsuoka, 2005). One of objectives of this study was to develop a method to estimate the group velocity of multi-modal surface wave to test whether the joint inversion of the *phase* and *group* velocities of the *fundamental* mode can provide a better vertical resolution. Luo et al. (2011) present sensitivity analyses of the phase and group velocities by implementing different models. They show the group velocity possesses a higher sensitivity and wider usable frequency ranges in comparison with the phase velocity. Although their analysis shows a potential of the group velocity to improve S-wave velocity estimation, their real data result of the group velocity does not exhibit a significant improvement in comparison with the phase velocity. They find that there is a less than 15% difference between S-wave velocities estimated from the group and phase velocities. Our

results of the group and phase velocity inversion are in a good agreement with theirs. Based on our results, we are not able to confirm whether the joint inversion of the phase and group velocities results in a better vertical resolution.

3.7 Conclusions

The slant stack generalized S transform uses a slant stack in the time-frequency domain on the generalized S transform. The method is robust to estimate group velocity where surface wave is multi-modal. The resolution of the group velocity is manipulated by a scaling factor. When we choose a small value of the scaling factor, we properly estimate the group velocity of the low frequency surface wave. However, at high frequencies, the group velocity might be overestimated. This is explained by the frequency uncertainty of the generalized S transform at higher frequencies which results in a low frequency resolution. In order to increase the frequency resolution, we should widen the window in the time domain. When the window becomes wide in the time domain, the time resolution will decrease at low frequencies which consequently results in a low velocity resolution of low frequency surface wave. Therefore, there is a tradeoff between the resolution of low and high frequency surface wave. It is concluded where surface wave has a broad range of frequencies, different scaling factors with respect to the frequency content of surface wave should be chosen.

Chapter Four: Estimation of Converted Waves Static Corrections Using CMP Cross-Correlation of Surface Waves

4.1 Overview

In order to compute receiver static corrections for converted waves successfully, we need an accurate shear wave velocity model of the near surface. To obtain a shear-wave velocity model, we have enlarged upon the idea of CMP Cross-Correlation of Surface Waves (CCSW). In our approach, we cross-correlate each trace of a shot record with a reference trace that is selected from within the shot gather based on high signal to noise ratio. This step removes the initial phase of a source. New midpoints that relate to the correlated traces are then calculated. We calculate the phase velocity for each CMP gather, and we convert the resulting dispersion curve to a vertical shear wave velocity through an inverse procedure (Conjugate Gradient (Appendix B) for example). Our approach is faster than the conventional CCSW because in the conventional CCSW all traces within a CMP gather are cross-correlated with each other which is computationally expensive.

In this chapter we show that, in order to have a precise estimation of a dispersion curve, we only consider those traces that lie in a spatial window and we found that the optimum window length (aperture) should be close (one to one and half times) to the maximum wavelength in a CMP gather. If the aperture is too short, we see a blurred image of dispersion curves and this causes modal interference. When the aperture is optimum, we see a high resolution image of each mode within the dispersion curve that avoids modal interferences. Therefore, not only does an appropriate aperture length improve dispersion curve estimation, but it also avoids the modal interference that can be so disastrous in surface waves studies (Strobbia et al., 2011).

We obtain 2D near surface shear wave velocity models for two real data sets. By decimating traces from the first dataset, we show that we can obtain a good trend of S-wave statics relatively similar to those obtained from the original dense array data. This demonstrates that CCSW has a capacity to address static correction of converted waves when geophone spacing is wide. Using the second data set, we show the importance of wavelength dependent aperture for estimating the phase velocity. We obtain static corrections based on an S-wave velocity model obtained from CCWS and successfully apply them to the data.

4.2 Introduction

Converted wave data acquisition, which provides more details about reservoirs, has been widely considering by industry in recent years. However, there are still many challenges that must be addressed. One of these is the S-wave receiver statics, which can be two to ten times greater than the P-wave receiver statics (Tatham and McCormack, 1991) due to the large V_p/V_s ratio in the near surface.

We can divide S-wave receiver static correction methods into two categories. One category is data-based methods, including the CRP stack-power optimization method (Cary and Eaton, 1993) and Monte-Carlo simulated annealing (Eaton et al. 1991). The CRP stack-power optimization method gives good results where geological structures are not complex, whereas Monte-Carlo simulated annealing gives a fairly good solution but is computationally expensive (Li et al., 2012).

Another category is based on modeling the shear wave velocity. These methods are based on either refracted waves analysis (Frasier and Winterstein, 1990) or surface wave analysis (Park et al., 1999a). Although refracted waves analysis is a conventional method for the estimation of P-wave statics where a near surface velocity model is estimated, the method is ambiguous for S-wave statics because S-wave refractions are hard to pick. Surface wave analysis is based on the inversion of the dispersion curve of ground roll, where the phase velocity as a function of frequency is inverted to an S-wave velocity model. The availability of ground roll as a predominant event in seismic data is utilized for the S-wave velocity estimation of the near surface.

Spectral Analysis of Surface Waves (SASW) (Nazarian et al., 1983) is a method to estimate S-wave velocity for the near surface. The method is based on the inversion of the fundamental mode phase velocity of ground roll. There are pairs of shots and geophones. The geophone interval is determined with regard to the frequency range of ground roll. For higher frequency components, narrower geophone spacing is designated whereas for lower frequency components, wider geophone spacing is employed. In order to have an improved signal to noise ratio, for any geophone spacing, there are two shots which are configured and reconfigured with respect to the midpoint of the geophones. Since the phase velocity and consequently the S-wave velocity are estimated with respect to a midpoint, the method provides good lateral resolution.

However, the method suffers from a low signal to noise ratio (because there are only two shots and receivers), and the effect of higher modes and other types of waves (P-waves for example).

Multi-channel Analysis of Surface Waves (MASW) (Park et al., 1999a) is another method based on the analysis of dispersed ground roll. There is a shot and an array of geophones where the phase velocity of the ground roll is determined by transforming (e.g. by the phase shift method (Appendix C, Park et al., 1998)) the data from the time-offset domain to the frequency-slowness (or velocity) domain. The estimated phase velocity and consequently the S-wave velocity are assigned to the point in the middle of the array. Generally speaking, a MASW survey is faster than an SASW survey in the terms of data acquisition and processing. MASW also provides a better signal to noise ratio and is less affected by ambient noise since several geophones are utilized in the processing (Hayashi and Suzuki, 2004). Therefore, MASW results in better dispersion curve estimates, but at the cost of lateral resolution because the phase velocity and the S-wave velocity are not determined with respect to a midpoint between shots and receives (Hayashi and Suzuki, 2004). In order to improve the lateral resolution in a MASW survey, smaller arrays should be used, but this reduces the resolution of the dispersion curve (Park et al., 1999b). Therefore, there is a tradeoff between the estimation of the dispersion curve and lateral resolution in MASW surveys. In practice, it is critical to compensate for this tradeoff. Especially in converted wave surveys, rapid spatial velocity variations in the weathering layer need to be resolved in order to compute an appropriate velocity model for static corrections. This requires both excellent quality phase velocity information as well as high spatial resolution.

In this chapter, we have enlarged upon the idea of CMP Cross-Correlation of Surface Waves (CCSW Hayashi and Suzuki, 2004) to increase lateral resolution. In the Hayashi and Suzuki's methodology, all traces within a common mid-point (CMP) are correlated with each other, traces with the same offset which belong the same CMP are stacked, and a dispersion curve is computed. Though this method provides good lateral resolution and a dispersion curve simultaneously, the process is computationally expensive. Therefore in our approach, to reduce cost, we cross-correlate each trace of a shot record with a reference trace selected from within the shot gather based on high signal to noise ratio. This step removes the initial phase of a source. New midpoints that relate to the correlated traces are then calculated. We calculate the phase velocity for each CMP gather, and finally the dispersion curve is converted to a vertical shear wave velocity by an inverse procedure. By putting together all the vertical shear wave

velocity profiles of all the CMP gathers, a 2D image of shear wave velocity is obtained for the data set. Since in our approach only a reference trace is cross-correlated with other trace within a CMP gather, it is faster than the conventional CCSW where all traces within a CMP gather are cross-correlated with each other which is computationally expensive.

In this chapter we use two data sets. The first data set was acquired by CREWES (Consortium for Research in Elastic Wave Exploration Seismology, University of Calgary) from a site near Priddis, Alberta, about 30 km southwest of the city of Calgary. The site of the survey is located at the eastern edge of the Rocky Mountain foothills. We show that in order to have a precise estimation of dispersion curve, the maximum relative offset, which we call the aperture length in this study, must be close to the maximum wavelength of ground roll. If the aperture is too short, we see a blurred image of dispersion curves which causes modal interference. When the aperture is optimum, we see a high resolution image of dispersion curves that avoids modal interferences. Therefore, not only does an appropriate aperture length improve dispersion curve estimation, but it also avoids the modal interference that can be so disastrous in surface waves studies (Strobbia et al., 2011). By decimating the data, we show that we can obtain a good trend of S statics similar to the original data. This demonstrates that CCSW has a capacity to address static correction of converted waves when geophone spacing is wide. The second dataset was acquired in September 2011 by CREWES, near Hussar, Alberta, Canada. We show the importance of wavelength dependent aperture for estimating the phase velocity where there are wide ranges of wavelengths. We obtain static corrections based on an S-wave velocity model obtained from CCWS and successfully apply them to the data. We compare our static corrections result with another static corrections result obtained from PP refraction analysis scaled by 2.5 (assuming V_p/V_s ratio to be 2.5 for the near surface), and we find significant improvement of reflector coherence in the shot domain. Using our method, subsequent NMO velocity analysis shows that we obtain a better estimation of NMO velocity after applying calculated static corrections to the data.

4.3 Theory

As discussed in Chapter 2, if we assume that a geometrical spreading correction has been applied to surface wave data, and $h_1(\tau)$ is the recorded signal at station 1, then the Fourier spectrum $H_2(f)$ of the signal $h_2(\tau)$ recorded at station 2 can be expressed in terms of the Fourier spectrum $H_1(f)$ of $h_1(\tau)$ by equation 2.7. Therefore, for any station such as station 3 we

can write its Fourier spectrum (H_3) in terms of the Fourier spectrum of station 1 (H_1). For any frequency, the spatial wavenumber between h_3 and h_2 can be obtained by

$$k(f) = -\frac{\varphi_3(f)-\varphi_2(f)}{2\pi\Delta x_{2,3}} = -\frac{\Delta\varphi(f)}{2\pi\Delta x_{2,3}}, \quad (4.1)$$

where φ_2 and φ_3 are the absolute phase spectra of stations 2 and 3 respectively and $\Delta x_{2,3}=x_3-x_2$ is the distance between the two stations.

If we cross-correlate h_1 with h_2, the result is expressed in the Fourier domain as

$$C(H_1(f), H_2(f)) = e^{-\lambda(f)\Delta x_{1,2}} e^{-j2\pi k(f)\Delta x_{1,2}} H_1(f) H_1^*(f), \quad (4.2)$$

where H_1^* is the complex conjugate of H_1 and $\Delta x_{1,2}=x_2-x_1$ is the distance between the two stations. Similarly, we can write the Fourier spectra of the cross-correlated traces of h_1 and h_3 in the terms of the Fourier spectrum of h_1 (H_1) and the relative distance between h_1 and h_3 ($x_{1,3}=x_3-x_1$). With respect to the Fourier spectrum of the cross-correlated traces, the spatial wavenumber between stations 2 and 3 can be also estimated by

$$k(f) = -\frac{\emptyset_3(f)-\emptyset_2(f)}{2\pi\Delta x_{2,3}} = -\frac{\Delta\emptyset(f)}{2\pi\Delta x_{2,3}}, \quad (4.3)$$

where $\emptyset_2$ and $\emptyset_3$ are the absolute phase spectra of the cross-correlated traces of stations 1 and 2 and stations 1 and 3 respectively. Following calculation of the wavenumber 'k', the phase velocity is obtained by equation 2.12.

We use the approach expressed in equations 4.2 and 4.3 for the calculation of the phase velocity because the source effect (initial phase value) is removed and the data can be sorted into CMP gathers. Consequently, we calculate the phase velocity of traces in one CMP combined from different shots to localize our analysis spatially. In this study we use the phase shift method (Appendix C, Park et al. 1998) for the calculation of the phase velocity. The method is based on the estimation of the phase differences (shifts) of different traces for a range of frequencies and is able to estimate the phase velocity of multi-modal ground-roll (Appendix C).

4.4 CMP Cross-Correlation of Surface Waves

Hayashi and Suzuki (2004) introduce the idea of CMP Cross-Correlation of Surface Waves (CCSW) to increase lateral resolution. They correlate all traces within a common mid-point (CMP) with each other, traces with the same offset which belong the same CMP are stacked, and a dispersion curve is computed. This approach improves the lateral resolution while keeping a good resolution of dispersion curve imaging. Since a dispersion curve is measured with respect to a fixed mid-point, the method is similar to SASW, which gives good lateral resolution. The

dispersion curve is estimated by transforming multi-channel cross-correlated traces into the frequency-slowness (velocity) domain, which is similar to the idea presented in a MASW survey. Therefore the method takes the advantages of the two conventional methods for surface wave analysis. Though this method provides good lateral resolution and a dispersion curve simultaneously, the process is computationally expensive. Therefore in our approach, to reduce cost, we cross-correlate each trace of a shot record with a reference trace selected from within the shot gather based on high signal to noise ratio. This step removes the initial phase of a source. New midpoints that relate to the correlated traces are then calculated. We calculate the phase velocity for each CMP gather, and finally the dispersion curve is converted to a vertical shear wave velocity by an inverse procedure. By putting together all the vertical shear wave velocity profiles of all the CMP gathers, a 2D image of shear wave velocity is obtained for the data set.

4.5 Field Data

We have used two converted-wave data sets in this study. The first data were acquired from a site near Priddis, Alberta, about 30 km southwest of the city of Calgary. The site of the survey is located at the eastern edge of the Rocky Mountain foothills. The 3C geophones are spaced at 2 m and the time sample interval is 1 ms. Vibroseis sources are spaced at 4 m, with a linear sweep from 10 Hz to 120 Hz, and a listening time of 10 s. Using this dense data set we explain the concept of aperture length, which plays an important role in successfully imaging dispersed cures for the estimation of the phase velocity. The dense geophone array in the Priddis data allows us to investigate effect of geophone interval on the shear wave velocity estimation and PS statics. By decimating the data we show how shear wave velocity and PS statics are affected by changing geophone interval.

The second data set was acquired in September 2011 by (Consortium for Research in Elastic Wave Exploration Seismology, University of Calgary) CREWES, near Hussar, Alberta, Canada. The survey was originally designed to test the use of different sources and receivers to investigate the extension of the seismic bandwidth in the low frequency range (Margave et al. 2011). 10 Hz geophones were spaced at 10 meter intervals along the line. A vibroseis source with a linear sweep from 1 Hz to 100 Hz, and listening time at 10 s was used. We show the importance of wavelength dependent aperture length for estimating the phase velocity for this data set. We successfully apply the calculated statics to the PS data.

4.6 Aperture Length (Priddis data)

We select the reference trace for each shot gather at an offset of 30 m where the signal to noise ratio is high and wave propagation is planar (avoiding near offset effect) (Xia et al, 1999). The data are binned using a CMP bin size of 5 m to increase fold to allow for a more stable phase velocity analysis. Figure 4.1 shows traces in a bin where the maximum offset is 69 m and the maximum wavelength is about 40m. The maximum wavelength is calculated by analyzing the CMP gather with different maximum offsets. Figure 4.2 shows the phase velocity that is calculated for the data in Figure 4.1. We use the phase shift method (Appendix C, Park et al., 1998) in this chapter to calculate the phase velocity. The maximum observed wavelength in this record is 40 m. There are three distinct patches of dispersion curves, which are indicated by letters ‘a’, ‘b’ and ‘c’. The first approach for the estimation of a phase velocity is to choose patches ‘a’ and ‘b’ as parts of the main patch of the dispersion curve because of their good apparent coherency. Applying this approach, we will pick the solid line in Figure 4.2 as the fundamental mode of the dispersion curve and consider patch ‘c’ as an artifact. An alternative approach is to choose patches ‘a’ and ‘c’ as parts of the main patch of the dispersion curve. In this case, the dashed line in Figure 4.2 is the fundamental mode of the dispersion curve and patch ‘b’ is considered as the first higher mode of ground roll. Though the second approach seems to be more realistic, the apparent incoherency of patches ‘a’ and ‘c’ might make us hesitant to choose it. In order to evaluate both approaches, we shorten the maximum relative offset to 45 m, which is close to the maximum length of the observed wavelength in the data (40 m) and calculate the dispersion curve. Figure 4.3 shows the phase velocity. Here we see two distinct patches ‘a’ and ‘b’, where patch ‘a’ is the dispersion curve (the solid line) pertinent to the fundamental mode with a tangible coherency and patch ‘b’ is the dispersion curve (the dashed line) related to the first higher mode. It can be concluded from Figure 4.3 that choosing the optimum length of the window (Figure 4.4) for trace selection plays an important role in CCSW analysis. We call the window length ‘*aperture length*’ in this study. It facilitates the estimation of the dispersion curves (the fundamental mode and higher modes) while maintaining good lateral resolution.

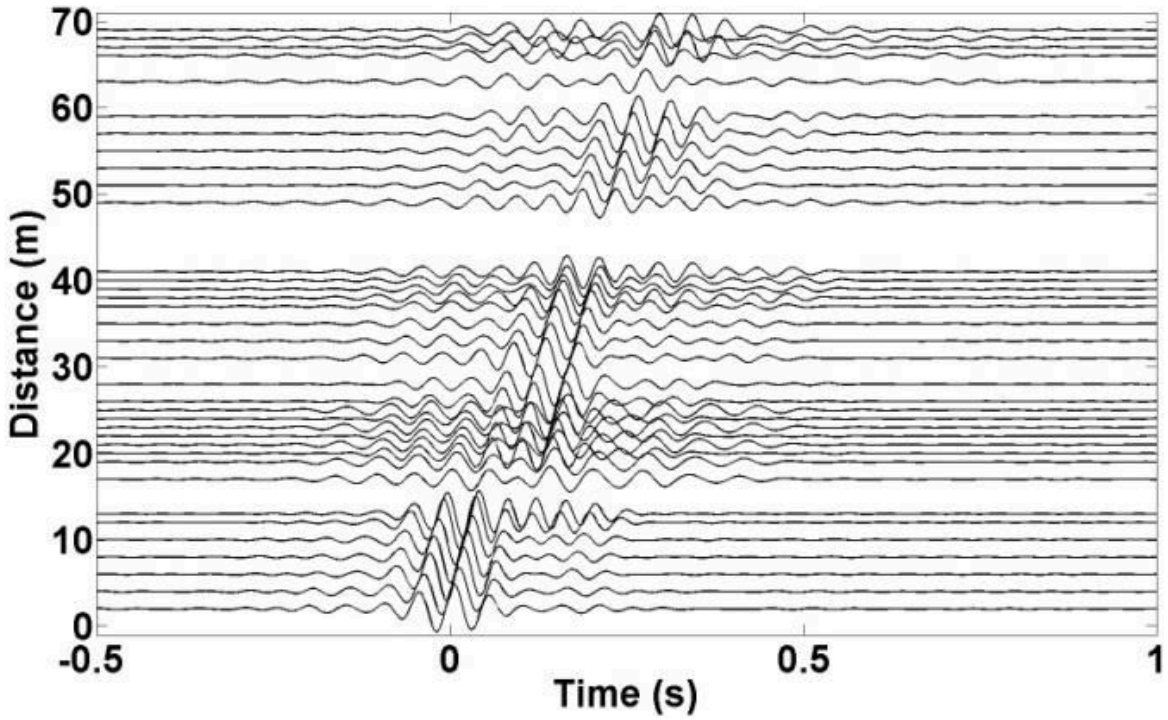

Figure 4.1 Traces in a bin.

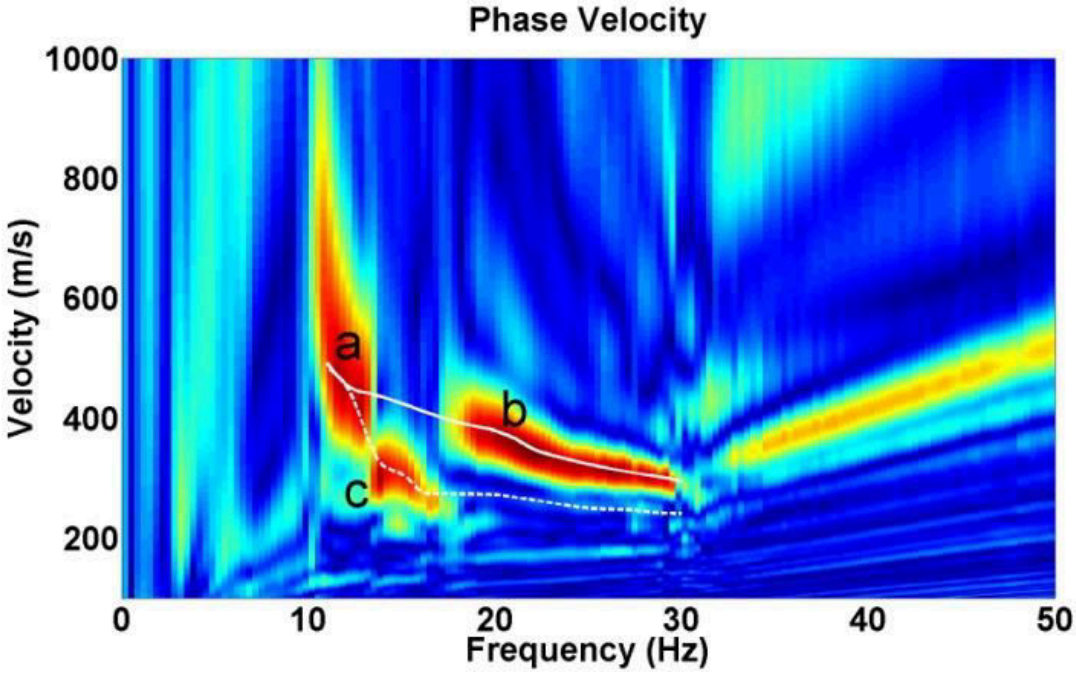

Figure 4.2 The phase velocity for the record in Figure 1.

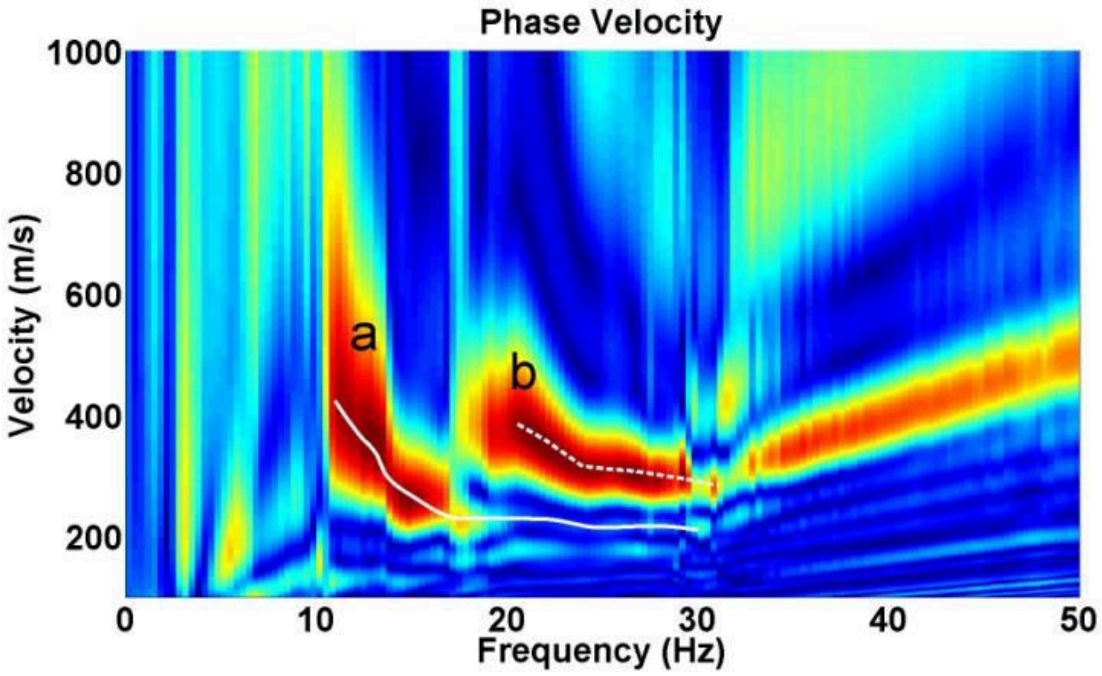

Figure 4.3 The phase velocity for the record in Figure 1 with aperture length 45 m. The solid line is the fundamental mode and the dashed line is the first higher mode.

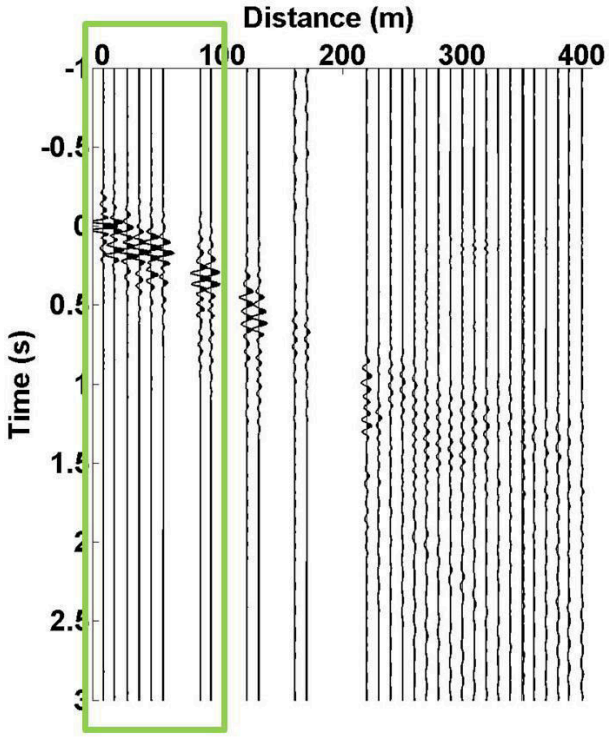

Figure 4.4 Concept of Aperture. When aperture length is 100 m, only those traces whose relative offsets are less than 100 m are considered for processing.

Figure 4.5 shows how dispersion curves evolve with respect to the aperture length. The aperture length increases from 4 m to 70 m in steps of 6 m. In the beginning, where the aperture is smaller than 20 m, a single crooked dispersion cure is observable (Figures 4.5a-c). Because the aperture length is not long enough with respect to the wavelength ranges, two modes (the fundamental and first higher) are superimposed. When the aperture length increases from 22 m to 34 m, we observe two modes more obviously (Figures 4.5d-f). This shows that dispersion curve image resolution improves with aperture increment. A good distinct image of two dispersion curves is observable in Figure 4.5g, where the aperture length is 40 m. Here the aperture length is equal to the maximum wavelength. High resolution images of dispersion curve are observed in Figures 4.5h-j, where the aperture lengths are 46 m, 52 m and 58 m. Dispersion curve resolution of the fundamental mode decreases when the aperture length increases from 64 m to 70 m (Figures 4.5k-l). This can be explained by near surface lateral heterogeneity. When the aperture length is long with respect to the maximum wavelength, the near surface lateral heterogeneity causes wide ranges of phase velocity for each mode at each frequency. Therefore, dispersion curve coherency becomes weak. Based on our empirical observations obtained from the analyses of different CMP gathers of the data set, an optimum aperture length is given by

$$\Gamma = \zeta \Lambda, \tag{4.4}$$

where Λ is the maximum wavelength and ζ is

$$1 \leq \zeta \leq 1.5. \tag{4.5}$$

The maximum wavelength 'Λ' is determined by

$$\Lambda = \frac{v_p(f)_{max}}{f}, \tag{4.6}$$

where $v_p(f)_{max}$ is the maximum phase velocity of the fundamental mode. Our finding is in good agreement with a study by Ikeda et al. (2013), who propose the same criteria for an appropriate aperture length by analyzing synthetic and real data.

4.7 S-wave Velocity Model for the Priddis Data

We estimate the fundamental mode phase velocity for all the CDP bins in the line (Figure 4.6). We invert the phase velocity to a shear wave velocity model by applying an inverse scheme described in Chapter 1. For the data inversion, we assign a density of 2300 kg/m^3, based on well logs from the study area. We use the approach used in Chapter 3 to assign an estimation of P-wave velocity based on the S-wave velocity and the Poisson ratio (equation 3.6). Here, we again assume the Poisson ratio to be 0.45 which is commonly observed for the near surface (e.g.

Ivanov et al. 2000). Using equation 1.3, we try to optimize a model using the Conjugate Gradient method (Appendix B, Zeidouni, 2011). The initial model is calculated from the phase velocity using equations 3.3 and 3.4. We assume the subsurface to be composed of layers with constant thicknesses of 2m. Since the average of the maximum wavelengths is about 40m, the maximum depth of investigation is assumed to be about 20m (the half of the maximum wavelength (Xia et al., 1999)).

Figure 4.7 shows the predicted phase velocity (the dashed line) versus the observed phase velocity of the fundamental mode in Figure 4.3 (the solid line) obtained from nine iterations using the Conjugate Gradient method (Appendix B). Figure 4.8 shows the S-wave velocity model obtained from the phase velocity in Figure 4.6. Some geological features at the depths 7.5 m and 15 m are noticeable. A low velocity zone in the middle of the line (the distance from 250 m to 325 m) is detectable which is surrounded by two high velocity zones. The velocity in the right side of the low velocity zone is higher than the left side. This detailed S-wave velocity model and geological features demonstrate the potential of CCSW for near surface shear wave velocity imaging. Figure 4.9 (solid line) shows the static corrections calculated from the S-wave velocity model in Figure 4.8. The static corrections in Figure 4.9 are the difference between static corrections at any CMP location and the average of the total static corrections. The detailed static corrections show the high potential usage of the method for the calculation of the static correction of converted waves in multi-component studies. A dramatic change of the calculated static corrections is observed around 175 m. The relative amount of the static corrections is about 20 ms which seems to be reasonable for first 20 m of the near surface. The reason that we are not able to image deeper layers in this study is frequency bandwidth limitation. The minimum frequency that we can observe in this data set is 11 Hz. This confines the depth of study. In practice, it is possible to increase the depth of study by using a low frequency source or doing the joint inversion of higher modes with the fundamental mode (Feng et al., 2005).

4.8 Geophone Spacing Interval

In order to investigate the role of spacing interval in the calculation of static corrections, we decimate the data to have 8 m geophone spacing instead of 2 m geophone spacing, which is closer to spacing interval in the real world. The decimated data are binned using a CMP bin size of 15 m to increase fold. The inversion parameters and procedure are the same used for the original data. Figure 4.10 shows the S-wave velocity model for the decimated data. The general

image of the decimated data is in a good agreement with the original data. However, some detailed velocity variations are missed in the decimated data. For instance, the decimated model proposes a lower S-wave velocity from 80 m to 140 m distance and also exhibits a smoother lateral velocity variation from 325 m to 400 m distance. This can be explained by the sampling interval effect. When we have a finer geophone spacing, we obtain a more detailed structure of the subsurface while a wider geophone spacing provides a general image of subsurface.

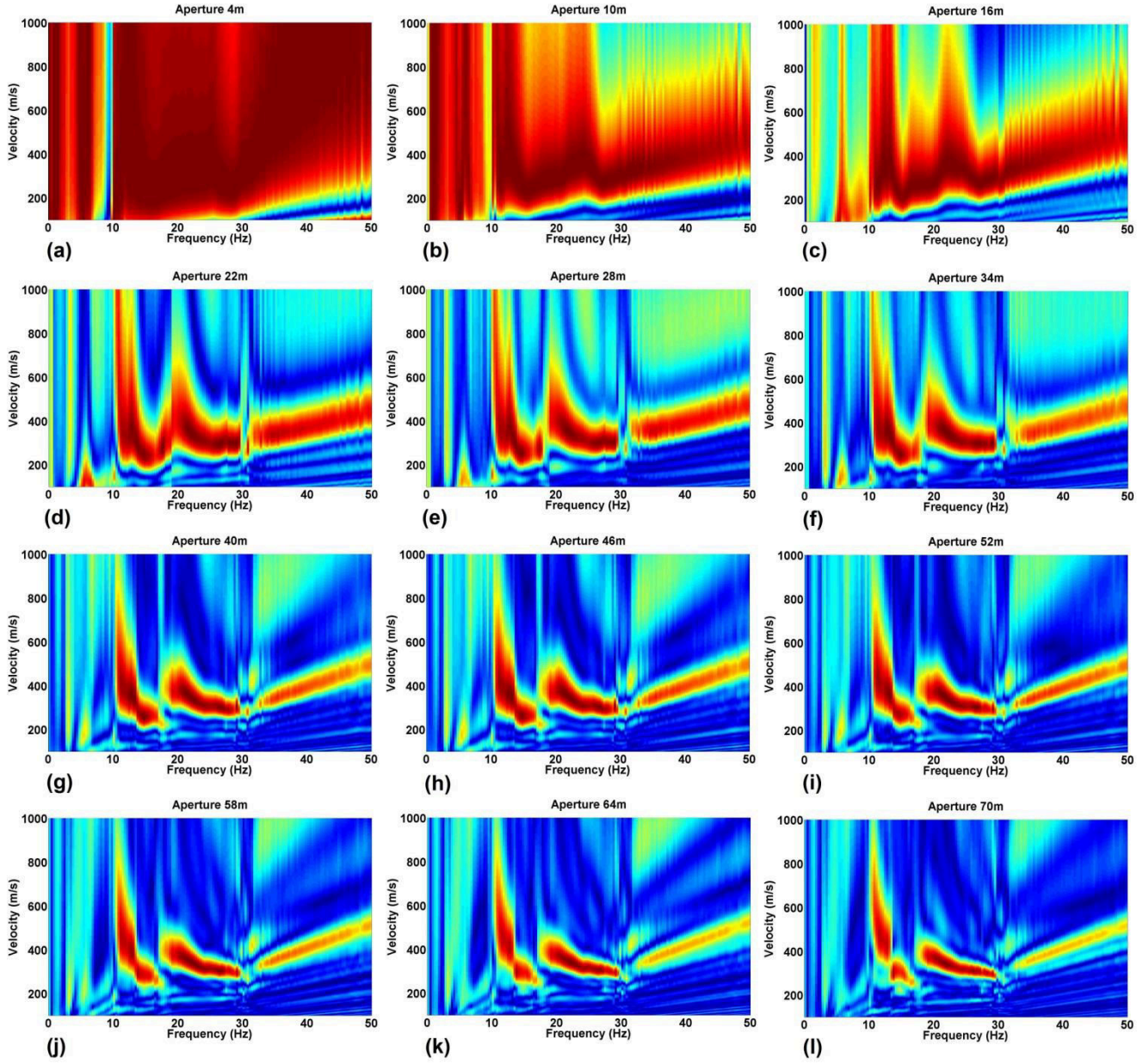

Figure 4.5 Evolution of dispersion curves. The aperture length increases from 4 m (a) to 70 m (l) in steps of 6 m.

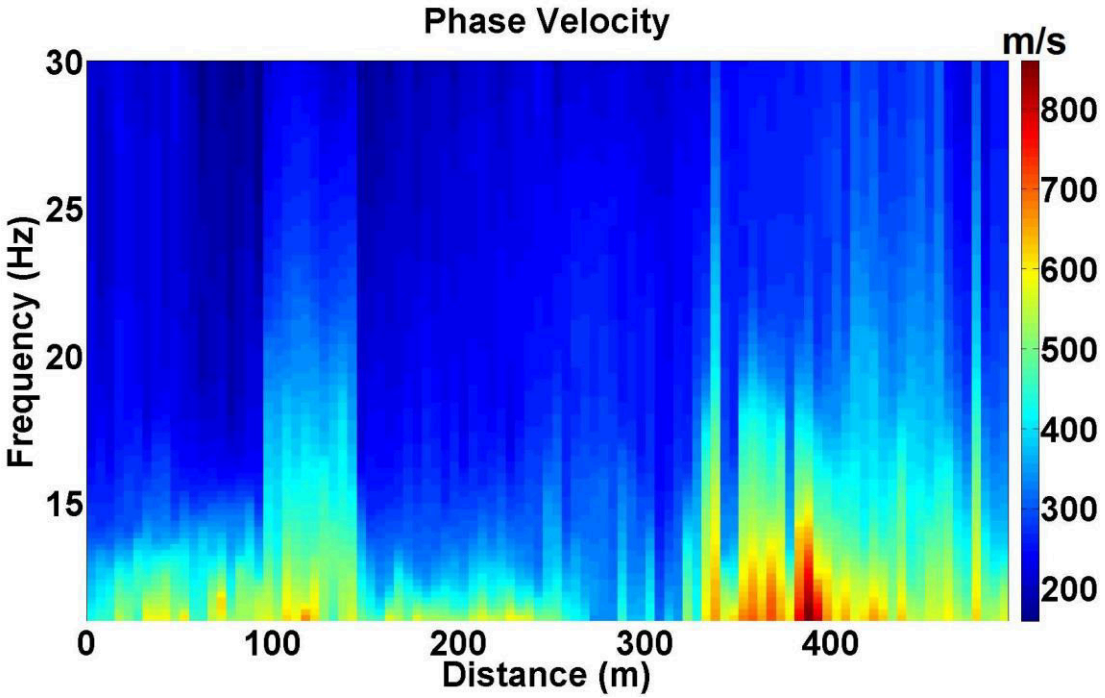

Figure 4.6 The estimated phase velocity for the Priddis data.

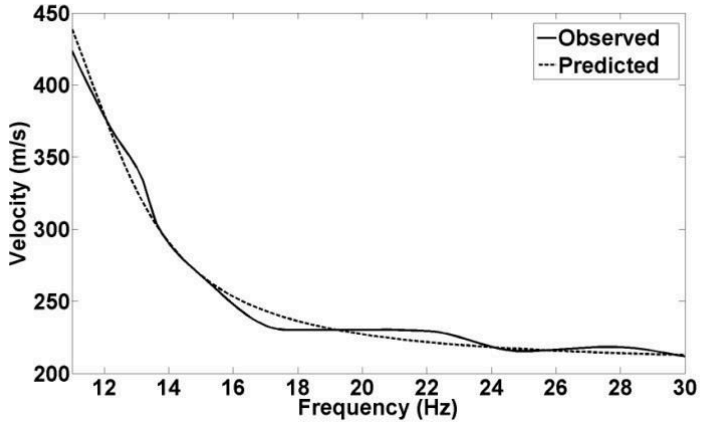

Figure 4.7 The predicted phase velocity (the dashed line) versus the observed phase velocity in Figure 3 (the solid line).

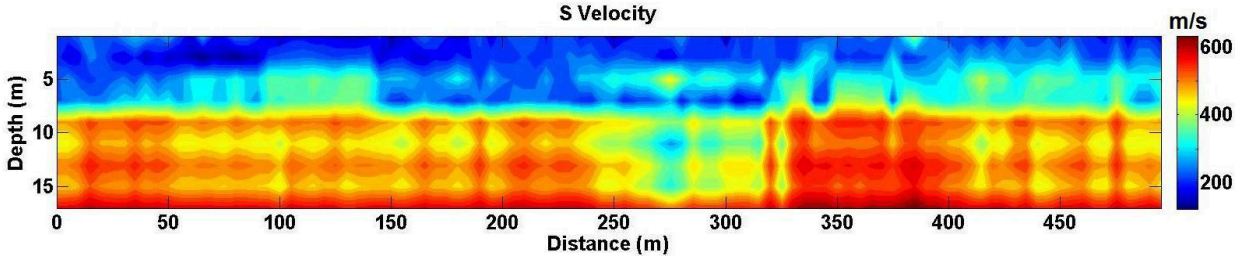

Figure 4.8 The S-wave velocity model for the Priddis data obtained from the phase velocity in Figure 4.6.

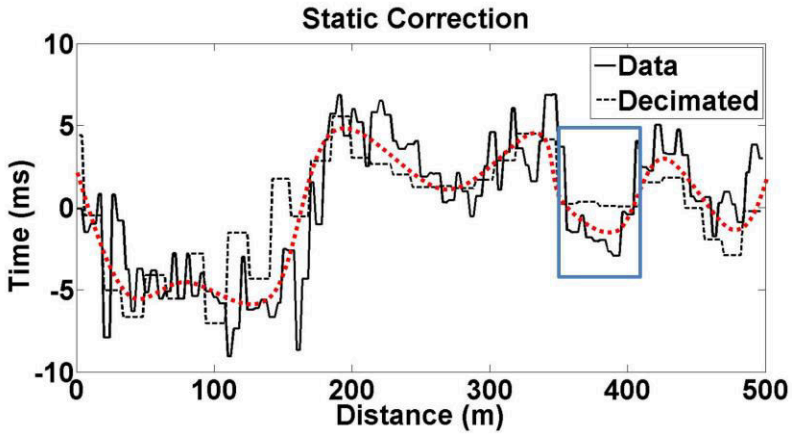

Figure 4.9 Static corrections for the Priddis data (the solid line) and the decimated data (the dashed line).

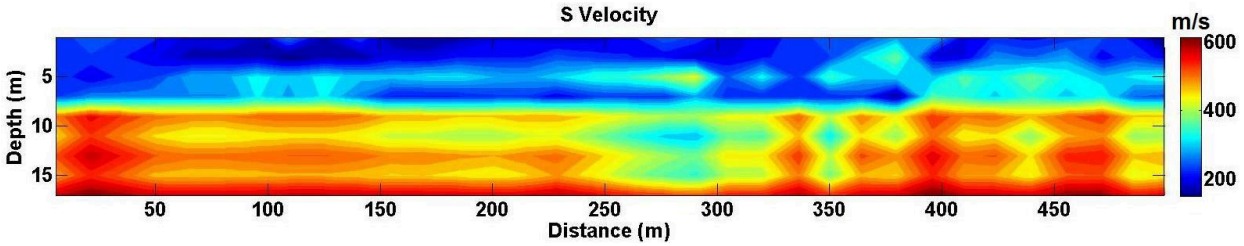

Figure 4.10 The S-wave velocity model for the decimated data.

Based on the S-wave velocity model in Figure 4.10, we calculate PS statics. PS static for the decimated data is indicated by the dashed line in Figure 4.9. Generally, the decimated data provides slightly smaller calculated statics in comparison with the original data. The calculated statics for the distance from 330 m to 420 m (the blue box in Figure 4.9) are larger than those for the original data because there is a high velocity anomaly surrounded by a low velocity field in these geophone locations. When geophone sampling is wider, this high velocity abnormality cannot be detected. Thus, the decimated data proposes smoother statics. Though the decimated data statics and the original data statics are slightly different in details, both data relatively exhibit the same general trend for the PS statics (the red dotted line). This demonstrates CCSW has a potential to address converted waves static corrections where geophone interval is wide. Unfortunately, the Priddis data do not contain strong PS events to evaluate the calculated statics. Therefore, we analyzed the Hussar data where the data contain strong converted waves.

4.9 PS Static Corrections (Hussar Data)

We estimate an S-wave velocity model for the Hussar data in order to calculate receiver static corrections. The procedure of sorting the data from shot gathers into cross correlated CMP gathers is similar to that done for the Priddis data, however the offsets of the reference traces are about 10 m. In this data set, a wide range of wavelengths is observable. Therefore, we use a wavelength-dependent aperture for these data. Figure 4.11a shows a phase velocity image for a CMP gather whose maximum wavelength is about 150 m. The aperture length is 80 m. At low frequencies (4 Hz to 8 Hz), where the wavelengths are large, it is very hard to pick the phase velocity due to the low resolution of dispersion curves. This is explained by unsuitable aperture length because it is much smaller than the wavelengths at these frequencies. However, at higher frequencies (10 Hz to 15 Hz), where the wavelengths are in the order of 20 m, we can see a better trend of the dispersion curve and therefore the phase velocity is easily detectable. Figure 4.11b shows the estimated phase velocity for the same CMP gather where the aperture length is 200 m. The phase velocity is obvious on the high resolution images of dispersion curves because, as discussed earlier, the aperture length is close to the maximum wavelength. Figure 4.11c shows dispersion curves for another CMP gather whose maximum offset is about 70 m. The aperture length is 80 m. Clear images of dispersion curves are noticeable for all frequencies from 4 Hz to 15 Hz because of the suitable length of the aperture. The aperture length (80 m) is close to the maximum wavelength (70 m).

We obtain a 2D image of the phase velocity based on an aperture wavelength dependent analysis of the CMP gathers. Figure 4.12 shows the 2D phase velocity image for the Hussar data. A low phase velocity zone from 2000 m to 2500 m distance is noticeable, which can be inferred to be a channel. Another low phase velocity is observed from 3500 m to 4200 m distance. Two smaller low phase velocity zones can be seen from 800 m to 1200 m and from 1500 m to 1700 m distance. Based on the inverse procedure as explained for the Priddis data, we obtain a 2D image of the S-wave velocity for the Hussar data. Based on well log data we assume the density to be 2200 kg/m^3. P-wave velocity is estimated using equation 3.6 and assuming the Poisson ratio to be 0.45. We assume the subsurface to be composed of layers with constant thicknesses of 4 m. Since the average of the maximum wavelength is 90 m, the maximum depth of investigation is assumed to be about 45 m (the half of the maximum wavelength (Xia et al. 1999)). Figure 4.13 shows the estimated S-wave velocity model for the Hussar data. Two interpreted major channels

are seen from 2000 m to 2500 m and from 3500 m to 4200 m distances, which correspond to the two major low phase velocity zones in Figure 4.12. Two smaller channels are observable from 800 m to 1200 m and from 1500 m to 1700 m distances, which correspond to low phase velocity zones in Figure 4.12. The S-wave velocity fluctuates with distance. This is expected in the near surface where the weathered layer causes dramatic velocity variations. We calculate static correction from the S-wave velocity model. The black solid line in Figure 4.14 indicates the static corrections for the Hussar data, which vary from -40 ms to 50 ms. The static corrections in Figure 4.14 are calculated from the difference between static corrections at any CMP location and the average of the total static corrections. The largest static corrections, which are about 50 ms, are seen from 2000 m to 2500 m distance, corresponding to one of the major channels interpreted in Figure 4.13. We apply the static correction to the Hussar data to assess the validity of the calculated statics.

Figure 4.15a shows the stacked data without statics corrections. Flat reflectors are perturbated due to the weathered layer. Figure 4.15b shows the stacked data after applying the calculated statics. Perturbations are removed significantly. This demonstrates that the calculated statics are reasonable enough to address static correction for these data. However, there are still some small perturbations. In order to remove the remaining statics, we apply residual statics (Figure 4.15c). We see a clear image of the flat reflectors. The red dashed line in Figure 4.14 indicates the total statics obtained from the calculated statics and the residual statics added together. Though at the most station locations there is a good match and compatibility between the calculated statics and the total statics, a significant difference is seen from 2000 m to 2500 m distance, where there is an interpreted major channel with a low phase velocity zone. There are two possibilities for this discrepancy. One is the limited bandwidth of the ground roll. The minimum detectable ground roll frequency for this data set is about 4.5 Hz, which confines the depth of investigation to about 45 m. If there had been more low frequency components, we could have investigated deeper layers and consequently used more information in the statics calculation. Another possibility is poor acquisition at the location of the interpreted major channel. This interpreted channel is a very low phase velocity zone, where we should choose a small aperture. When the geophone interval is wide and the aperture is small, we have only few traces in each CMP gather. This causes a low resolution image of dispersion curves because the phase velocity estimation is based on slant stacking methods where fold number is very

important for resolution. For instance, in a CMP gather where the maximum wavelength is 30 m, an optimum aperture length should be close to 30 m (40 m for example). When the geophone interval is 10 m and the aperture is 40 m, the fold is four, which results in a low resolution image of dispersion curves (Figure 4.17). In order to improve the resolution of dispersion curves, we have to increase the aperture beyond its optimum values. This causes the dispersion curves and the estimated phase velocity to be affected by the other velocity structures in the vicinity of the CMP gather. Therefore, at a low velocity zone surrounded by a higher velocity field, we obtain smaller values for statics than if we were able to analyze the low velocity zone without influence from the surrounding higher velocities.

We calculate S-wave refraction statics from the P-wave receiver refraction static as a conventional method for a comparison with S-wave receiver statics obtained from CCSW. We scale the P-wave receiver static by 2.5 based on an assumption that V_P/V_s ratio is 2.5 and apply these statics to the data. Figure 4.18 shows the stacked data after applying the scaled P-wave receiver refraction statics. Comparing Figure 4.18 with Figure 4.15b, we observe that the CCSW statics provide better corrections. Figure 4.19a shows a shot record without receiver static corrections and Figure 4.19b shows the same record after applying CCSW static corrections. We see better coherency of reflectors after applying the S-wave static correction. Figure 4.20 shows NMO velocity analysis for a CMP gather before and after application of the calculated S–wave receiver statics. NMO velocity analysis has improved significantly after applying the S-wave receiver statics.

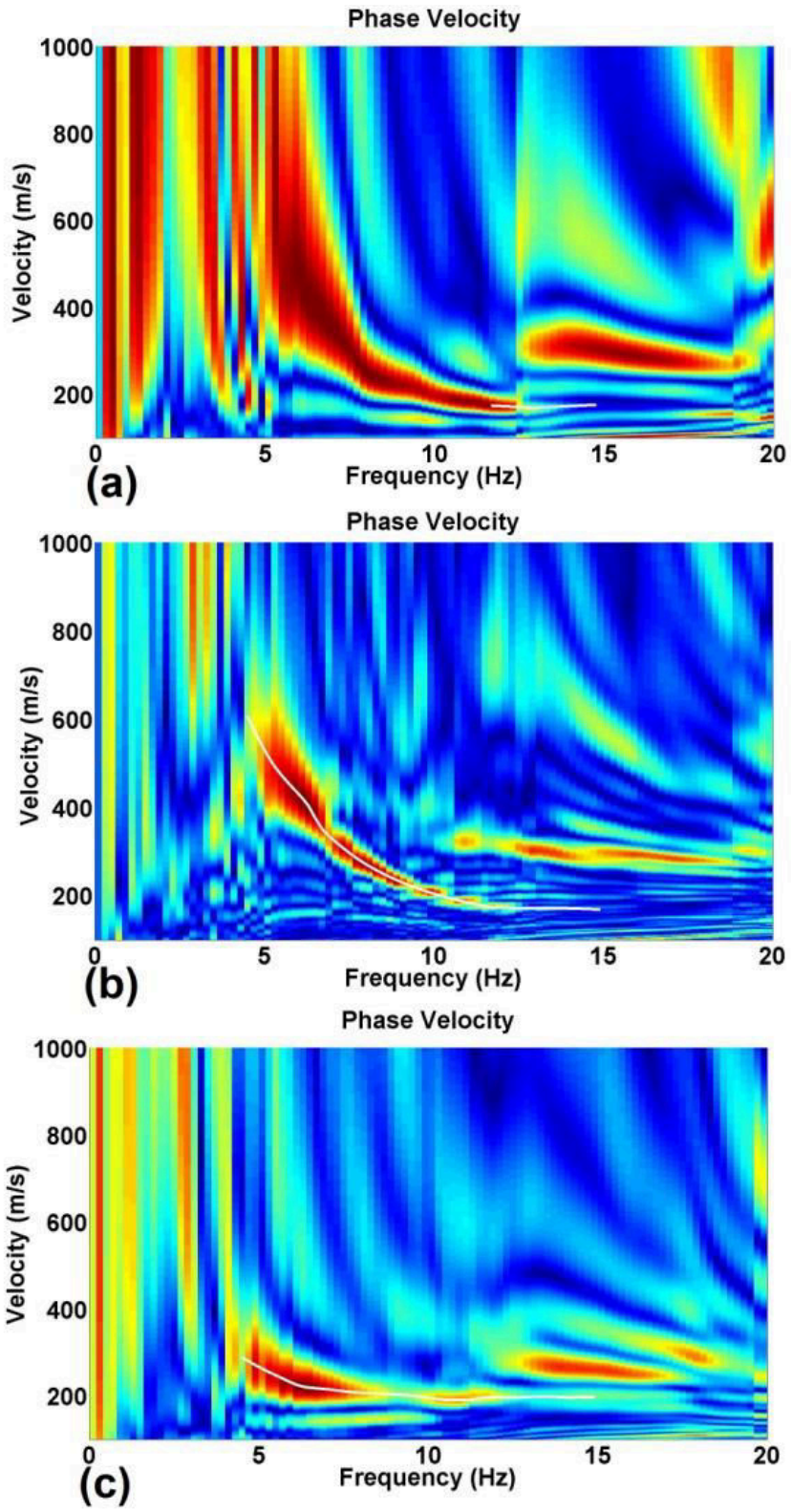

Figure 4.11 (a) Dispersion curve analysis for a CMP gather with the aperture 80 m. (b) Dispersion curve for the same CMP gather with the aperture 200 m, and (c) dispersion curve analysis for a CMP gather whose maximum wavelength is 70 m and the aperture is 80 m.

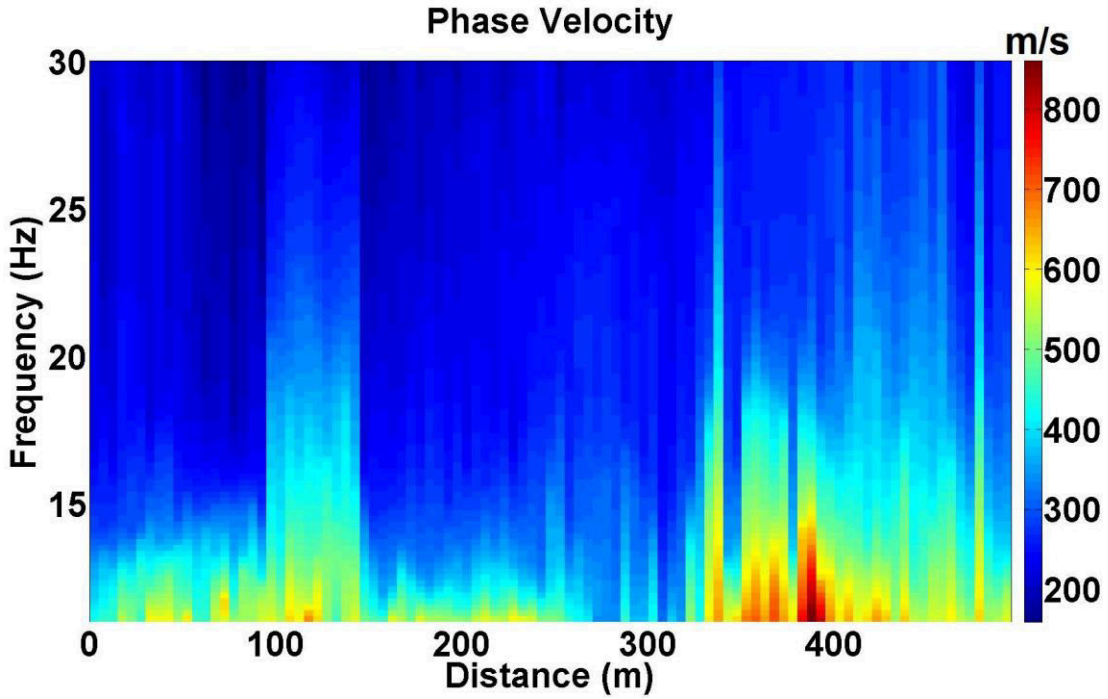

Figure 4.12 The estimated phase velocity for the Hussar data.

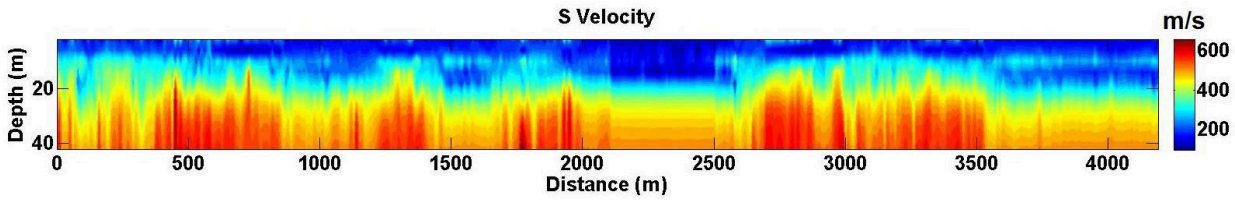

Figure 4.13 The S-wave velocity model for the Hussar data obtained from the phase velocity in Figure 4.12.

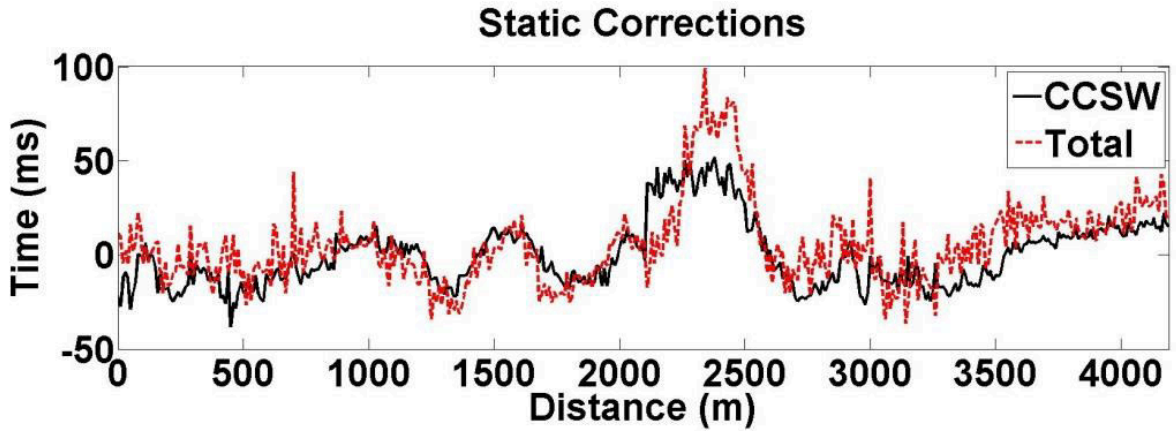

Figure 4.14 Static corrections for the Hussar data.

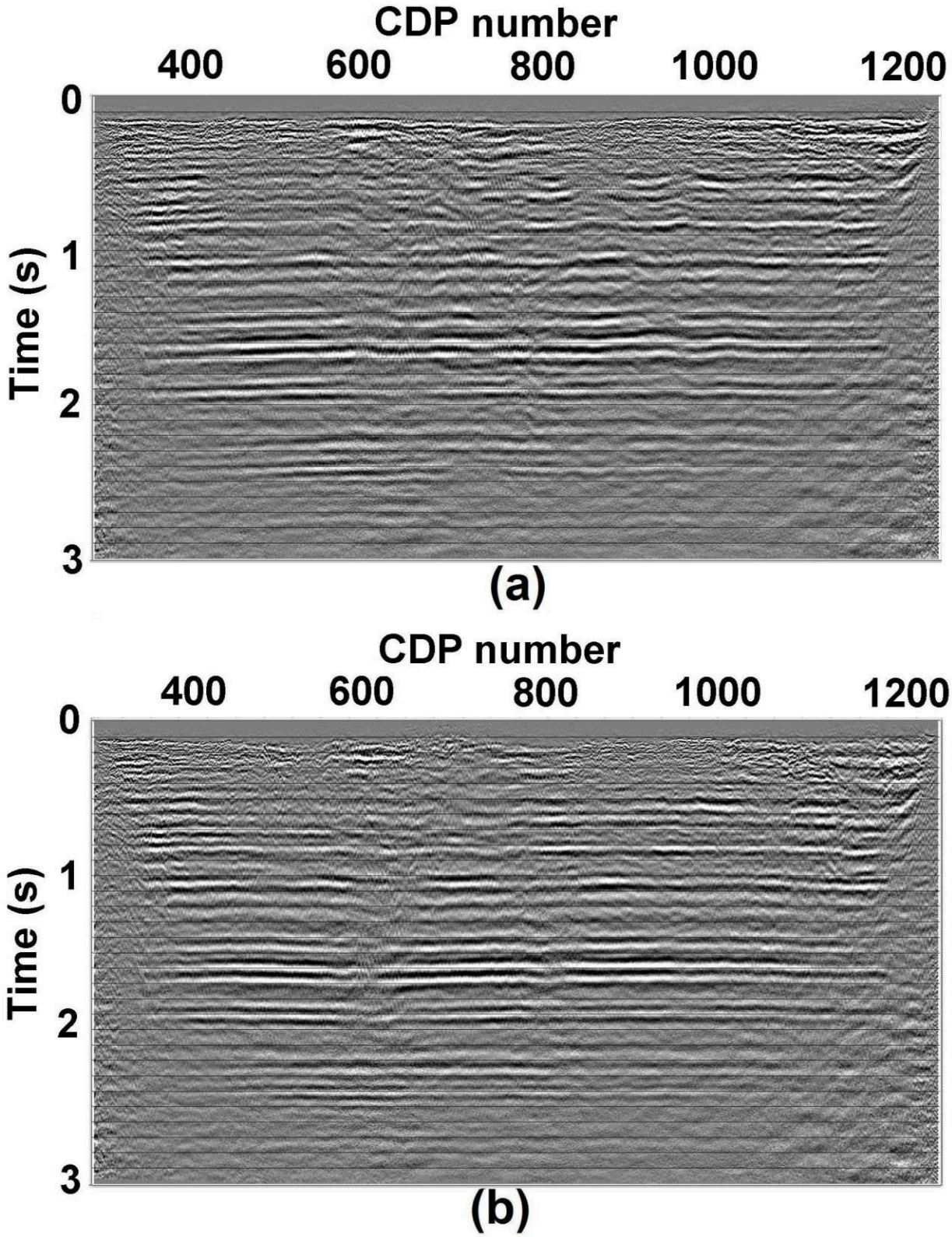

Figure 4.15 (a) Stacked Hussar data before static correction, (b) the stacked data after applying the calculated S-wave receiver static,

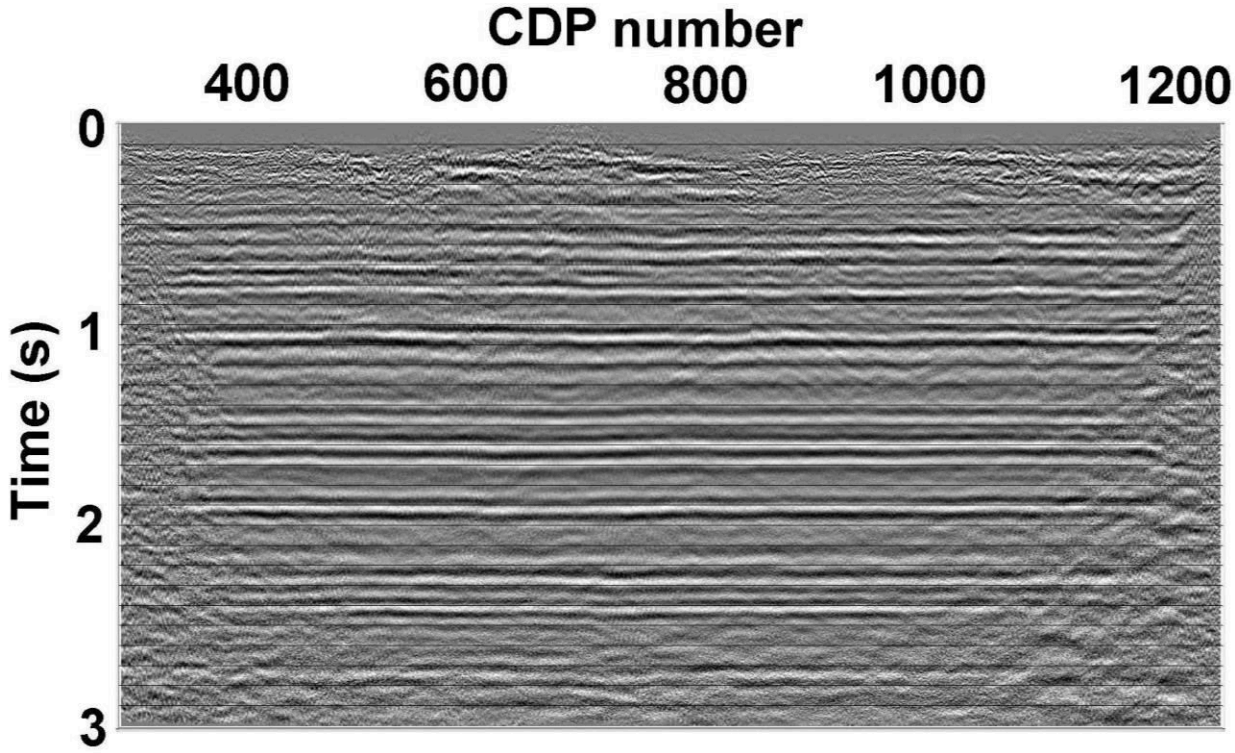

Figure 4.16 The stacked data after applying residual statics.

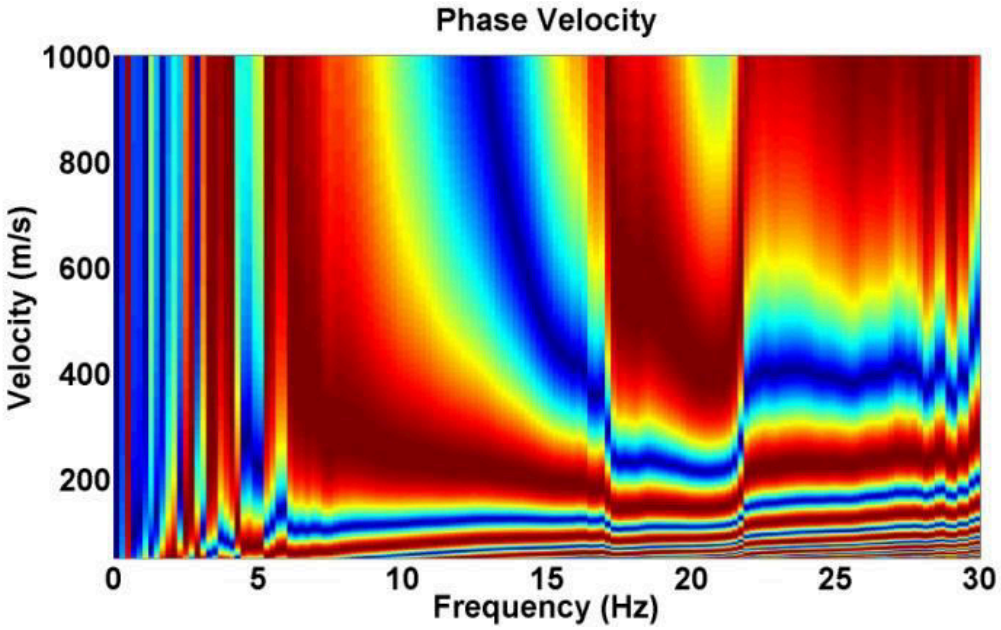

Figure 4.17 The phase velocity estimation for a CMP gather whose fold number is four. We see vague trends of dispersion curve which are due to modal imposition.

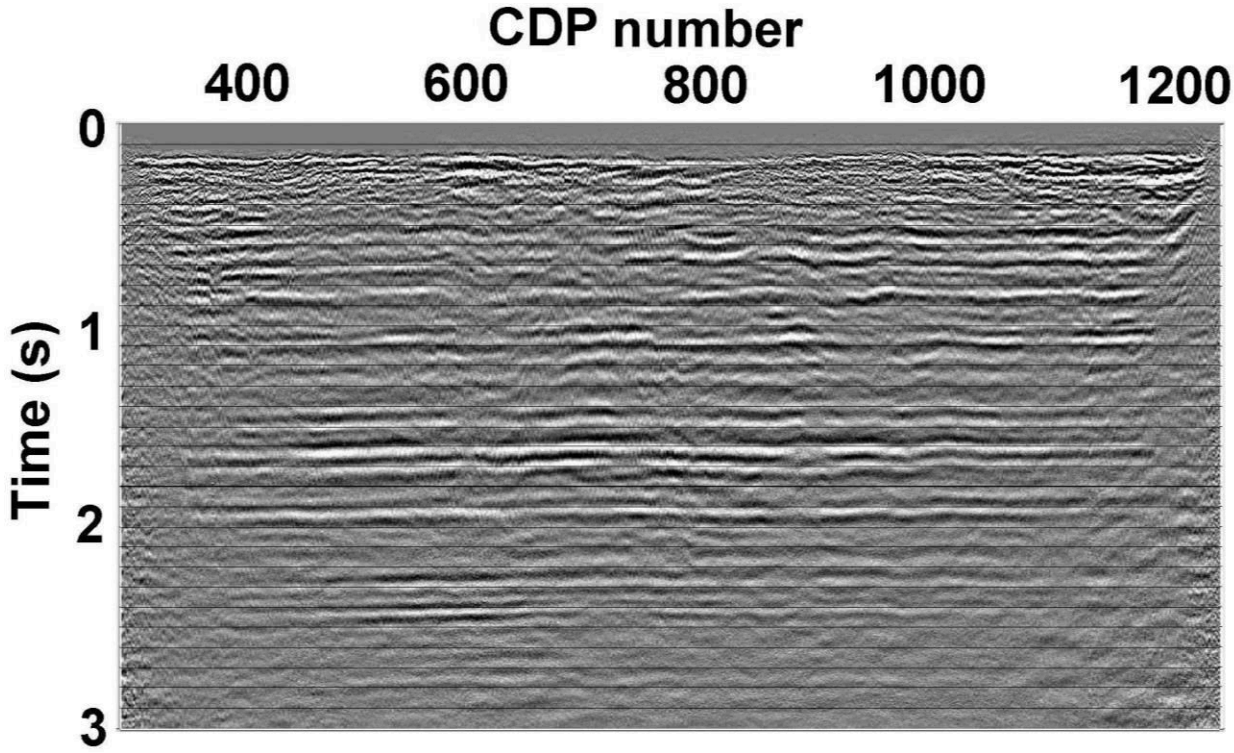

Figure 4.18 P-wave receiver refraction statics scaled by 2.5 applied to the data as S-wave receiver statics.

4.10 Conclusions

We introduce a new approach of the CMP Cross-Correlation of Surface Wave in order to obtain better lateral resolution for near surface S-wave velocity imaging. The idea takes advantages of SASW and MASW methods, and is faster than the conventional CCSW (Hayashi and Suzuki, 2004).

We define an optimum aperture length for maintaining lateral resolution and dispersion curves simultaneously. According to our results, the aperture length must be close to the maximum wavelength. This gives us a better coherency of the fundamental mode and avoids modal interferences.

The detailed static corrections calculated for the dense Priddis data from the S-wave velocity model in this study demonstrate the high potential of the method to be utilized in seismic exploration. The decimated data and the original exhibit the same general trend of receiver static corrections. This shows a potential of the method to address converted wave receiver static corrections when the geophone interval is wide.

In order to have a good estimation of the phase velocity where there are wide ranges of wavelengths, a wavelength dependent aperture must be utilized. The general result of the calculated statics of the Hussar data demonstrates the capacity of CCSW to address converted wave receiver static corrections. We obtain a better image of reflectors after applying additional residual statics.

Our ability to successfully extract information from converted waves and S-waves is dramatically hampered by our lack of understanding of the near-surface S-wave velocity structure. This is exactly why the surface wave methods should be taken into account. However, if we want to obtain more reliable results from surface wave, we will have to optimize acquisition parameters in areas where there are very low velocity zones. We should also consider the limitations of surface-wave methods such as the modal superposition, which can cause error in the estimation of the phase velocity.

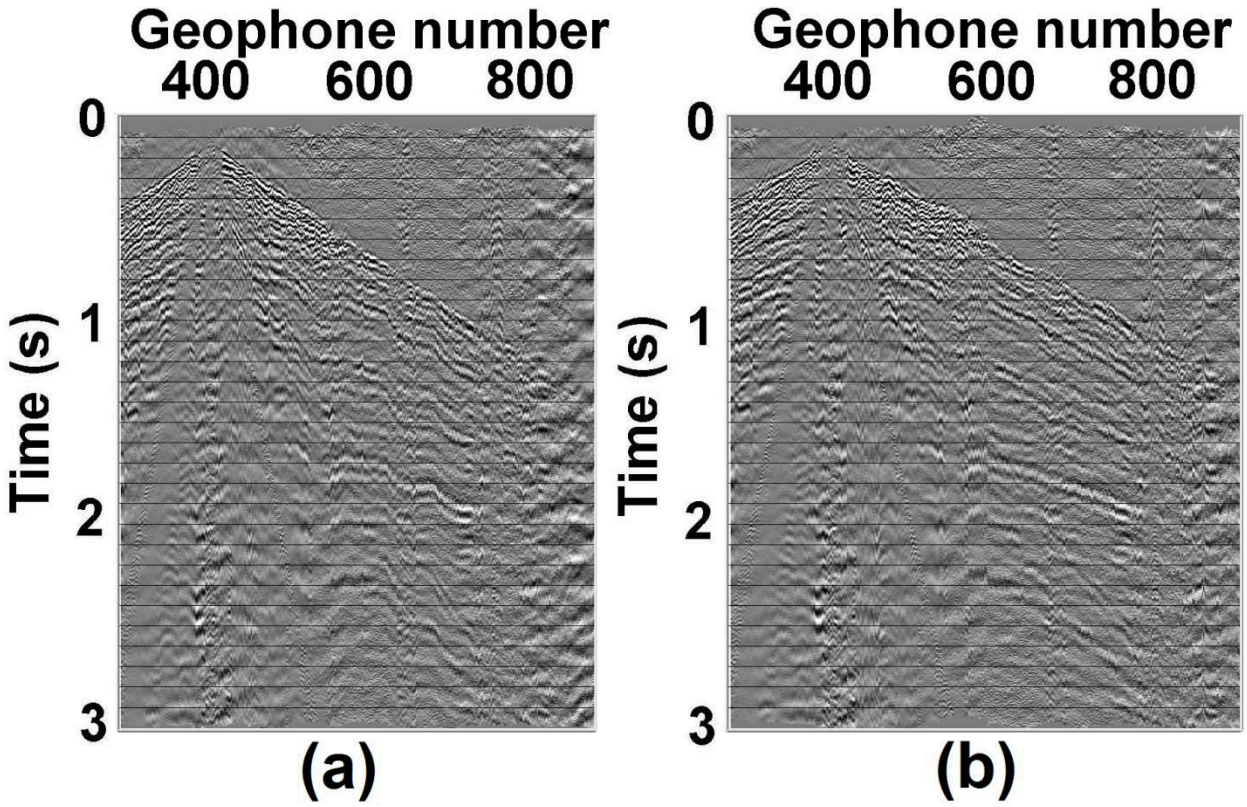

Figure 4.19 A shot record, (a) before without static corrections, and (b) after applying static corrections.

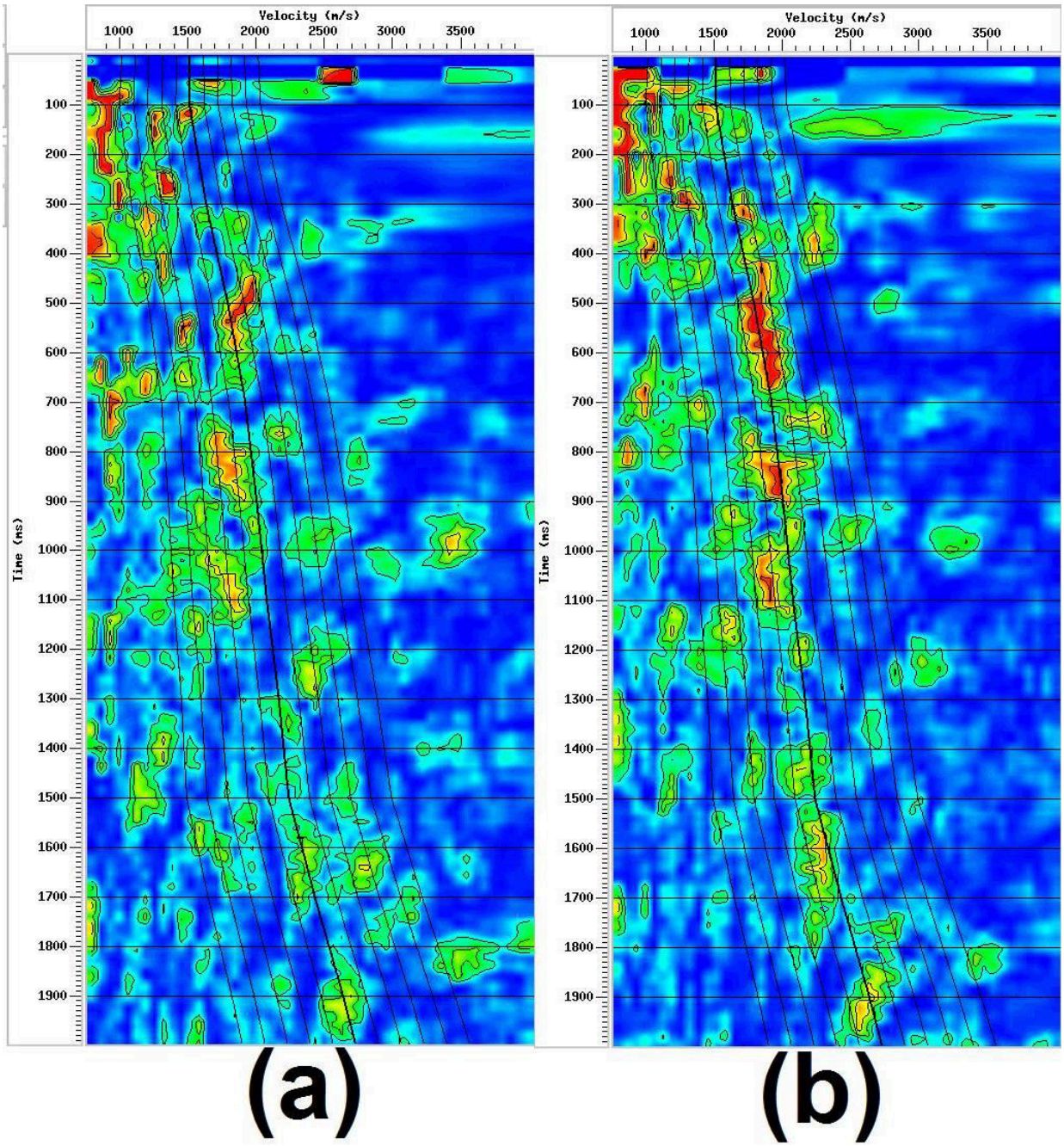

Figure 4.20 NMO velocity analysis. (a) before static correction and (b) after applying the calculated statics.

Chapter Five: Summary and Conclusions

As a part of my PhD thesis, I developed two novel mathematical models to estimate phase and group velocities of surface waves (Chapters 2 and 3). I also enlarged upon the idea of CMP Cross-Correlation of Surface Waves (CCSW) to estimate a shear wave velocity model to compute converted wave static corrections (Chapter 4).

The S transform and its generalized versions provide frequency-dependent resolution that makes it suitable to process non-stationary seismic signal. In Chapter 2, a mathematical model is developed based on the generalized S transform to estimate propagation parameters (wavenumber, phase velocity, group velocity and attenuation function) of surface waves in dispersive and attenuating media. This method involves using a scaling factor in the generalized S transform to control spectral localization. Therefore results can be improved, especially for a highly dispersive and dissipative medium. Based on the mathematical model, wavenumber and phase velocity are obtained directly from the absolute phase value of the ridges of the S-domain, and group velocity is computed from the time difference of the ridges of the transform. Frequency-dependent attenuation is estimated by the relative amplitudes of the ridges of the transform. According to the results obtained from the analyses of the synthetic data, a larger scaling factor should be chosen for highly disperse surface waves. In order to optimize the application of the method for highly dispersed surface waves, a cost function is introduced. The cost function determines a minimum optimum value for the scaling factor. We could make decision what ranges of the scaling factor should be chosen to avoid overlapping time-frequency spectrum of different modes. When signal to noise ratio is small at low frequencies, estimated wavenumber is perturbed. Another cost function is introduced to estimate wavenumber perturbation. The cost function is highly non-linear; therefore it must be minimized with global optimization methods such as Simulated Annealing.

Though the method introduced in Chapter 2 is robust especially where the surface wave is highly dispersed, parameterization within the method becomes ambiguous when the surface wave is multi-modal. In order to generalize the application of the mathematical model for the estimation of the group velocity, the slant stack generalized S transform based method is introduced in Chapter 3. The method takes advantage of slant stacking in the generalized S transform domain. The generalized S transform returns a three dimensional analysis domain (time, frequency and offset) when given a two dimensional gather (a shot gather for example). At

each constant frequency f in the time, frequency and offset domain, there is a 2D common frequency gather in time and offset coordinates, and multi-modal surface waves appear there as linear events. The group velocity of each member of this set of multi-modes (the fundamental mode plus the higher modes) corresponds to the apparent velocity of the linear events. To estimate each linear velocity, slant stacking is implemented to transform the time and offset coordinates to intercept time and slowness coordinates. Since surface wave is initiated from a source point at time $t=0$, the fundamental and higher modes intercept at time $T=0$, so the group velocity of each mode at each frequency is determined by picking the slowness and then calculating the inverse. Using this process, we create a 2D image of the group velocity for all ranges of frequency. Similar to Chapter 2, the scaling factor inserted in the generalized S transform facilitates the application of the method for wide rangers of frequencies. According to the empirical results presented in Chapter 3, in order to increase the frequency resolution, a wide window in the time domain should be utilized. When the window is widened in the time domain, the time resolution will decrease at low frequencies which consequently results in a low velocity resolution of low frequency surface wave. Therefore, there is a tradeoff between the resolution of low and high frequency surface wave. It is concluded where surface wave has a broad range of frequencies, different scaling factors with respect to the frequency content of surface wave should be chosen.

Surface waves provide information on the earth's layers nearest to the earth's surface. We can estimate a near surface shear wave velocity model by the inversion of the phase velocity of ground roll. Based on this procedure, two conventional methods have developed by previous works, "Spectral Analysis of Surface Waves (SASW)" and "Multi-channel Analysis of Surface Waves (MASW)". In SASW, the phase velocity of the fundamental mode of ground roll is estimated by configuring and reconfiguring a pair of receivers and shots respectively with respect to a mid-point. Since a dispersion cure is estimated with respect to a mid point, SASW provides a good lateral resolution. However, the method is very vulnerable to noise because only two records are available for each shot. In MASW, a dispersion cure is calculated by analyzing several traces from a multi-channel data. Therefore, the method is more robust in the presence of variable source wavelet and noise in comparison with SASW. But, MASW provides a weaker lateral resolution because of the long receiver array that must be used and the fact that a dispersion curve is not estimated with respect to a mid-point. CMP Cross-Correlation of Surface

Waves (CCSW) takes the advantage of the two conventional methods. According to the methodology introduced in Chapter 4, each trace of a shot record is cross-correlated with a reference trace that is selected from within the shot gather based on high signal to noise ratio. This step removes the initial phase of a source. New midpoints that relate to the correlated traces are then calculated. The phase velocity is calculated for each CMP gather, and finally the resulting dispersion is converted to a vertical shear wave velocity through an inverse procedure (Conjugate Gradient (Appendix B) for example). This approach is faster than the conventional CCSW introduced by Hayashi and Suzuki, (2004) because in the conventional CCSW all traces within a CMP gather are cross-correlated with each other which is computationally expensive. The concept of *aperture* is introduced in Chapter 4 in order to optimize the output of the method to address the calculation of converted wave static corrections. Aperture is a window length. Only those traces are considered for processing whose offsets are less than the window length (aperture). The optimum window length (aperture) should be close (one to one and half) to the maximum wavelength in a CMP gather. If the aperture is too short a blurred image of dispersion curves is observed and this causes modal interference. When the aperture is optimum, a high resolution image of each mode within the dispersion curve is seen that avoids modal interferences. Therefore, not only does an appropriate aperture length improve dispersion curve estimation, but it also avoids the modal interference that can be so disastrous in surface waves studies. According to the analysis of the field data in Chapter 4, when there wide ranges of wavelengths, wavelength dependent aperture should be implemented for estimating the phase velocity. The general result of the calculated statics of the Hussar data demonstrates the capacity of CCSW to address converted wave receiver static corrections. The static results are improved applying additional residual statics. However, if we want to obtain more reliable results from surface wave, we will have to optimize acquisition parameters in areas where there are very low velocity zones. We should also consider the limitations of surface-wave methods such as the modal superposition, which can cause error in the estimation of the phase velocity.

Appendix A: Phase velocity calculation

In this appendix, I present a methodology developed by Abo-Zena (1979) for the calculation of the phase velocity of Rayleigh wave for a geological model whose layers are assumed to be horizontally flat, isotropic, homogeneous, and perfectly elastic (Figure A.1).

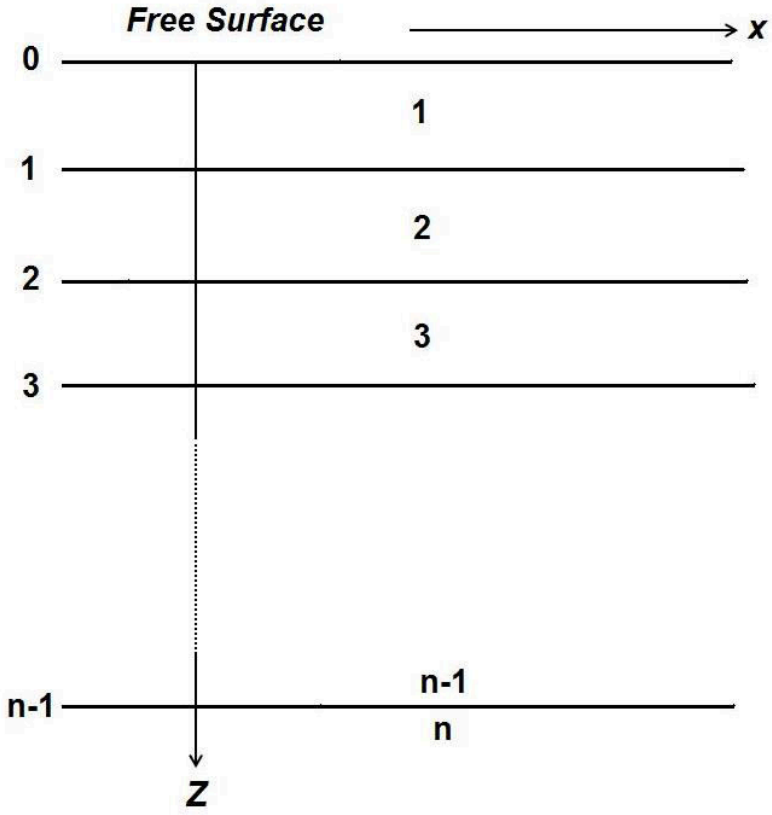

Figure A.1 A geological model composed of *n* layers (modified after Abo-Zena, 1979).

The normal stress σ_z and tangential stress τ_{xz} are linked to the x component 'u' and z component 'w' of displacements by

$$\sigma_z = \lambda\left(\frac{\partial u}{\partial x} + \frac{\partial w}{\partial z}\right) + 2\mu\frac{\partial w}{\partial x}, \qquad \text{(A.1)}$$

and

$$\tau_{xz} = \mu\left(\frac{\partial u}{\partial z} + \frac{\partial w}{\partial x}\right), \tag{A.2}$$

where λ and μ denote Lamé modulii. For a layered earth model, we can estimate the phase velocity of Rayleigh wave by considering the following boundary conditions

$$\sigma_z(z = 0) = 0, \tag{A.3}$$

$$\tau_{xz}(z = 0) = 0, \tag{A.4}$$

$$\sigma_z(z = z_m)_m = \sigma_z(z = z_m)_{m+1}, \tag{A.5}$$

$$\tau_{xz}(z = z_m)_m = \tau_{xz}(z = z_m)_{m+1}, \tag{A.6}$$

$$w(z = z_m)_m = w(z = z_m)_{m+1}, \tag{A.7}$$

and

$$u(z = z_m)_m = u(z = z_m)_{m+1}, \tag{A.8}$$

where z_m is the depth of the boundary between the two layers 'm' and '$m + 1$'. Equations A.3 and A.4 imply that at the surface, the Normal and tangential stresses are zero, Equations A.5, A.6, A.7 and A.8 imply that at the boundary between two layers stresses and displacements are equal to each other. Abo-Zena (1979) presents a mathematical model to calculate the phase velocity using a scalar potential (ϕ) and a vector potential (ψ) (Ewing et al., 1957)

$$\nabla^2\phi = \frac{1}{{V_p}^2}\frac{\partial^2\phi}{\partial t^2}, \tag{A.9}$$

and

$$\nabla^2\psi = \frac{1}{{V_s}^2}\frac{\partial^2\psi}{\partial t^2}, \tag{A.10}$$

where V_p and V_s denote the P-Wave and S-wave velocities of each layer, respectively. The vertical and horizontal displacements, and the normal and tangential stresses can be written in terms of these potentials as

$$w = \frac{\partial \phi}{\partial z} + \frac{\partial \psi}{\partial x}, \tag{A.11}$$

$$u = \frac{\partial \phi}{\partial x} - \frac{\partial \psi}{\partial z}, \tag{A.12}$$

$$\sigma_z = \lambda \nabla^2 \phi + 2\mu \frac{\partial^2 \phi}{\partial z^2} + 2\mu \frac{\partial^2 \psi}{\partial x \partial z}, \tag{A.13}$$

and

$$\tau_{xz} = \mu \left(2 \frac{\partial^2 \phi}{\partial x \partial z} + \frac{\partial^2 \psi}{\partial x^2} - \frac{\partial^2 \psi}{\partial z^2} \right). \tag{A.14}$$

By assuming both ϕ and ψ to be periodic with respect to time, and the waves to be planar, Abo-Zena (1979) presents the following equations for ϕ and ψ

$$\phi = \left[b_1 \cosh\left(r_p kz\right) + b_2 \sinh(r_p kz) \right] \exp[i(\omega t - kx)], \tag{A.15}$$

and

$$\psi = [b_3 \cosh(r_s kz) + b_4 \sinh(r_s kz)] \exp[i(\omega t - kx)]. \tag{A.16}$$

where k is the wavenumber, and ω is the angular frequency which is given by

$$\omega = 2\pi f, \tag{A.17}$$

and with v_p denoting the phase velocity, r_p and r_s are given (Abo-Zena, 1979) by

$$r_p = \begin{cases} i[\left(\frac{v_p}{V_p}\right)^2 - 1]^{\frac{1}{2}} & v_p > V_p \\ [1 - \left(\frac{v_p}{V_p}\right)^2]^{\frac{1}{2}} & v_p < V_p \end{cases}, \tag{A.18}$$

$$r_s = \begin{cases} i[\left(\frac{v_p}{V_s}\right)^2 - 1]^{\frac{1}{2}} & v_p > V_s \\ [1 - \left(\frac{v_p}{V_s}\right)^2]^{\frac{1}{2}} & v_p < V_s \end{cases}. \tag{A.19}$$

If there is no source at infinity (Abo-Zena, 1979), then

$$b_1 = -b_2, \tag{A.20}$$

and

$$b_3 = -b_4. \tag{A.21}$$

Therefore, equations A.15 and A.16 attain the form

$$\phi = b_1\left[\cosh\left(r_p kz\right) - \sinh(r_p kz)\right]\exp[i(\omega t - kx)], \tag{A.22}$$

and

$$\psi = b_3[\cosh(r_s kz) - \sinh(r_s kz)]\exp[i(\omega t - kx)]. \tag{A.23}$$

By inserting equations A.22 and A.23 into equations A.11-14 and considering the boundary conditions (equations A.3-8), Abo-Zena (1979) derives the matrix equation

$$\begin{bmatrix} (J_{11} + J_{12}) & (J_{21} + J_{22}) \\ (J_{13} + J_{14}) & (J_{23} + J_{24}) \end{bmatrix} \begin{bmatrix} iu/k \\ w/k \end{bmatrix} = \begin{bmatrix} 0 \\ 0 \end{bmatrix}, \tag{A.24}$$

where J_{ij} are elements of a 4×2 matrix 'J'. J is given by (Abo-Zena, 1979)

$$J = [U_n(0)]^{-1} A_{n-1} A_{n-2} \cdots A_2 A_1 \begin{bmatrix} 1 & 0 \\ 0 & 1 \\ 0 & 0 \\ 0 & 0 \end{bmatrix}, \tag{A.25}$$

where n is the number of layers,

$$A_m = [U_m(z_m)][U_m(0)]^{-1}, \tag{A.26}$$

$$U_m(z)=\begin{bmatrix} 1 & 1 & r_s & r_s \\ r_p & r_p & 1 & 1 \\ \rho\left(2\left(\frac{V_s}{v_p}\right)^2-1\right) & \rho\left(2\left(\frac{V_s}{v_p}\right)^2-1\right) & 2\rho\left(\frac{V_s}{v_p}\right)^2 r_s & 2\rho\left(\frac{V_s}{v_p}\right)^2 r_s \\ 2\rho\left(\frac{V_s}{v_p}\right)^2 r_p & 2\rho\left(\frac{V_s}{v_p}\right)^2 r_p & \rho\left(2\left(\frac{V_s}{v_p}\right)^2-1\right) & \rho\left(2\left(\frac{V_s}{v_p}\right)^2-1\right) \end{bmatrix}\times$$

$$\begin{bmatrix} exp(-r_p kz) & 0 & 0 & 0 \\ 0 & exp(-r_p kz) & 0 & 0 \\ 0 & 0 & exp(-r_s kz) & 0 \\ 0 & 0 & 0 & exp(-r_s kz) \end{bmatrix}$$

$$+\begin{bmatrix} 1 & -1 & r_s & -r_s \\ -r_p & r_p & -1 & 1 \\ \rho\left(2\left(\frac{V_s}{v_p}\right)^2-1\right) & -\rho\left(2\left(\frac{V_s}{v_p}\right)^2-1\right) & 2\rho\left(\frac{V_s}{v_p}\right)^2 r_s & 2\rho\left(\frac{V_s}{v_p}\right)^2 r_s \\ -2\rho\left(\frac{V_s}{v_p}\right)^2 r_p & 2\rho\left(\frac{V_s}{v_p}\right)^2 r_p & -2\rho\left(\left(\frac{V_s}{v_p}\right)^2-1\right) & \rho\left(2\left(\frac{V_s}{v_p}\right)^2-1\right) \end{bmatrix}\times$$

$$\begin{bmatrix} exp(-r_p kz) & 0 & 0 & 0 \\ 0 & exp(-r_p kz) & 0 & 0 \\ 0 & 0 & exp(-r_s kz) & 0 \\ 0 & 0 & 0 & exp(-r_s kz) \end{bmatrix}, \qquad \text{(A.27)}$$

and

$$[U_m(0)]^{-1}=\begin{bmatrix} 2\left(\frac{V_s}{v_p}\right)^2 & 0 & -1/\rho & 0 \\ 0 & -\left(2\left(\frac{V_s}{v_p}\right)^2-1\right)/r_p & 0 & 1/\rho r_p \\ -\left(2\left(\frac{V_s}{v_p}\right)^2-1\right)/r_s & 0 & 1/\rho r_s & 0 \\ 0 & 2\left(\frac{V_s}{v_p}\right)^2 & 0 & -1/\rho \end{bmatrix}. \qquad \text{(A.28)}$$

It is obvious that the matrix

$$\begin{bmatrix} (J_{11}+J_{12}) & (J_{21}+J_{22}) \\ (J_{13}+J_{14}) & (J_{23}+J_{24}) \end{bmatrix}$$

in equation A.24 must be singular, otherwise the displacements u and w will be zero. Therefore, the determinant of the matrix must be zero

$$F = (J_{11} + J_{12})(J_{23} + J_{24}) - (J_{21} + J_{22})(J_{13} + J_{14}) = 0. \quad \text{(A.29)}$$

Equation A.29 is called the dispersion function. We calculate the phase velocity of dispersed surface waves by finding the roots of the dispersion function. The smallest value of the phase velocity that satisfies equation A.29 is called the fundamental mode, and the first velocity above the fundamental mode is called the first higher mode. It is implied from equations A.29 that the phase velocity is calculated with respect to the S-wave velocity, P-wave velocity, density and thickness of the layers.

Appendix B: Conjugate Gradient

Generally, an inverse problem is given by (Aster et al., 2004)

$$Gm = d, \tag{B.1}$$

where d denotes data, m denotes model parameters, and G is a matrix which presents the explicit relationship between the data and the model parameters. We obtain the model parameters 'm' from the observed data 'd' using

$$m = (G^T G)^{-1} G d. \tag{B.2}$$

When there is a bulk volume of data, it is impractical to solve equation B.1 because the matrix G might have thousands of rows and columns which requires a great deal computer memory. Iterative methods are used to address the problem. Iterative methods are classified into two categories, *deterministic methods* (gradient-based), and *stochastic methods* (evolutionary). The deterministic methods minimize an objective function by the means of the gradient of the function. Although the deterministic methods are fast at finding a minimum that satisfies the objective function, they might fall into a local minimum when the objective function is not linear and has more than one minimum, and thus fail to estimate the global minimum (the best answer for the objective function). In order to avoid being trapped in a local minimum, we should take different parameters into account such as a good initial model to obtain the global minimum. The methodology of Steepest Descent, Newton's method, the Gauss-Newton method, the Levenberg-Maquardt method and Conjugate Gradient method are examples of deterministic methods. Alternatively, stochastic methods are not based on the gradient of an objective function. At the beginning, a random set of solutions is created for an objective function. Different random solutions are computed and compared. From those solutions which give the better results, a new set of solutions is generated in an organized way. Finally, an optimum solution (global minimum) is estimated after some iteration. Genetic algorithm, simulated annealing, particle swarm and ant colony are examples of stochastic methods.

The Conjugate Gradient method is very similar to the Steepest Descent method where each iteration step is calculated with respect to the gradient of the objective function (Colaco et al., 2006). But, in the Conjugate Gradient method, the direction of descent is not the negative gradient direction of the objective function which this results in a faster convergence and consequently a faster process (less iteration). This procedure is based on computing a linear

combination of the negative gradient direction of the objective function at the current iteration with the direction of descent of the previous iteration (Shewchuk, 1994).

Consider an objective function $g(\boldsymbol{V_s})$ where $\boldsymbol{V_s}$ is the S-wave velocity vector for a layered model whose the S-wave velocities are V_{s_1}, V_{s_2}, …, and V_{s_m}. $g(\boldsymbol{V_s})$ is given by

$$g(\boldsymbol{V_s}) = \sum_{k=1}^{n}(\boldsymbol{v_{p}}_{obs} - \boldsymbol{v_p}(\boldsymbol{V_s}))^2, \tag{B.3}$$

where $\boldsymbol{v_{p}}_{obs}$ denotes the observed phase velocity (estimated for a field data), $\boldsymbol{v_p}(\boldsymbol{V_s})$ denotes the calculated phase velocity for the geological model as a function of $\boldsymbol{V_s}$, and n is the number of the phase velocity samples. Equation B.3 can be written in matrix form as

$$g(\boldsymbol{V_s}) = \left(\boldsymbol{v_{p}}_{obs} - \boldsymbol{v_p}(\boldsymbol{V_s})\right)^T \left(\boldsymbol{v_{p}}_{obs} - \boldsymbol{v_p}(\boldsymbol{V_s})\right), \tag{B.4}$$

where

$$\left(\boldsymbol{v_{p}}_{obs} - \boldsymbol{v_p}(\boldsymbol{V_s})\right)^T = \left[v_{p_{obs_1}} - v_p(\boldsymbol{V_s})_1, \cdots, v_{p_{obs_n}} - v_p(\boldsymbol{V_s})_n\right]. \tag{B.5}$$

The Jacobean matrix is given by

$$J(\boldsymbol{V_s}) = \left[\frac{\partial \boldsymbol{v_p}\ (\boldsymbol{V_s})}{\partial \boldsymbol{V_s}}\right]^T = \begin{bmatrix} \frac{\partial v_p(\boldsymbol{V_s})_1}{\partial V_{s_1}} & \frac{\partial v_p(\boldsymbol{V_s})_1}{\partial V_{s_2}} & \cdots & \frac{\partial v_p(\boldsymbol{V_s})_1}{\partial V_{s_m}} \\ \frac{\partial v_p(\boldsymbol{V_s})_2}{\partial V_{s_1}} & \frac{\partial v_p(\boldsymbol{V_s})_2}{\partial V_{s_2}} & \cdots & \frac{\partial v_p(\boldsymbol{V_s})_1}{\partial V_{s_m}} \\ \vdots & \vdots & \vdots & \vdots \\ \frac{\partial v_p(\boldsymbol{V_s})_n}{\partial V_{s_1}} & \frac{\partial v_p(\boldsymbol{V_s})_n}{\partial V_{s_2}} & \cdots & \frac{\partial v_p(\boldsymbol{V_s})_n}{\partial V_{s_m}} \end{bmatrix}. \tag{B.6}$$

To optimize the S-wave velocity, the objective function (equation B.3) is minimized using a Conjugate Gradient as

$$\boldsymbol{V_s}^{k+1} = \boldsymbol{V_s}^{k} + \beta^k \boldsymbol{\chi}^k \tag{B.7}$$

where

$$\beta^k = \frac{\left(\boldsymbol{v_{p}}_{obs} - \boldsymbol{v_p}(\boldsymbol{V_s})\right)^T \left[J^k\right]^T \boldsymbol{\chi}^k}{\left(\left[J^k\right]\boldsymbol{\chi}^k\right)^T \left(\left[J^k\right]\boldsymbol{\chi}^k\right)}, \tag{B.8}$$

$$\boldsymbol{\chi}^k = [J^k]^T \left(\boldsymbol{v_{p}}_{obs} - \boldsymbol{v_p}(\boldsymbol{V_s}^k)\right) + \eta^k \boldsymbol{\chi}^{k-1}, \tag{B.9}$$

and

$$\eta^k = \frac{\left([J^k]^T\left(\boldsymbol{v_{p}}_{obs} - \boldsymbol{v_p}(\boldsymbol{V_s}^k)\right)\right)^T \left([J^k]^T\left(\boldsymbol{v_{p}}_{obs} - \boldsymbol{v_p}(\boldsymbol{V_s}^k)\right) - [J^{k-1}]^T\left(\boldsymbol{v_{p}}_{obs} - \boldsymbol{v_p}(\boldsymbol{V_s}^{k-1})\right)\right)}{\left([J^{k-1}]^T\left(\boldsymbol{v_{p}}_{obs} - \boldsymbol{v_p}(\boldsymbol{V_s}^{k-1})\right)\right)^T \left([J^{k-1}]^T\left(\boldsymbol{v_{p}}_{obs} - \boldsymbol{v_p}(\boldsymbol{V_s}^{k-1})\right)\right)}. \tag{B.10}$$

Since Conjugate Gradient produces m conjugates directions for an m dimensional field, we should find an optimum solution for the objective function after m-iterations (Shewchuk, 1994).

Appendix C: Phase shift method

Considering a seismic record in the time-offset domain $u(x,t)$ containing ground roll, the Fourier transform of each trace is expressed by

$$U(x,\omega) = \int u(x,t)e^{-i\omega t}\,dt. \tag{C.1}$$

The equation above could be rewritten as

$$U(x,\omega) = P(x,\omega)A(x,\omega), \tag{C.2}$$

where $P(x,\omega)$ is the phase spectrum and $A(x,\omega)$ is the amplitude spectrum. The amplitude spectrum contains all the information about attenuation and spherical divergence whereas the phase spectrum contains all the information about dispersion. Applying the operator $e^{i2\pi fx/v_p}$, where v_p is a phase velocity, to integral

$$V(f,v_p) = \int \frac{U(x,\omega)}{|U(x,\omega)|} e^{i2\pi fx/v_p}\,dx = \int P(x,\omega)e^{i2\pi fx/v_p}\,dx, \tag{C.3}$$

produces a two dimensional image of the phase velocities versus frequencies (Park et al., 1998). It is clear that, at those frequencies where v_p is equal to the phase velocities of the signal, the integral will have a maximum.

Figure C.1 shows synthetic data containing a bi-modal surface wave. The geophone spacing is one meter and time sampling is 2 ms. Ricker wavelets are used in both modes. Figure C.2 shows the phase velocity obtained from the phase shift method. The solid and dashed lines correspond to the theoretical phase velocities. As shown in Figure C.2, the theoretical values are well matched by the estimates.

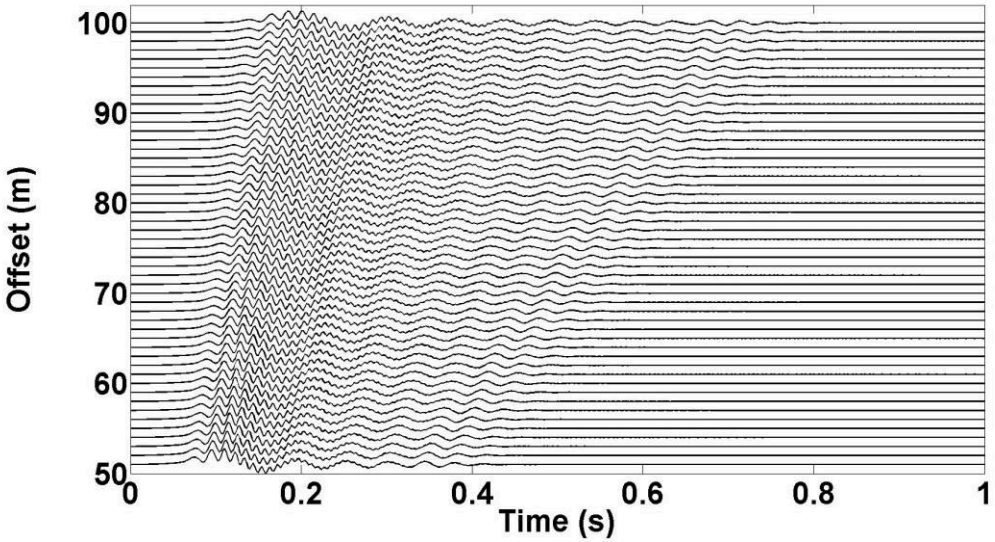

Figure C.1 Synthetic data containing bi- modal ground roll.

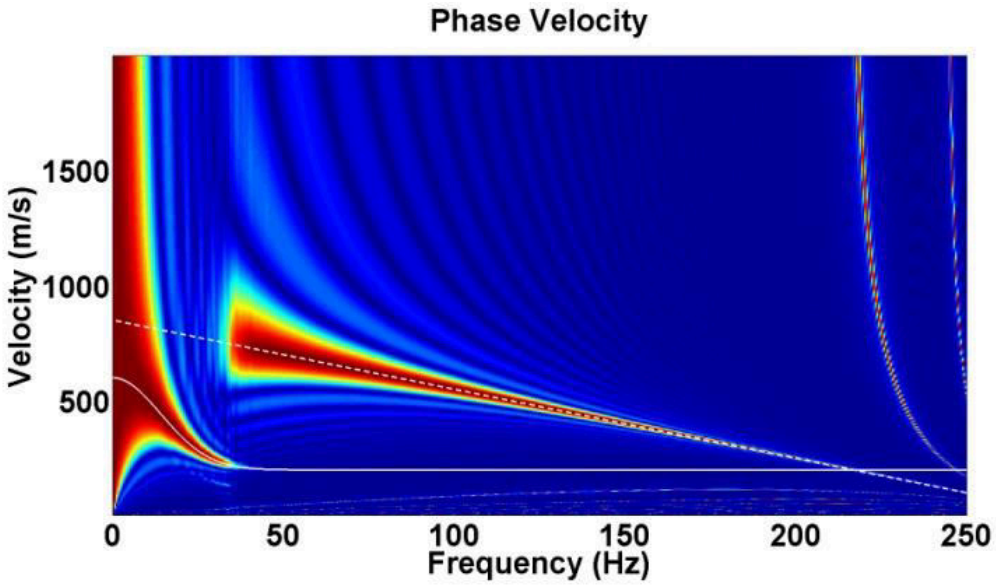

Figure C.2 The phase velocity of the record in Figure 1 obtained from the phase shift method.

References

Abo-Zena, A. M., 1979, Dispersion function computations for unlimited frequency values: Geophys. J. R. astr. Soc., **58**, 91-105.

Askari, R., and Siahkoohi, H. R., 2008, Ground roll attenuation using the S and x–f–k transform: Geophysical Prospecting, **56**, 105–114.

Askari, R., and Ferguson, R. J., 2012, Dispersion and the dissipative characteristics of surface waves in the generalized S transform domain: Geophysics, **77**, 11 - 20.

Askari, R., Ferguson, R. J., Isaac, H., 2013, Optimum aperture length for improving dispersion curve analysis in CMP Cross- Correlation of Surface Waves: GeoConvention 2013, Calgary, AB.

Aster, R. C., Borchers, B., and Thurber, C. H., 2004, Parameter Estimation and Inverse Problems: Elsevier Academic Press.

Beaty, K. D.R. Schmitt, and M. Sacchi, 2002, Simulated annealing inversion of multimode Rayleigh wave dispersion curves for geological structure: Geophys. J. Int., **151**, 622-671

Cary, P. W., and Eaton, D. W. S., 1993, A simple method for resolving large converted-wave (P-SV) static: Geophysics, **58**, 429-433.

Colaço, M. J., Orlande, H. R. B., and Dulikravich, G. S., 2006, Inverse and optimization problems in heat transfer: Journal of the Brazilian Society of Mechanical Sciences and Engineering, **28**, 1–24.

DeAngelo, M. V., Backus, M., Hardage, B. A., and Murray, P., 2003, Depth registration of P-wave and C-wave seismic data for shallow marine sediment characterization, Gulf of Mexico: The Leading Edge, **22**, 96–105.

Dobrin, M. B., 1951, Dispersion in seismic surface waves: Geophysics, **16**, 63-80.

Dulaijan, K. A., 2008, Near-surface characterization using seismic refraction and surface-wave methods: M.Sc. dissertation, University of Calgary.

Eaton, D. W. S., Cary, P. W., and Schafer, A. W., 1991, Estimation of P-SV statics using stack-power optimization: The CREWES Research Report: University of Calgary, **3**.

Evans, B. J., 1998, A handbook for seismic data acquisition in exploration: SEG.

Evison, F. F., Orr, R. H., and, Ingham, C. E., 1959, Thickness of the earth's crust in Antarctica: Nature, **183**, 306-308.

Ewing, M., Jardetzky, W., and Press, F., 1957, Elastic Waves in Layered Media: McGraw-Hill, New York.

Gabor, D., 1946, Theory of communication: J. Inst. Elect. Eng., **93**, 429–457.

Frasier, C., and Winterstein, D., 1990, Analysis of conventional and converted mode reflections at Putah sink, California using three-component data: Geophysics, **55**, 646-659.

Hayashi, K., and H. Suzuki, 2004, CMP cross-correlation analysis of multi-channel surface-wave data: Exploration Geophysics, **35**, 7–13.

Herrmann, R. B., 1973, Some aspects of band-pass filtering of surfacewaves: Bull. seism. Soc. Am, **63**, 663–671.

Holschneider, M., Diallo, M. S., Kulesh, M., Ohrnberger, M., Lück, E., and Scherbaum, F., 2005, Characterization of dispersive surface waves using continuous wavelet transforms: Geophys. J. Int., *163*, 463–478.

Ikeda, T., Tsuji, T., and Matsuoka, T., 2013, Window-controlled CMP cross-correlation analysis for surface waves in laterally heterogeneous media: Geophysics, in revision.

Ivanov, J., Park, C. B., Miller, R., and Xia, J., 2000, Mapping Poisson's ratio of unconsolidated materials from a joint analysis of surface-wave and refraction events: Proceedings of the Symposium on the Application of Geophysics to Engineering and Environmental Problems (SAGEEP 2000), Arlington, VA, February 20–24, 11–20

Keilis-Borok, V. I., 1989, Seismic Surface Waves in Laterally Inhomogeneous Earth: Kluwer Academic Publishers, London.

Kennett, B. L. N., 1983, Seismic Wave Propagation in Stratified Media: Cambridge University Press, Cambridge, UK.

Kulesh, M., Holschneider, M., Diallo, M. S., Xie, Q., and Scherbaum, F., 2005, Modeling of wave dispersion using continuous wavelet transforms: Pure and Applied Geophysics, **162**, 843–855.

Kulesh, M., Holschneider, M., Ohrnberger, M., and Lück. E., 2008, Modeling of wave dispersion using continuous wavelet transforms II: wavelet-based frequency-velocity analysis: Pure and Applied Geophysics, **165**, 255–270.

Lay, T., and Wallace, T. C., 1995, Modern Global Seismology: Academic Press, London, UK.

Li, Y., Ma, Z., Sun, P., and Yang, H, 2012, Converted-wave static correction method for thick weathering area: Chinese Journal of Geophysics, **55**, 76-83.

Luo, Y., Xia, J., Liu, J., Liu, Q., and Xu, S., 2007, Joint inversion of high-frequency surface waves with fundamental and higher modes: Journal of Applied Geophysics, **62**, 375–384.

Luo, Y., Xia, J., Miller, R. D., Xu, Y., Liu, J. and Liu, Q., 2008. Rayleigh-wave dispersive energy imaging by high-resolution linear Radon transform: Pure and Applied Geophysics, **165**, 902–922.

Luo, Y., Xia, J., Xu, Y., and Zeng, C., 2011, Analysis of group-velocity dispersion of high-frequency Rayleigh waves for near-surface applications: Journal of Applied Geophysics, **74**, 157-165.

Mallat, S., 1999, A wavelet tour of signal processing: Academic Press, London, UK.

Margrave, G. F., Mewhort, L., Phillips, T., Hall, M., Bertram, M. B., Lawton, D. C., Innanen, K. A. H., Hall, K. W., and Bertram, K. L., 2011. The Hussar Low-Frequency Experiment: CREWES Research Report, Vol. 23, No. 78.

McMechan, G. A., and Yedlin, M. J., 1981, Analysis of dispersive waves by wave field transformation: Geophysics, **46**, 869–874.

Mcfadden, P. D., Cook, J. G., and Forster, L. M., 2002, Decomposition of gear vibration signals by the generalized S transform: Mechanical Systems and Signal Processing, **13**, 691-707.

Nazarian, S., Stokoe, K. H., and Hudson, W. R., 1983, Use of spectral analysis of surface waves method for determination of moduli and thickness of pavement system: Transportation Research Record, **930**, 38–45.

O'Neill, A., and Matsuoka, T., 2005, Dominant higher surface-wave modes and possible inversion pitfalls: J. Eng. Environ. Geophysics. EEGS., **10**, 185–201

Palmer, D., 1980, The generalized reciprocal method of seismic refraction interpretation: Society of Exploration Geophysicists, Tulsa, OK, 104 p.

Park, C. B., Miller, R. D. and Xia, J., 1998, Imaging dispersion curves of surface waves on multi-channel record: 68th Annual International Meeting, SEG, Expanded Abstracts, 1377–1380.

Park, C. B., Miller, R. D., and Xia, J., 1999a, Multichannel analysis of surface waves: Geophysics, **64**, 800–808.

Park, C. B., Miller, R. D., and Xia, J., 1999b, Multimodal analysis of high frequency surface waves: Proceedings of the Symposium on the Application of Geophysics to Engineering and Environmental Problems (SAGEEP), 115–121.

Pinnegar, C. R., and Mansinha, L. 2003a, The Bi-Gaussian *S transform*: SIAM J. SCI. COMPUT., **24**, 1678–1692.

Pinnegar, C. R., and Mansinha, L., 2003b, The *S transform* with windows of arbitrary and varying shape: Geophysics, **68**, 381–385.

Pinnegar, C. R., and Mansinha, L., 2004, Time-local Fourier analysis with a scalable, phase-modulated analyzing function: the *S transform* with a complex window: Signal Processing, **84**, 1167 – 1176.

Rayleigh, L., 1887, On waves propagated along the plane surface of an elastic solid: Proc. R. Soc. London, 17, 4-11.

Sato, Y., 1955, Analysis of dispersed surface waves by means of Fourier Transform 1: Bull. Earthquake Res. Inst., Tokyo Univ., Part 1, **33**, 33-47.

Schwab, F. A., and Knopoff, L., 1972, Fast surface wave and free mode computations, in B. A. Bolt, ed., Methods in computational physics: Academic Press, 87–180.

Sezawa, K., 1927, Dispersion of elastic waves propagated on the surface of stratified bodies and on curved surfaces: Bull. of the Earthquake-Inst: Imperial Univ. Tokyo, 3, 1-18.

Sheriff, R. E., and Geldart, L. P., 1986: Exploration Seismology, Vol. 12. Cambridge University

Sheriff, R. E., 1991, Encyclopedic Dictionary of Exploration Geophysics (3rd ed.): Society of Exploration. ISBN 978-1-56080-018-7.

Shewchuk, J., R., 1994, An introduction to the conjugate gradient method without the agonizing pain: Technical Report CMU-CS-TR-94-125, Carnegie Mellon University. (See also http://www.cs.cmu.edu/~quake-papers/painless-conjugate-gradient.ps)

Stewart, R. R., Gaiser, J. E., Brown, R. J., and Lawton, D. C., 1999, Converted-wave seismic exploration: a tutorial: CREWES Research, **11**, 21-62.

Stockwell, R. G., Mansinha, L., and Lowe, R. P., 1996, Localization of the complex spectrum: The *S* transform: IEEE Transactions on Signal Processing, **44**, 998-1001.

Stokoe II, K.H., Nazarian, S., Rix, G.J., Sanchez-Salinero, I., Sheu, J., and Mok, Y., 1988. In situ seismic testing of hard-to-sample soils by surface wave method: Earthquake Engineering and Soil Dynamic. II — Recent adv. in ground-motion eval. ASCE, Park City, pp. 264–277.

Strobbia, C., Laake, A., Vermeer, P., and Glushchenko A., 2011, Surface waves: use them then lose them. Surface-wave analysis, inversion and attenuation in land reflection seismic surveying: Near Surface Geophysics, **9**, 503-514.

Tatham, R. H., and McCormack, M. D., 1991, Multicomponent seismology in petroleum exploration: Soc. Expl. Geophys.

Xia, J., Miller, R. D., and Park, C. B., 1999, Estimation of near-surface shear-wave velocity by inversion of Rayleigh waves: Geophysics, **64**, 691–700.

Xia, J., Miller, R. D., Park, C. B., Hunter, J. A., Harris, J. B., and Ivanov J, 2002a, Comparing shear wave velocity profiles inverted from multichannel surface wave with borehole measurements: Soil Dynamics and Earthquake Engineering, **22**, 181-190.

Xia, J., Miller, R. D., Park, C. B., Wightman, E., and Nigbor, R., 2002b, A pitfall in shallow shear-wave refraction surveying: Journal of Applied Geophysics, **51**, 1 – 9.

Xia, J., Miller, R. D., Park, C.B., and Tian, G., 2002c, Determining Q of near-surface materials from Rayleigh waves: Journal of Applied Geophysics, **51**, 121-129.

Xia, J., Xu, Y., and Miller, R. D., 2007, Generating image of dispersive energy by frequency decomposition and slant stacking: Pure and Applied Geophysics, **164**, 941-956.

Yi-Ke, L., Xu, C., and Hu, W., 2001, Estimation of near-surface velocity for 3-d complicated topography and seismic tomographic static corrections: Chinese Journal of Geophysics, **44**, 268, 274.

Yilmaz, O., 1987, Seismic Data Processing: Soc. Exploration Geophysicists, Tulsa, OK.

Yilmaz, O., 2001, Seismic data analysis, 2nd. ed.: Soc. Expl. Geophys.

Yousefzadeh, A., 2012, High Resolution Seismic Imaging using Least Squares Migration: Ph.D. dissertation, University of Calgary.